Investigating the dynamics of Rossby wave packets using Local Finite Amplitude Wave Activity

Paolo Ghinassi

Institute for Atmospheric Physics

Johannes Gutenberg University of Mainz

Dissertation submitted for the award of the title "Doctor of Natural Sciences" to the Faculty of Physics, Mathematics, and Computer Science of Johannes Gutenberg University of Mainz

06 December 2019

Declaration

I confirm that this is my own work and the use of all material from other sources has been properly and fully acknowledged.

Paolo Ghinassi

Abstract

Upper tropospheric Rossby wave packets (RWPs) are important dynamical features, because they may act as precursors to high impact weather and have implications for predictability. In the literature, several methods have been proposed to identify RWPs and describe their dynamics. However, most of these methods are based on linear theory and therefore valid only for small amplitude waves, or theoretically and computationally rather complex when valid for finite amplitude waves. The present work introduces a novel diagnostic to quantify the amplitude of RWPs which holds at finite amplitudes and is particularly amenable to compute from atmospheric data. It is based on the local finite amplitude wave activity (LWA) of N. Nakamura and collaborators, which is extended to the primitive equations in isentropic coordinates. LWA is then combined with a zonal filter to remove its intrinsic phase dependence and identify the entire wave packet. The utility of the proposed diagnostics in identifying RWPs is applied first to idealised simulations and then to a specific episode containing large amplitude RWPs. A climatology of Rossby wave activity based on filtered LWA computed from reanalysis data is also presented. Furthermore, the LWA diagnostic is used as a metric to quantify the Rossby wave amplitude error up to the planetary scale in an upscale error growth experiment. The LWA diagnostic identifies a fourth stage of upscale error growth, which could not been revealed using simply potential vorticity or other phase dependent metrics, since they reach saturation at the synoptic scale. The LWA diagnostic is then used to analyse the dynamics of Rossby wave packets, with the goal of distinguishing between conservative propagation against the impact of non-conservative processes. Previous research focused on the dynamics of the single phases of RWPs or described

the dynamics of Rossby waves in the zonal average. Our LWA diagnostic achieves both, providing a quantitative framework for the evolution of the RWPs amplitude rather than its individual phases, but at the same time being local in longitude. In this context a budget equation for filtered LWA is derived and its utility is tested in a hierarchy of models and forecast data. The results confirm the ability of the LWA diagnostic to capture the key features of the RWPs dynamics and identifying non-conservative local sources or sinks of wave activity. In agreement with previous studies, diabatic processes are found responsible to considerably affect the RWP evolution, therefore an improvement of the representation of such physical processes operational models may help to reduce the forecast error.

Contents

List of Publications

The parts of this thesis identified by quotation marks have been published in peer-reviewed journals in the following accepted or submitted articles:

- Ghinassi et al. (2018)

  Ghinassi, P., G. Fragkoulidis, and V. Wirth, 2018: Local Finite Amplitude Wave Activity as a diagnostic for Rossby wave packets, *Mon. Wea. Rev.*, doi:10.1175/MWR-D-18-0068.1.

  Summary: This first paper introduces the novel formulation of Local Wave Activity (LWA) in the primitive equation in isentropic coordinates framework and proposes a zonal filter based on wavelet to remove its phase dependence and to quantify the wave packets amplitude. The new diagnostic is applied to reanalysis data and to a barotropic model simulation to episodes containing large amplitude RWPs and it is compared with a more traditional diagnostic based on the envelope of the meridional wind. Finally, the difference in performance between the two diagnostics is discussed. My supervisor Volkmar Wirth formulated the LWA theory in the primitive equations framework. I have produced all the plots, developed the numerical algorithm to compute LWA and performed the numerical simulations. The algorithm to extract a local zonal wavenumber was developed by Georgios Fragkoulidis. The text has been written by myself and has been revised by Volkmar Wirth.

[1]For further information regarding the AMS Copyright Policy statement, visit the AMS website http://www.ametsoc.org/ CopyrightInformation.

- Baumgart et al. (2019)

  Baumgart, M., Ghinassi, P., Selz, T. Craig, G., Wirth, V. and Riemer, M., 2019: Quantitative view on the processes governing the error growth from the convective to the planetary scale in simulations with a stochastic convection scheme, *Mon. Wea. Rev.*, doi:10.1175/MWR-D-18-0292.1.

  Summary: In this manuscript two diagnostics based on potential vorticity and the envelope of Rossby waves are used to investigate upscale error in a set of global, real-case ensemble simulations. The only difference between the ensemble members lies in the random seed of the stochastic convection scheme. My contribution to this work has been to apply the LWA diagnostics first to a selected month then to all ensemble combinations to investigate the spatial evolution of the envelope error at the planetary scale. Lastly, the time behaviour of the envelope error has been analysed producing time series of the spatially averaged mean squared envelope error. Time series showed evidence of error growth from the synoptic up to the planetary scale, which could not be identified simply via the potential vorticity based diagnostic, since the latter saturates at the synoptic scale. This manuscript has been produced mainly by Marlene Baumgart under the supervision of Michael Riemer. I have produced figures 3, 6b and 9 and I have written parts of the text in sections 2, 3 and 4 of the manuscript. ICON simulations were performed by Tobias Selz. The final text has been revised by Michael Riemer and Volkmar Wirth, with comments from the other co-authors.

- Ghinassi et al. (2019)

  Ghinassi, P., Baumgart, M., Teubler, F., Riemer, M. and Wirth, V., 2019: A budget equation for the amplitude of Rossby wave packets based on finite amplitude local wave activity, *J. Atmos. Sci.*, (in review).

  Summary: This work extends the LWA diagnostics proposed in Ghinassi et al. [2018] deriving a budget equation for the evolution of the amplitude of Rossby wave packets based on filtered LWA. This budget equation allows one to dis-

tinguish between conservative wave packets dynamics and non-conservative local sources or sinks of Rossby wave activity. The utility of the budget equation is demonstrated first in idealized simulations (barotropic and a dry primitive equation model) and in a state-of-the-art operational model. My supervisor Volkmar Wirth formulated the budget equations for LWA. I have produced all the plots, implemented the algorithm for the computation of LWA and its budget and performed the numerical simulations. The wind partitioning based on piecewise potential vorticity inversion used in this work has been computed by Marlene Baumgart and Franziska Teubler. The text has been written by myself and has been revised by Volkmar Wirth, with comments from the other co-authors.

Chapter 1

Introduction

1.1 Motivations and context of this study

The atmospheric flow in the midlatitude upper troposphere is characterised by a strong westerly wind, called jet stream. The jet stream usually is not oriented purely in the zonal direction, but exhibits large scale meanders. This class of slowly evolving, synoptic-to-planetary scale waves are called Rossby waves, in honour of Carl-Gustaf Rossby, who first identified them analysing the atmospheric circulation (Rossby, 1939, 1940). Rossby waves are important for understanding the atmospheric general circulation because they are able to transport energy and momentum across large distances (Charney and Drazin, 1961; Hoskins and Karoly, 1981). "Often, synoptic scale (i.e., zonal wavenumbers 6 – 8). Rossby waves are not strictly circumglobal; rather, their amplitude is spatially inhomogeneous with a relative maximum at a specific location decaying to smaller values at larger distances. This gives rise to so-called Rossby wave packets, which are abbreviated as RWPs in the following" (Ghinassi et al., 2018).

RWPs usually do propagate in the zonal direction along the sharp gradients of potential vorticity (short: PV, Hoskins et al. 1985; Hoskins 1991; Martius et al. 2010) found at the tropopause along the jet stream. The different phases of the wave are called troughs and ridges and manifest as positive and negative PV anomalies, respectively. An important characteristic of RWPs (which is related to the dispersive nature of Rossby waves) is that the wave group propagates eastward faster than the individual phases. Synoptic scale Rossby waves are usually associated with different types of local

weather at the surface, such as cyclones and anticyclones (Holton, 2004; Hoskins and James, 2014). In particular RWPs have been associated with severe weather episodes like strong surface cyclones (Chang, 2005b; Wirth and Eichhorn, 2014), heavy rainfall (Grazzini and van der Grijn, 2002; Martius et al., 2008), blocking (Shutts, 1983) or heat waves and drought (Schubert et al., 2011; Fragkoulidis et al., 2018). "Furthermore, it was argued that RWPs play a role for predictability (Lee and Held, 1993a), although the precise mechanisms may vary from case to case and are currently under debate. In one study, long-lasting RWPs in the Northern Hemisphere were associated with above average forecast skill over Europe (Grazzini and Vitart, 2015), while in another study a RWP actually transmitted errors committed over North America downstream in the zonal direction, leading to a complete forecast failure over Europe a few days later (Rodwell et al., 2013). Recently it has been also shown that diabatic heating or numerical diffusion are able to significantly modify the structure of Rossby waves (Gray et al., 2014; Saffin et al., 2016; Harvey et al., 2018) and the misrepresentation of such processes in operational models may act as a source of forecast errors (Martinez-Alvarado et al., 2016; Baumgart et al., 2019)." (Ghinassi et al., 2019)

The importance of RWPs has motivated the development of various techniques for their identification and analysis. These techniques can be divided into purely diagnostics methods which are able to identify wave packets, or diagnostics which are able to additionally provide information about their dynamics. Example of the former types are the famous Hovmöller diagram (Hovmöller, 1949), or the reconstruction of the envelope of the meridional wind field (Zimin et al., 2003, 2006), while examples of the latter class of diagnostics are the eddy kinetic energy (short EKE, Orlanski and Katzfey 1991; Chang and Orlanski 1993), or specific forms of wave activity (Andrews and Mcintyre, 1976; Andrews and McIntyre, 1978; Edmon et al., 1980) and wave activity flux (Plumb, 1985; Takaya and Nakamura, 2001; Wolf and Wirth, 2017).

As discussed in Ghinassi et al. (2018), wave activity is a particularly suitable quantity to identify Rossby waves, since it quantifies the waviness of the atmospheric flow as the difference between a given PV field and a suitable background. In addition, wave activity is globally conserved quantity in case of a conservative flow. This means that it is possible to neatly distinguish between the effect of conservative dynamics

versus non-conservative processes in the evolution of wave activity. This is in contrast with EKE, which is not globally conserved even in case of a purely conservative flow. Andrews and Mcintyre (1976) derived a widely used expression for wave activity; however they assumed that the atmosphere is quasi-geostrophic and that the waves must be small-amplitude, such as to allow linearisation of the governing equations. If on one hand it is true that the dynamics of Rossby waves in the extratropics can be explained to the leading order in the quasi-geostrophic limit, on the other hand the small amplitude assumption is often too restrictive. It turns out that the amplitude of observed Rossby waves in fact is often large or even finite and Rossby wave exhibits a strongly nonlinear behaviour, which can evolve into wave breaking or cutoff formation. Furthermore, the formulation of wave activity of Andrews and Mcintyre (1976) was defined in terms of zonally averaged quantities and it is thus not suited to diagnose the dynamics of transient, zonally propagating RWPs. Plumb (1985, 1986) and Takaya and Nakamura (2001) successfully derived local (i.e. zonal averaging is not preformed) expressions for wave activity and its flux which can be applied to stationary and transient Rossby waves. However in their formulations they both retained the small amplitude and quasi-geostrophic assumptions. The above diagnostics can formally be applied to atmospheric data, but the validity of the results should be considered with care and related to the assumptions made. Other authors successfully developed theories of local wave activity which are valid at finite amplitudes (Killworth and McIntyre, 1985; McIntyre and Shepherd, 1987), but their formulation is rather complex, preventing a straightforward computation from data. Instead, it would be desirable to use a diagnostic which is able to deal with RWPs of any amplitude and at the same time not too involved to compute.

"A quantity particularly suitable for our purpose is the finite amplitude wave activity (FAWA), of Nakamura and collaborators. Nakamura and collaborators developed FAWA in the barotropic (Nakamura and Zhu, 2010; Solomon and Nakamura, 2012), quasi-geostrophic (Nakamura and Solomon, 2010) and in the primitive equations in isentropic coordinates (Nakamura and Solomon, 2011) frameworks. Recently, Huang and Nakamura (2016) formulated a local (in longitude) version of FAWA, which, since does not require any zonal averaging, would be well suited to identify zonally prop-

agating RWPs. This development was done in the quasi-geostrophic framework, and the authors called their diagnostic "Local Wave Activity" (short LWA). By definition, LWA is a function of both longitude and latitude, and one recovers FAWA upon zonal averaging. This new diagnostic is able to provide information about the "local waviness" of the flow while at the same time being valid for finite amplitude eddies. The authors applied LWA to study spatially localized features such as blocking (Huang and Nakamura, 2016; Nakamura and Huang, 2017), storm tracks (Huang and Nakamura, 2017) or stratospheric vortex weakening events (Lubis et al., 2018). Although this provided interesting results, the limitations given by the quasi-geostrophic approximation result in some undesirable effects like the occurrence of spurious wave activity regions in the equatorial and subtropical upper troposphere as pointed out by the authors (Nakamura and Solomon, 2010, 2011). This state of affairs motivated us to combine the developments of Huang and Nakamura (2016) with those of Nakamura and Solomon (2011) in order to develop a formulation of LWA, including a budget equation for its evolution, which is valid in the primitive equations framework. As we will see in section 4, the construction of LWA using Ertel PV in isentropic coordinates (Ertel, 1942; Hoskins et al., 1985) allows one to obtain a correct description of RWPs in the subtropics and in the midlatitude upper troposphere, both of which are regions of frequent RWP occurrence" (Ghinassi et al., 2019). In the next section we will discuss the new contributions of this thesis, as well as the questions we want to address through the application of the developed diagnostic framework to investigate the dynamics of RWPs.

1.2 Objectives and Contributions

The usual approach to investigate the dynamics of RWPs is to define their amplitude in terms of a quantity that obeys a conservation relation: this allows one to associate the growth and decay of RWPs amplitude to various physical mechanisms. As we have seen in the previous section, LWA is particularly suitable since it is globally conserved and any changes in LWA can be directly related to conservative and nonconservative processes.

"Recently, several PV-based diagnostics have been developed which allow one to quantitatively link the evolution of individual PV anomalies to physical processes, such as the PV tracers technique of Chagnon et al. (2013) and Saffin et al. (2016) or the PV budget equation of Teubler and Riemer (2016). By contrast, our present diagnostics aims to describe the evolution of the amplitude of the whole wave packet rather than individual PV troughs and ridges, thereby providing information related to a larger spatial scale" (Ghinassi et al., 2019).

In this work we will, first, formulate a primitive equation variant of LWA in isentropic coordinates. We will then present a method to remove the phase information from LWA and therefore quantify the amplitude of whole wave packets based on a spatial filter. We will then apply this diagnostic to identify RWPs in idealised simulations and reanalysis data and compare the results with the more traditional and widely used diagnostic based on the envelope of the meridional wind (Zimin et al., 2003). "Once investigated the performance of the filtered LWA diagnostic we will then derive a budget equation for the filtered LWA and demonstrate its utility for quantifying processes associated with the growth and decay of RWPs amplitude. Also in this case we consider a hierarchy of models of increasing complexity, allowing us to build confidence first and subsequently show the value of our approach for real cases. We start by considering simulated RWPs in two idealized models: a barotropic model on the sphere and a dry primitive equation model. These simulations will show the ability of our diagnostic to distinguish between conservative RWP dynamics and non-conservative sources and sinks of LWA. In addition, for the three dimensional flows we will partition the horizontal wind into several contributions following Teubler and Riemer (2016) and Baumgart et al. (2018). This will allow us to associate the impact on the wave amplitude evolution due to the contributions from the near-tropopause, tropospheric-deep and divergent wind. We will then apply the LWA budget to data from a weather forecast model for a case in which the misrepresentation of diabatic processes was suggested to be responsible for an error in an ensuing RWP (Rodwell et al., 2013). The comparison between the forecast and the respective analysis confirms the hypotheses of Rodwell et al. (2013), thus indicating the value of our LWA diagnostic" Ghinassi et al. (2019). Finally, the implications for future research will be

discussed.

1.3 Overview of the Thesis

This thesis is organised as follows: chapter 2 contains some theoretical background needed to interpret our results. This includes a review of the concepts of PV, Rossby waves and RWPs and linear and finite amplitude wave activity. The formulation of LWA in the primitive equations in isentropic coordinates, which is a new theoretical contribution of this thesis is provided in section 2.5.3. In chapter 3 we present the algorithm for the computation of isentropic LWA from meteorological data as well as the description of the zonal filters and the PV inversion technique used to partition the wind into several contributions. In chapter 4 we discuss the utility of the LWA diagnostics to identify wave packets in idealised simulations and from real atmospheric data. In chapter 5, we apply the LWA diagnostic to an upscale error growth experiment as a metric to quantify the error at a scale ranging from the synoptic up to the planetary. In chapter 6 we present and discuss the application of the filtered LWA budget to investigate the dynamics of RWPs. This is done the framework of idealised simulations and in the context of predictability, applying our diagnostic to an operational forecast model. Finally, chapter 7 contains a summary of the results obtained in sections 4, 5 and 6 as well as our conclusions.

Chapter 2

Theoretical background

In this chapter we present some aspects of the theory of Rossby waves and Rossby wave packets which are useful to understand and interpret our results. In particular we will emphasise the role of Potential Vorticity and Rossby wave activity, which are both of fundamental importance to describe the dynamics of Rossby waves.

Rossby wave activity is first presented in the linear theory (barotropic model and quasi-geostrophic framework) stressing out its limitations and the necessity of a formulation valid for finite amplitudes. Subsequently, finite amplitude wave activity (FAWA) is introduced in the barotropic model, quasi-geostrophic framework and in the primitive equations in isentropic coordinates and their main properties are discussed. Finally, Local Wave Activity (LWA) is presented in the same hierarchy of frameworks (barotropic model, quasi-geostrophic limit and in the primitive equations in isentropic coordinates) and a budget equation for barotropic and isentropic LWA is derived. The formulation of LWA in the primitive equations, which is presented in section 2.5.3, represents a novelty of this thesis and have been published in Ghinassi et al. (2018). The proposed formulation of the budget equations for LWA in the barotropic model and in the primitive equations are presented in sections 2.5.1 and 2.5.3 respectively, and led to the publication Ghinassi et al. (2019, manuscript submitted to the Journal of the Atmospheric Sciences).

2.1 Rossby Waves

The barotropic model on the β-plane is arguably the simplest model which can qualitatively describe the dynamics of the Rossby waves and their mechanism of horizontal propagation. The barotropic model describes the dynamics of an inviscid fluid of constant density confined between two rigid horizontal surfaces in a rotating frame of reference. Cartesian coordinates are used, where x, y are the zonal and meridional coordinates, respectively and t is time. In the barotropic model the dynamics can be entirely described in terms of the absolute vorticity q

$$q(x, y, t) = f + \zeta \,, \tag{2.1}$$

where $f = f_0 + \beta y$ is the linear Coriolis parameter ($f_0 = 2\Omega \sin \phi_0$, Ω is the Earth angular velocity and ϕ_0 a constant reference latitude) and $\beta \equiv 2\Omega a^{-1} \cos \phi_0$ (with a the radius of the Earth). This linear approximation of the full Coriolis parameter captures, to the leading order, the variation of planetary vorticity with latitude, which is crucial for the existence of Rossby waves (Andrews et al., 1987; Rhines, 2002). ζ is relative vorticity

$$\zeta(x, y, t) = \frac{\partial v}{\partial x} - \frac{\partial u}{\partial y} \,, \tag{2.2}$$

where (u, v) is the horizontal wind. The equation for absolute vorticity in the barotropic model reads

$$\frac{Dq}{Dt} = \frac{\partial q}{\partial t} + \mathbf{v} \cdot \nabla q = N_{\mathrm{q}} \,, \tag{2.3}$$

where D/Dt denotes the material derivative and N_{q} represents non-conservative source and sinks of vorticity. In a conservative (frictionless and adiabatic) flow, absolute vorticity is materially conserved (i.e. $Dq/Dt = 0$) and q plays the role of Potential Vorticity (PV). Defining a streamfunction ψ such that the horizontal wind can be written as

$$(u, v) = \left(- \frac{\partial \psi}{\partial x}, \frac{\partial \psi}{\partial y} \right) \,, \tag{2.4}$$

the relation between relative vorticity and the streamfunction is

$$\zeta = \nabla^2 \psi \ , \tag{2.5}$$

where ∇^2 denotes the Laplacian. The relation between the streamfunction and vorticity has the form of a Poisson equation:

$$\nabla^2 \psi = q - f \ . \tag{2.6}$$

This means that if the absolute vorticity distribution at a particular time is known, (2.6) can be inverted (given suitable boundary conditions) to determine the streamfunction and so the horizontal wind. This is the basic idea behind the so called *invertibility principle* and explains why the dynamics of the barotropic model can be entirely described integrating equation (2.3) in time. Another important characteristic related to the elliptic nature of (2.6) is that a given PV distribution at one location affects the solution over the whole domain, in an analogous manner as the electric field potential is affected by a point charge in electrostatics. This action-at-a-distance feature is fundamental to understand the Rossby wave propagation mechanism, as we will see in section 2.2. Some of the key aspects of the dynamics of Rossby waves waves can be described in the linear theory with the so called perturbation method (see for example Holton (2004) or Vallis (2006)). In this approach the flow is partitioned between a constant, basic flow and a perturbation, which is the local deviation of one variable from such basic state. The basic state is usually set as the zonal average and all variables are written as the sum of the constant basic state plus a small perturbation. For example PV q becomes

$$q(x, y, t) = \overline{q} + q'(x, y, t) \ , \tag{2.7}$$

where the overbar denotes the zonal mean and the prime its deviation. Substituting the so decomposed variables in equation (2.3), and neglecting the products between perturbations we finally obtain the linearised barotropic vorticity equation

$$\left(\frac{\partial}{\partial t} + \overline{u} \frac{\partial}{\partial x} \right) \zeta' + \beta v' = 0 \ . \tag{2.8}$$

Equation (2.8) can be rewritten only in terms of the streamfunction perturbation ψ' (noting that $\zeta' = \nabla^2\psi'$) yielding

$$\left(\frac{\partial}{\partial t} + \overline{u}\frac{\partial}{\partial x}\right)\nabla^2\psi' + \beta\frac{\partial\psi'}{\partial x} = 0 \; . \tag{2.9}$$

Wee seek Rossby waves as plane waves solutions of equation (2.8) of the form

$$\psi' = \Re\psi_0 e^{i(kx+ly-\nu t)} \; , \tag{2.10}$$

in which ψ_0 is a constant amplitude, $\Re$ denotes the real part, k, l are the zonal and meridional wavenumbers and ν is the wave angular frequency. The dispersion relation of Rossby waves in the barotropic model is

$$\nu(k,l) = \overline{u}k - \frac{\beta k}{k^2+l^2} \; , \tag{2.11}$$

from which the zonal phase speed c_p^x and group velocitiy c_g^x can be determined:

$$c_p^{(x)} = \frac{\nu}{k} = \overline{u} - \frac{\beta}{k^2+l^2} \; , \tag{2.12}$$

$$c_g^{(x)} = \frac{\partial\nu}{\partial k} = \overline{u} + \beta\frac{k^2-l^2}{(k^2+l^2)^2} = c_p^{(x)} + \frac{2\beta k^2}{(k^2+l^2)^2} \; . \tag{2.13}$$

The zonal phase speed of Rossby waves relative to the mean zonal wind is

$$c_p^{(x)} - \overline{u} = -\frac{\beta}{k^2+l^2} \; , \tag{2.14}$$

which implies that the zonal phase propagation is always westward relative to $\overline{u}$. The fact that the dispersion relation (2.11) depends on the zonal and meridional wavenumbers implies that Rossby waves are dispersive. The zonal group velocity indeed may be either westward or eastward with respect to the background wind. In case of a synoptic scale (in which typically $5 \leq k \leq 8$) Rossby wave propagating on a westerly zonal wind, which is a typical situation occurring in the upper troposphere in the mid-latitudes (a typical observed value in this region is $\overline{u} = 30$ m s^{-1}), the wave group

propagates eastward faster than the wave phase, leading to the development of new disturbances downstream of the existing ones. This phenomenon is called downstream development. The downstream development of Rossby waves can be explained from

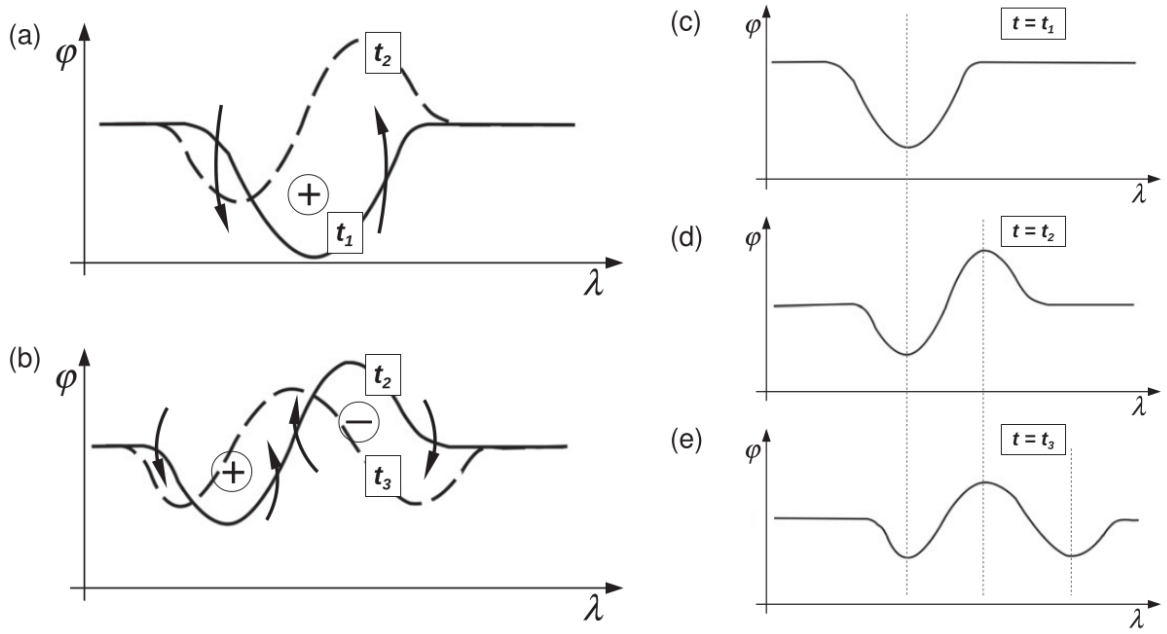

Figure 2.1: Qualitative explanation of barotropic downstream development in the framework of PV thinking. Each panel represents a map on the horizontal plane with the lines depicting contours of PV at different times t_i $(i = 1, 2, 3)$. The PV gradient of the background atmosphere is northward (i.e., upward in the figure). (left) The circled plus and minus signs represent PV anomalies; the curved arrows represent the wind field associated with these PV anomalies; the solid PV contour depicts an early stage, while the dashed contour represents the situation a short time later (i.e., after the wind had some time to advect the initial contour). (a) The time interval $t_1 < t < t_2$ and (b) time interval $t_2 < t < t_3$. (right) The scenario in a frame of reference in which the phase of the troughs and ridges is stationary. From Wirth et al. (2018).

a PV perspective in terms of the circulation induced by PV anomalies onto the background flow (action-at-a-distance), as illustrated in Figure 2.1. This brief description of Rossby waves in the barotropic model provides the fundamental concepts to derive a theory for the interaction of the waves with the mean flow, where the concepts of wave activity plays a key role. Before focusing on wave activity it is important to introduce the concept of Rossby wave packet, since it motivates the necessity of defining a local measure of wave activity.

2.2 Rossby wave packets

The presence of RWPs in the upper troposphere as an organised series of troughs and ridges has been known since the first upper air observations became available in the 1930s. (Hovmöller, 1949) with his famous troughs and ridges diagram proposed a method which clearly identified these features in the observed circulation of the upper troposphere. The concept of wave packet translates into the amplitude of the Rossby waves solutions (2.10) not being constant but slowly varying in time and space compared to their phase. The meridional wind v is widely used to identify Rossby waves as deviations from a purely zonal flow, since usually $\overline{v} \approx 0$ and v' oscillates between positive and negative values. Taking into account the Earth sphericity at one latitude circle ϕ we have

$$v'(\lambda, t) = A(\lambda, t)\cos(s\lambda - \nu t);\,, \tag{2.15}$$

where the spherical zonal wavenumber s is related to k through

$$s = ka\cos\phi;\,. \tag{2.16}$$

A popular method to quantify the RWP amplitude $A(\lambda)$ has been developed by Zimin et al. (2003) and it is based on the extraction of the envelope of the meridional wind. The algorithm consists of the Hilbert transform[1] on v at each latitude circle plus a filter to retain only a specific range of zonal wavenumbers in its Fourier spectrum. An example of RWP in the barotropic model and in the real atmosphere, identified in terms of the meridional wind v and its envelope, can be seen in Figure 2.2. Note that since v is a purely kinematic quantity it is not conserved even in a truly conservative flow. Therefore this technique for the envelope reconstruction, although useful in the identification of RWPs, it is not well suited to investigate their dynamics.

We will now review some key concepts about the dynamics of RWPs. Pedlosky

[1]Let $v(x)$ be a function of the real variable x, the Hilbert transform is defined by the linear operator $\mathcal{H}$:

$$\mathcal{H}(v)(x) = \pi^{-1}\int_{-\infty}^{\infty}\frac{v(x')}{x - x'}\,dx'\,.$$

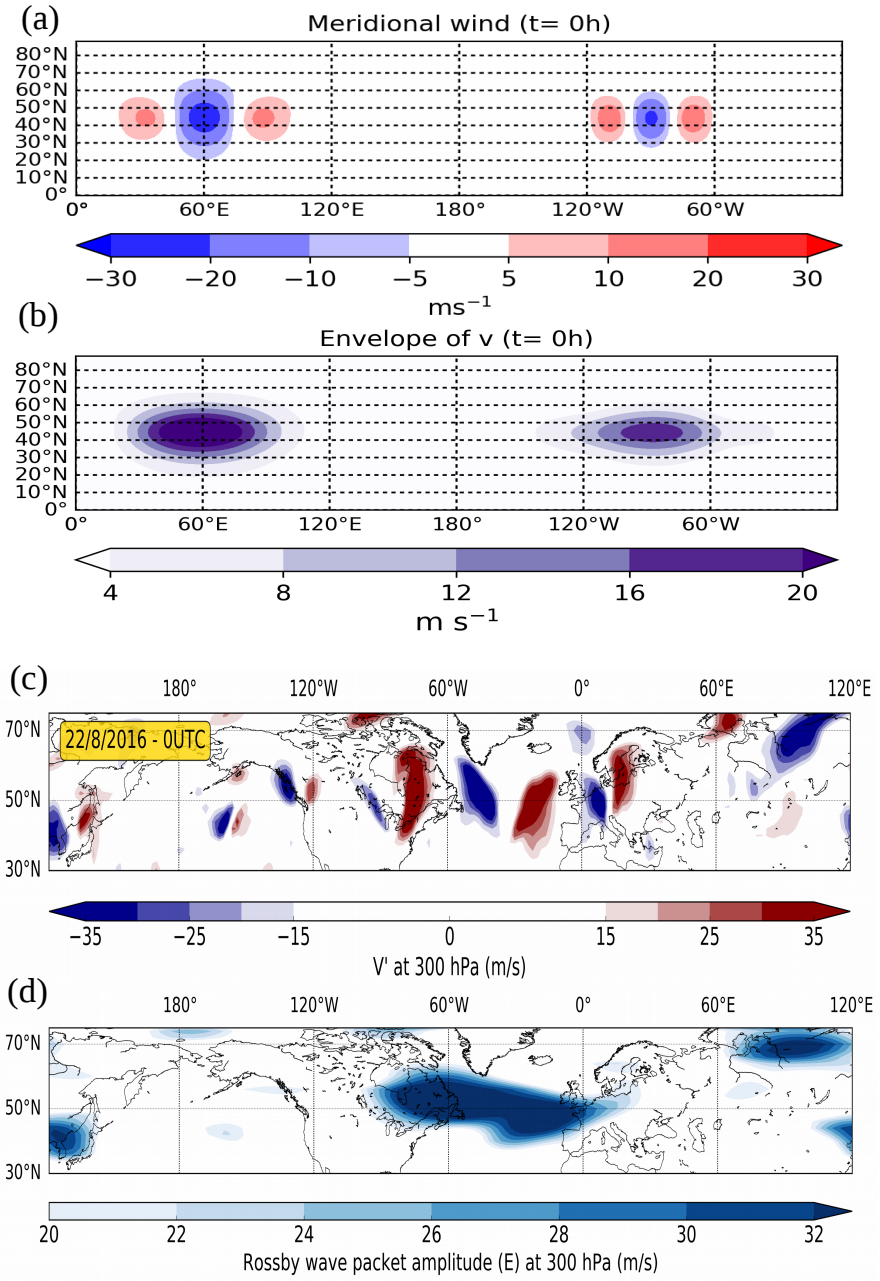

Figure 2.2: Example of RWPs with different carrier zonal wavenumbers from a barotropic simulation in terms of meridional wind V (panel (a)). Panel (b): envelope of the v field showed in (a) computed according to Zimin et al. (2003). Panel (c): meridional wind at 300 hPa and its envelope computed according to Zimin et al. (2003) (panel d). A RWP is clearly visible over the North Atlantic. Plots in (c) and (d) are a courtesy of Georgios Fragkoulidis.

(1972) was one of the first authors to investigate the dynamics of RWPs in the framework of the quasi-geostrophic theory. Pedlosky (1972) enlightened the importance of the conversion of the available potential energy stored in the baroclinicity[1] into kinetic energy for the RWP amplitude growth. This mechanism occurs until the wave packet amplitude reaches saturation. After reaching saturation, the wave packet starts to decay and its energy and momentum are transferred back to the mean flow. This phenomenon is called *wavebreaking* and is characterised by the fact that the RWPs structure appears highly nonlinear, with the individual phases becoming tilted and assuming a characteristic bow shape (Hoskins et al., 1983; James, 1994). Simmons and Hoskins (1978), corroborated what was theorised by Pedlosky while investigating the energetics of baroclinic life cycles in an idealised, primitive equations model experiment. Simmons and Hoskins (1978) found that in the zonal mean, the growth phase of these synoptic-scale eddies happens via the interaction of an initially small amplitude, unstable wave in the upper levels with the high baroclinicity in the lower levels. The decay phase instead was associated with transfer of momentum from the wave back to the mean flow and dissipative processes. The growth phase of the zonally averaged disturbances happens via the mutual interaction of Rossby waves at the lower and upper levels as in the models of baroclinic instability described by Eady (1949) and Charney (1947), whereas the decay phase occurs mainly via interaction with the zonal wind through momentum fluxes on the same vertical level. Therefore the growth and decay processes are often referred as baroclinic growth and barotropic decay. An illustrative schematic of the growth and amplification of a RWP in the upper troposphere via baroclinic instability is shown in Figure 2.3. Subsequently, other authors focused on the local (i.e. not in the zonally averaged sense) dynamics of RWPs. Lee and Held (1993b) found evidence that synoptic scale Rossby waves tend to spontaneously self-organise in wave packets in a hierarchy of idealised simulations of baroclinically unstable flows in the quasi-geostrophic and primitive equations frameworks. Chang

[1]The baroclinicity in a stably stratified atmosphere is proportional to $\nabla p \times \nabla \rho$, where p is pressure and ρ the air density. In the atmosphere a high baroclinicity is typically associated with the strong meridional temperature gradient or vertical wind shear (the two are linked by the thermal wind relation) found in the midlatitudes. A widely used metric to quantify the atmospheric baroclinicity is the maximum Eady growth rate (Lindzen and Farrell, 1980; Hoskins and Valdes, 1990) defined as $\sigma_{\max} = f|\partial \mathbf{v}/\partial z|N^{-1}$, where N is the static stability.

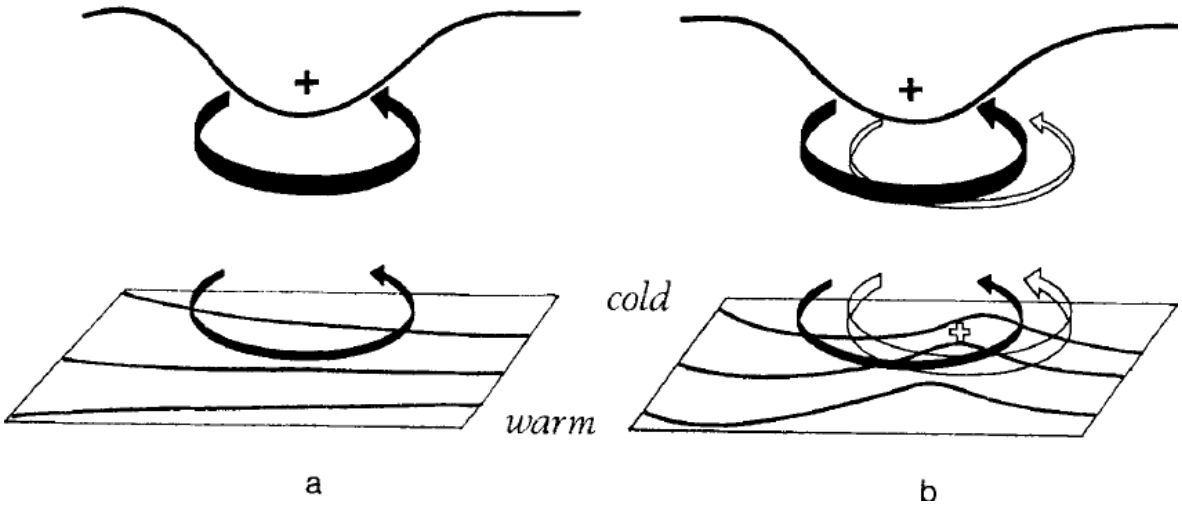

Figure 2.3: A schematic picture of baroclinic development due to the arrival of an upper air positive PV anomaly (PV trough), for example embedded in a RWP, over a low-level baroclinic region. In (a) the upper troposphere, a positive PV anomaly, indicated by a solid plus sign, has just arrived over a region of significant low-level baroclinicity. The circulation induced by the anomaly is indicated by solid arrows, and potential temperature contours are shown on the ground. The low-level circulation is shown above the ground for clarity. The advection by this circulation leads to a warm temperature anomaly somewhat ahead of the upper PV anomaly as indicated in (b), and marked with an open plus sign. This warm anomaly induces the cyclonic circulation indicated by the open arrows in (b). If the equatorward motion at upper levels advects high-PV air from the high latitudes, and the poleward motion advects low-PV subtropical air, then the action of the upper-level circulation induced by the surface potential temperature anomaly will, in effect, reinforce and amplify the upper level PV trough, as well as favour the downstream development of new PV anomalies. From Hoskins et al. (1985).

and Orlanski (1993), using the EKE budget, enlightened the role of the ageostrophic circulation in the downstream development of the wave packet. This mechanism occurs due to the ageostrophic geopotential fluxes and can originate new disturbances downstream even in regions with a lower baroclinicity. The amplitude growth of the wave packet via baroclinic conversion is generally observed in the central part of the wave packet (Chang and Orlanski, 1993), whereas the amplitude decay of the upstream edge occurs via barotropic energy transfer into the mean flow (Swanson and Pierrehumbert, 1994). However, these mechanisms of growth and decay of the amplitude of simulated RWPs are not systematically found in observed wave packets (Chang, 2001, 2005a). A more complete review about RWPs can be found in the review article of Wirth et al. 2018.

To the autor's knowlegde, an investigation of the dynamics of RWPs using LWA in the primitive equations in isentropic coordinates framework is still missing in the literature. As discussed in the introduction, this thesis aims to elucidate to what extent the LWA diagnostic we propose is able to describe the dynamics of RWPs. Furthermore, the amenability of the LWA diagnostic to deal with either model data or observations, allows one a straightforward comparison of simulated RWPs with observed ones (see sections 4 and 6).

2.3 Linear measures of wave activity

In this section we will summarise the linear theory of Rossby wave activity in the barotropic and quasi-geostrophic frameworks.

2.3.1 Barotropic β-plane

Wave activity plays a fundamental role in the interaction between waves and the mean flow (Buehler, 2009) and it quantifies the amplitude of the waves as the deviation from any given flow and a suitably defined background. Wave activity is the negative of the pseudo-momentum[1] and its physical units are m s^{-1}. Wave activity first gained

[1] According to McIntyre and Shepherd (1987) pseudo-momentum denotes the zonal specific angular momentum (divided by the radius of the Earth) associated with the waves and thus represents the

attention in meteorology during the early studies of the response of the zonally averaged atmospheric circulation in the presence of planetary waves (Charney and Drazin, 1961) or the instability related to waves interacting with sheared flows (Charney and Stern, 1962; Bretherton, 1966). The choice of the background state is a non-trivial issue in the formulation of a wave mean flow interaction theory. In the earliest approach to the problem, linear theory was used, in which the background is set as the zonal mean flow. This provides a particularly simple formulation of wave activity; however, linear theory assumes that the amplitude of the waves is small, a condition which is rarely observed in the real atmosphere (Andrews and McIntyre, 1978). According to Vallis (2006), barotropic linear wave activity is defined as

$$\mathcal{A} = \frac{1}{2}\frac{\overline{q'^2}}{\partial\overline{q}/\partial y} = -\frac{1}{2}\overline{\Delta y q'} \; . \tag{2.17}$$

The second equality in (2.17), which holds for conservative waves and assumes $\partial\overline{q}/\partial y > 0$, makes use of the linear meridional displacement Δy defined as in Andrews and McIntyre (1978) through $q' = -\Delta y \; \partial\overline{q}/\partial y$. The equation for the evolution of $\mathcal{A}$ reads (Vallis, 2006)

$$\frac{\partial \mathcal{A}}{\partial t} + \overline{v'q'} = \mathcal{N} + O(\alpha^3) \; , \tag{2.18}$$

where the term $\mathcal{N}$ represents non-conservative sources and sinks of wave activity. Equation (2.18) states that in case of a conservative flow the rate of change of wave activity is given by the eddy vorticity flux. The cubic term $O(\alpha^3)$ on the right hand side, where α is a non-dimensional measure of the wave amplitude, arises from neglecting the products of perturbation upon linearisation. This term includes the advection of wave activity by the eddies, and it turns out that for large amplitude waves its magnitude may be similar to the one of the other terms. This is why $\mathcal{A}$ is called *small amplitude* wave activity. The relation between the eddy vorticity flux and the eddy momentum flux in the barotropic model reads (Vallis, 2006)

$$\overline{v'q'} = -\frac{\partial}{\partial y}(\overline{u'v'}) \; . \tag{2.19}$$

force exerted by the waves onto the mean flow.

This means that (**??**) can be rewritten in the flux form

$$\frac{\partial \mathcal{A}}{\partial t} + \nabla \cdot \mathbf{F} = \mathcal{N} + O(\alpha^3) \ , \tag{2.20}$$

where $\mathbf{F} = (0, -\overline{u'v'})$. The conservation relation (2.20) is known as *generalised Eliassen-Palm (E-P) relation* and the flux $\mathbf{F}$ is known as the generalised E-P flux (Andrews and Mcintyre, 1976). The E-P relation states that in a conservative flow and with suitable boundary conditions the total (i.e integrated over the whole domain) $\mathcal{A}$ does not change with time. In addition, in the E-P relation it is possible to clearly distinguish between the conservative dynamics of $\mathcal{A}$ related to the divergence of $\mathbf{F}$ and the non-conservative processes. This is in contrast with other kinematic quantities used to diagnose waves dynamics such as the Eddy Kinetic Energy (EKE), whose budget equation contains additional adiabatic sources and sinks (Orlanski and Katzfey, 1991). The rate of change of the zonally averaged zonal wind in the barotropic model is

$$\frac{\partial \overline{u}}{\partial t} = -\frac{\partial}{\partial y}(\overline{u'v'}) \ , \tag{2.21}$$

which combined with (2.18) and (2.19) gives the so called *nonacceleration theorem* (Charney and Drazin, 1961)

$$\frac{\partial}{\partial t}(\mathcal{A} + \overline{u}) = \mathcal{N} + O(\alpha^3) \ . \tag{2.22}$$

For linear and conservative waves (2.22) states that the sum of $\mathcal{A}$ and $\bar{u}$ is constant, meaning that the arrival of a Rossby wave is associated with a reduction of the zonal mean zonal flow. Although linear theory provides a qualitatively correct interpretation of the interaction of Rossby wave with the mean flow it suffers from the fact that its conservation relation and nonacceleration theorem are valid only up to $O(\alpha^2)$, preventing their quantitative use in case of large amplitude waves. Another limitation of $\mathcal{A}$ is that it cannot be computed from any PV field. In particular, when $\partial\overline{q}/\partial y = 0$, $\mathcal{A}$ diverges and this happens for example when the reference PV profile is non monotonic along the meridional direction.

2.3.2 Barotropic model on the sphere

The theory of wave activity on the barotropic β-plane can be extended to spherical geometry without any particular difficulties. We now present the wave activity formulation and its conservation relation including spherical geometry, since we will make use of it in the barotropic simulation experiment of section 4.1.

The main difference between the description of a barotropic flow on the sphere and the β-plane approximation is that in the former we consider the full variation of the Coriolis parameter with latitude. In spherical geometry (where ϕ and λ denote latitude and longitude, respectively, and a is the radius of the Earth) the absolute vorticity reads

$$q(\lambda, \phi, t) = f + \zeta \ , \tag{2.23}$$

where now, $f = 2\Omega \sin\phi$ is the full Coriolis parameter and in

$$\zeta(\lambda, \phi, t) = \frac{1}{a\cos\phi}\left[\frac{\partial v}{\partial \lambda} - \frac{\partial}{\partial \phi}(u\cos\phi)\right] \ , \tag{2.24}$$

the derivatives are calculated on the sphere. The small amplitude barotropic wave activity on the sphere $\mathcal{A}$ reads (Held and Phillips, 1987):

$$\mathcal{A}_s = \frac{1}{2\gamma}\overline{q'^2} \tag{2.25}$$

where $\gamma = a^{-1}\frac{\partial \overline{q}}{\partial \phi}$. The nonacceleration theorem and generalised E-P relation have the same form of (2.22) and (2.20) respectively, but with the divergence operator considered in spherical coordinates. The E-P relation expresses the conservation of the wave activity integrated on the sphere, and the spherical variant of the generalised E-P flux reads

$$\mathbf{F} = a\cos\phi(0, -\overline{u'v'}) \ . \tag{2.26}$$

2.3.3 Quasi-geostrophic wave activity

A qualitative description of the interaction of Rossby waves with the mean flow can be extended to a three-dimensional stably stratified atmosphere under the quasi-geostrophic

(QG) approximation. The main idea behind the QG approximation is that the atmospheric motions occur approximately under geostrophic balance[1]. The QG theory is thus suitable to describe the large scale, low frequency motions observed in the extratropics. A key quantity is the the quasi-geostrophic Potential Vorticity (QGPV), which in a QG, conservative flow is materially conserved following the geostrophic wind. The dynamics of a QG flow can be entirely described in terms of QGPV, which can be inverted to determine the streamfunction (and therefore wind and temperature) in an analogous way as in the barotropic model. A complete description of the QG theory and the derivation of the QGPV is given for example in Andrews et al. (1987) or Hoskins and James (2014). To apply the QG formalism to meteorological data it is opportune to consider the QG theory including the Earth spherical geometry. The use of the QG theory in spherical coordinates requires some carefulness, since its formalism is not anymore exact as in the β-plane approximation (Andrews et al., 1987). A fair compromise, which does not render the theory too complicated, consists in considering the full variation of the Coriolis parameter f with latitude in (2.27) (Vallis, 2006; Nakamura and Solomon, 2010) bearing in mind that this implies that even the geostrophic wind satisfies geostrophic balance only approximately (the error committed however is small in the extratropics (Nakamura and Solomon, 2010)). Under these assumptions we define QGPV q_g as in Nakamura and Solomon (2010)

$$q_g(\phi, \lambda, z, t) = f + \zeta + \frac{f}{\rho_0}\frac{\partial}{\partial z}\left[\frac{\rho_0(\theta - \tilde{\theta})}{\partial\tilde{\theta}/\partial z}\right], \tag{2.27}$$

where ζ is the relative vorticity defined in (2.24), $\rho_0 \propto e^{-z/H}$ is the air density θ is potential temperature[2], and $\tilde{\theta}$ is the global mean potential temperature. Here $z =$

[1]Geostrophic balance is satisfied when the Coriolis force is exactly balanced by the pressure gradient force.

[2]Potential temperature θ is defined as:

$$\theta := T\left(\frac{p}{p_0}\right)^{\frac{R}{c_p}},$$

where T is temperature, p is pressure, p_0 is a reference pressure (usually $p_0 = 1000$ hPa), R is the dry air constant and c_p the air specific heat at constant pressure. In an adiabatic atmosphere potential temperature is materially conserved ($\frac{D\theta}{Dt} = 0$), and air parcels move along surfaces of constant θ. In the atmosphere, θ is often used as a vertical coordinate, and given that specific entropy is proportional to potential temperature, the horizontal surfaces in which θ is constant are called *isentropic surfaces*.

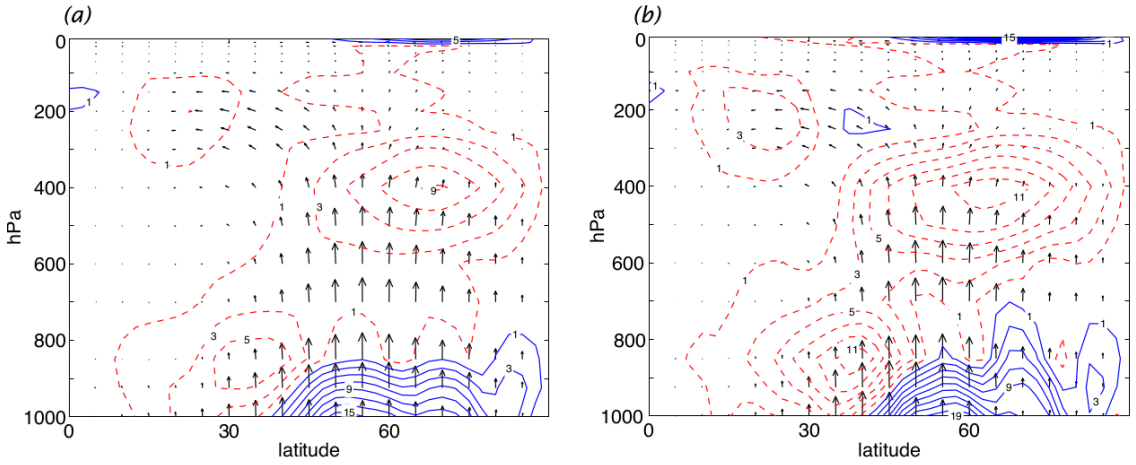

Figure 2.4: QG Eliassen-Palm flux $\mathbf{F}_{\mathrm{QG}}$ (arrows) and its divergence (contours, with intervals of 2 m s^{-1} per day, zero contour omitted) in the Northern Hemisphere computed from reanalysis. Solid contours denote divergence, and dashed contours denote convergence. Vertical coordinate is pressure. (a) Annual mean, (b) DJF (December-January-February). From Vallis (2006) p.544.

$-H\ln(p/p_0)$ denotes pressure pseudo-height (H is an scale height, p is pressure and p_o a reference pressure value) which is used as vertical coordinate.

In the QG framework, small amplitude wave activity $\mathcal{A}_{\mathrm{QG}}$ reads (Andrews et al., 1987)

$$\mathcal{A}_{\mathrm{QG}} = \frac{1}{2} a \rho_0 \frac{\overline{q_g'^2}}{\overline{q}_{gy}} , \tag{2.28}$$

where $\overline{q}_{gy}$ is the meridional gradient of the zonal mean of QGPV. As in the barotropic model, for conservative waves, defining a linear meridional displacement Δy through $q_g' = -\Delta y \overline{q}_{gy}$ (Andrews and McIntyre, 1978), equation (2.28) can be rewritten as

$$\mathcal{A}_{\mathrm{QG}} = -\frac{1}{2} a \rho_0 \overline{\Delta y q_g'} , \tag{2.29}$$

which gives a more intuitive representation of $\mathcal{A}_{\mathrm{QG}}$ in terms of the QGPV anomaly times the meridional displacement associated with the disturbance. $\mathcal{A}_{\mathrm{QG}}$ obeys the generalised E-P relation (2.20), and nonacceleration theorem in a similar form of (2.22) (in the QG framework an additional term related to the residual meridional circulations is present on the right hand side of (2.22), (Andrews and Mcintyre, 1976)). In case

of linear waves, when it is possible to define a group velocity $\mathbf{c}_g$, the E-P flux is proportional to the group velocity of the waves in the meridional–vertical plane, namely $\mathbf{F}_{\mathrm{QG}} = \mathcal{A}_{\mathrm{QG}}\mathbf{c}_g$. Therefore the QG E-P flux has been used to diagnose the propagation of Rossby wave activity (in the zonally averaged sense) from the observed atmospheric circulation (Edmon et al., 1980). The explicit form of the QG E-P flux $\mathbf{F}_{\mathrm{QG}}$ reads (Vallis, 2006)

$$\mathbf{F}_{\mathrm{QG}} = (F^{(\phi)}_{\mathrm{QG}}, F^{(z)}_{\mathrm{QG}}) = a\cos\phi\rho_0[-\overline{u'_g v'_g}, f_0\overline{v'_g\theta'}/(\partial\theta_0/\partial z)] \,, \tag{2.30}$$

and its divergence on the meridional–vertical plane is

$$\nabla\cdot\mathbf{F}_{\mathrm{QG}} = (a\cos\phi)^{-1}\left(\frac{(F^{(\phi)}_{\mathrm{QG}}\cos\phi)}{\partial\phi} + \frac{\partial F^{(z)}_{\mathrm{QG}}}{\partial z}\right) .$$

The meridional component of the E-P flux $F^{(\phi)}_{\mathrm{QG}}$ represents the eddy momentum flux, whereas $F^{(z)}_{\mathrm{QG}}$ is the meridional eddy heat flux. In the baroclinic life cycles experiments discussed in section 2.2, the upward eddy heat flux dominates the RWPs baroclinic growth stage, whereas the decay phase of the wave packets occurs primarily via the divergence of the eddy momentum flux. However, this generally holds for the zonally averaged flow and it is not always true in the local sense i.e. for individual wave packets and their individual phases (Chang, 2001, 2005a).

$\mathbf{F}_{\mathrm{QG}}$ and its divergence, computed from meteorological data are shown in Figure 2.4. The picture which emerges from the observed E-P flux is that wave activity is exported from the lower levels of the midlatitudes towards the upper troposphere. The generalized E-P relation (2.20) and nonacceleration theorem (2.22) imply that a positive (negative) divergence of the E-P flux is associated to a reduction (increase) of wave activity and a tendency to accelerate (decelerate) the zonal mean wind. Therefore the observed divergence of $\mathbf{F}_{\mathrm{QG}}$ states that wave activity is increased in the upper troposphere and decreased in the lower troposphere. Due to the nonacceleration theorem, this means that the zonal wind is reduced in the upper troposphere and increased close to the surface, where westerlies are observed despite friction. This results in a more barotropic structure of the jet stream along the vertical.

The quasi-geostrophic formulation of wave activity and its flux thus provide a powerful tool to describe the dynamics of Rossby waves and how their interact with the mean flow. However the formulation discussed in this section is undermined by the small amplitude and QG assumptions. In addition, the formulations of wave activity discussed until now are defined in terms of the zonally averaged circulation, and therefore are not useful to diagnose the dynamics of transient, zonally propagating RWPs. In the next two sections we will discuss these issues first describing a finite amplitude wave activity formulation (which allows a quantitative use of the finite amplitude versions of (2.22) and (2.20)) and then extending it to local wave activity, in order to be able to diagnose the longitudinal propagation of RWPs.

2.4 Finite Amplitude Wave Activity

"In the past there have been several successful attempts to formulate finite amlitude wave activity theories. Notable examples are the Casimir impulse wave activity (Killworth and McIntyre, 1985; McIntyre and Shepherd, 1987), the Generalized Lagrangian Mean theory (Andrews and McIntyre, 1978), or, more recently, the wave activity in the primitive equations proposed by Methven (2013). Unfortunately, these measures of wave activity have some issues. For example, the Casimir impulse wave activity, although obeying an exact conservation relation, does not possess an exact nonacceleration theorem and moreover tends to be very filamentary and fragmented when computed from a given PV field (Huang and Nakamura, 2016), which prevents a straightforward identification of whole RWP structures. The Generalized Lagrangian Mean theory is often problematic to compute from data (Methven, 2013), and the wave activity introduced by Methven (2013) is defined in the zonal mean and requires the computation of the Generalized Lagrangian Mean background state (McIntyre, 1980), which must be obtained through the inversion of Ertel PV in isentropic coordinates, which is computationally rather involved."(Ghinassi et al., 2018)

As we mentioned in the introduction, a notable exception to this computational complexity is the Finite Amplitude Wave Activity (short FAWA) proposed by Nakamura and collaborators, which can be computed from atmospheric data in a fairly

straightforward manner.

In the next three subsections the FAWA of Nakamura and collaborators will be discussed in the barotropic model, QG theory and in the primitive equations in isentropic coordinates.

2.4.1 Barotropic model on the sphere

The expression for FAWA was first derived on the barotropic beta plane by Nakamura and Zhu (2010) and extended to spherical geometry in Solomon and Nakamura (2012). FAWA is defined in terms of the meridional displacement of a potential vorticity contour from zonal symmetry. Due to its finite amplitude nature it can be computed from any given PV field and furthermore posseses exact E-P relation and non-accleleration theorem. FAWA is evaluated associating to a a latitude circle ϕ a wavy PV contour of value Q such that they enclose the same area on the sphere[1]. This is done using the implicit relation

$$\iint_{q\geq Q} dS' = \iint_{\phi'\geq\phi} dS' \ . \tag{2.31}$$

wgere $dS' = a^2 \cos\phi' d\lambda d\phi'$ is the area element in spherical coordinates and ϕ' denotes the variable of integration along the meridional direction with respect to constant latitude ϕ. (2.31) establishes, at each time, a one-to-one relation between a set of latitudes and a PV profile $Q(\phi, t)$. $Q(\phi, t)$ is thus the PV value found at latitude ϕ after rearranging the full flow in a way such that the circulation along the PV contours is preserved, as in the Modified Lagrangian Mean (MLM) state defined by McIntyre (1980). Note that the profile $Q(\phi)$ is always monotonic for any given PV field. Barotropic FAWA A^* is then defined in terms of surface integral of PV as

$$A^*(\phi, t) = \frac{1}{2\pi a \cos\phi} \left(\iint_{q\geq Q} q\, dS' - \iint_{\phi'\geq\phi} q\, dS' \right) \ . \tag{2.32}$$

Given that the PV values are higher in the integration domain of the first integral compared to the second integral in (2.32), A^* is a positive definite quantity and $A^* = 0$ only in when $q = Q(\phi)$ at latitude ϕ. The expression for A^* (2.32) can be reformulated

[1]The latitude ϕ associated with the respective PV contour Q is called equivalent latitude (Butchart and Remsberg, 1986).

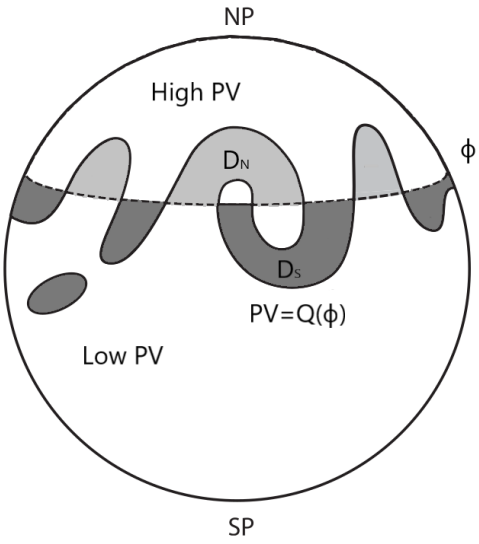

Figure 2.5: Schematic illustration of FAWA. Adapted from Nakamura and Solomon (2010).

as

$$A^*(\phi, t) = \frac{1}{2\pi a \cos\phi} \left(\iint_{D_S} q \, dS - \iint_{D_N} q \, dS \right) , \tag{2.33}$$

where D_S and D_N denote the following domains of integration:

$$D_S : [q \geq Q(\phi)] \cap [\phi' < \phi] , \tag{2.34}$$

$$D_N : [q \leq Q(\phi)] \cap [\phi' > \phi] , \tag{2.35}$$

with the subscripts S and N referring to areas respectively to the South and to the North of latitude ϕ. A schematic illustration of FAWA is shown in Figure 2.5, where D_S is the area coloured in dark grey and D_N is the area in light grey. Note that the so defined A^* can be computed from any given field, unlike its small amplitude version $\mathcal{A}$. As shown by Nakamura and Zhu (2010) A^* converges to $\mathcal{A}_s$ in the small amplitude limit. Another key difference compared to linear theory is that the finite amplitude E-P relation

$$\frac{\partial A^*}{\partial t} + \nabla \cdot \mathbf{F}^* = \mathcal{N} , \tag{2.36}$$

and nonacceleration theorem

$$\frac{\partial}{\partial t}(A^* + \overline{u}) = \mathcal{N} , \tag{2.37}$$

do not contain anymore the $O(\alpha^3)$ term, suggesting that their quantitative use is now possible for waves of any amplitude. In particular, the noncoservative term $\mathcal{N}$ in the finite amplitude formulation can be evaluated exaclty as a residual from (2.36).

Given that in the barotropic model the horizontal wind which advects the PV contours Q is nondivergent, the relation between Q and latidude ϕ is time independent in case of a conservative flow. In addition, the contribution to the rate of change of A^* from the first integral in (2.32) is zero (since q is materially conserved), while the contribution from the second integral is equal to the eddy PV flux through the latitude circle ϕ. Therefore in this conservative limit the rate of change of A^* evaluated at latitude ϕ is

$$\frac{\partial A^*}{\partial t}\cos\phi = -\cos\phi\overline{v'q'} = -\nabla\cdot\mathbf{F}^* \,, \tag{2.38}$$

and the flux $\mathbf{F}^*$ has the same form of (2.26). Unlike small amplitude wave activity, which is defined entirely in terms of Eulerian quantities, FAWA is partly Lagrangian in latitude, since it is defined in terms of material contours of PV associated to latitudes through (2.31).

2.4.2 Quasi-geostrophic variant

Barotropic and QG FAWA are closely related. Nakamura and Solomon (2010) defined QG FAWA $\mathcal{A}^*_{\mathrm{QG}}$ in terms of surface integrals of QGPV q_g on the sphere (QGPV is defined according to (2.27). This yields

$$A^*_{\mathrm{QG}}(\phi,z,t) = \frac{1}{2\pi a\cos\phi}\left(\iint_{q_g\geq Q} q_g\, dS' - \iint_{\phi'\geq\phi} q_g\, dS'\right) \,, \tag{2.39}$$

where in the relation (2.31) q is replaced by q_g. The associated E-P relation reads

$$\frac{\partial A^*_{\mathrm{QG}}}{\partial t} + \nabla\cdot\mathbf{F}^*_{\mathrm{QG}} = \mathcal{N} \,. \tag{2.40}$$

In a conservative flow, and ignoring the the divergence of $f(\phi)$ the equation for the evolution of $\mathbf{F}^*_{\mathrm{QG}}$ reduces to (Nakamura and Solomon, 2010)

$$\frac{\partial A^*_{\mathrm{QG}}}{\partial t}\cos\phi = -\cos\phi\overline{v'q'_g} = -\frac{1}{\rho_0}\nabla\cdot\mathbf{F}^*_{\mathrm{QG}}\ . \tag{2.41}$$

In the conservative limit therefore the E-P flux associated with $\mathbf{F}^*_{\mathrm{QG}}$ has the same form of its small amplitude counterpart defined in (2.30). Note also that in the small amplitude limit A^*_{QG} converges to $\mathcal{A}_{\mathrm{QG}}$ (Nakamura and Solomon, 2010).

A^*_{QG} has been used by Nakamura and collaborators to quantify the impact of the waves on the zonal mean geostrophic wind Δu taking the advantage that for conservative waves holds

$$\Delta u = \overline{u}_g - u_{\mathrm{REF}}\ , \tag{2.42}$$

where $u_{\mathrm{REF}}(\phi, z)$ is the zonally symmetric reference state associated with the PV distribution of the MLM state $Q(\phi, z)$. It follows that the time evolution of u_{REF} is related only to non-conservative processes. The advantage of the QG formulation resides in its linearity yielding $u_{\mathrm{REF}}(\phi, z)$ not too difficult to compute from $Q(\phi, z)$. On the other hand, the price to pay is the fact that the quasi-geostrophic theory is applicable only in the extratropics. Although it is possible to evaluate A^*_{QG} and the mean flow adjustment globally, their values in the subtropics (where the QG assumption breaks down) should not be considered seriously. The QG analysis of FAWA of Nakamura and Solomon (2010) in fact revealed a meaningful picture in the extratropics, where maxima of A^*_{QG} are found in the upper troposphere associated with synoptic eddies. In the upper troposphere between the subtropics and the equator spurious high values of wave activity were found. This wave activity arose from wavy QGPV contours crossing the equator, a situation which is unphysical, since inertially unstable. A quantitatively correct global wave activity analysis therefore is not possible in the QG framework.

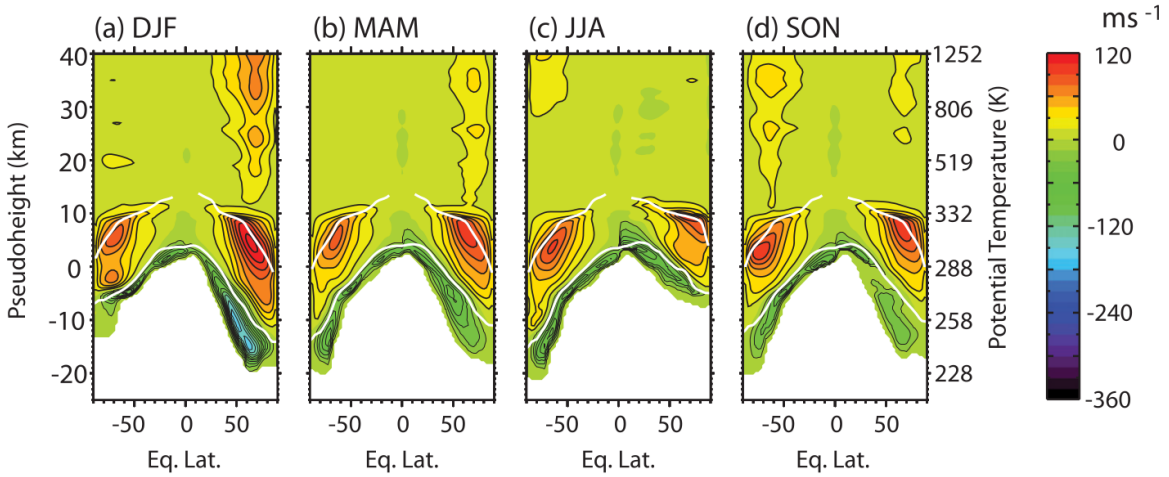

Figure 2.6: Seasonal climatology of wave activity as a function of equivalent latitude and pseudoheight based on the 19792001 daily ERA-40 data. (The corresponding potential temperature is shown on the right vertical axis.) The upper white curves are 2.5-PVU (1 PVU $\equiv 10^{-6}$ K m^2 s^{-1} kg^{-1}) contours and the lower white curves represent the zonal-mean surface potential temperature. The regions not sampled by the atmosphere are masked in white. (a) DecemberFebruary, (b) MarchMay, (c) JuneAugust, and (d) SeptemberNovember. The contour interval is 15 m s^{-1} , negative values are plotted with thin solid contours, and the zero contours are suppressed. From Nakamura and Solomon (2011).

2.4.3 Primitive equation variant

FAWA in the primitive equations in isentropic coordinates is defined in terms of Ertel PV (Ertel, 1942). Ertel PV P in isentropic coordinates reads

$$P(\phi, \lambda, \theta, t) = \frac{f + \zeta_\theta}{\sigma} \ , \tag{2.43}$$

where the subscript θ in the relative vorticity means that derivatives are evaluated along the quasi horizontal isentropic surfaces and $\sigma = -g^{-1}\frac{\partial p}{\partial \theta}$ is the isentropic layer density (where g is the Earth gravitational acceleration). If the flow is conservative, Ertel PV is materially conserved following the full flow, i.e. $\frac{DP}{Dt} = 0$. Ertel PV can be inverted to obtain the quasi-balanced component of the flow, however, unlike in the barotropic and QG frameworks, the relation between P and the associated streamfunction is non-linear (Hoskins et al., 1985). Ertel PV in isetropic coordinates has been widely used to identify upper tropospheric Rossby waves as well as their interaction with weather phenomena at the surface (Hoskins et al., 1985). The inversion of individual PV anomalies to obtain the associated circulation (the so called piecewise PV inversion, (Davis, 1992)) is the main idea behind the wind partitioning technique described in section 3.3.

An issue related to the use of θ as vertical coordinate arises when an isentrope partially lies below the ground. In this work however we will summarise the key points of the formulation of Nakamura and Solomon (2011) assuming, for simplicity, that the isentropes lie above the ground over the domain of interest. The formulation of FAWA including isentropic surfaces which intersects the ground is given in Nakamura and Solomon (2011). In the primitive equations variant the relation between latitude ϕ and $Q(\phi, \theta)$ is defined in terms of integrals of isentropic layer mass through

$$\iint_{q \geq Q} dM' = \iint_{\phi' \geq \Phi} dM' \ , \tag{2.44}$$

where $dM' = \sigma dS'$. FAWA at a given latitude ϕ is then defined in terms of surface integrals of mass-weighted Ertel PV as

$$A^*_{\mathrm{PE}}(\phi, \theta, t) = \frac{1}{2\pi a \cos\phi} \left(\iint_{P \geq Q} P\, \sigma \, dS \ - \iint_{\phi' \geq \phi} P\, \sigma \, dS \right) \ . \tag{2.45}$$

In the framework of the primitive equations, the isentropic horizontal wind which advects the PV contours Q may be divergent, which means that there can be a mass flux through the latitude circle ϕ. Therefore the relation $Q(\phi, \theta, t)$ depends on time even for a purely conservative flow.

The equation for the evolution of A^*_{PE} cannot be written in terms of a pure divergence of a flux, as for its barotropic and QG counterparts, due to an extra term (which involves a time derivative) related to the pseudo-momentum exchange through gravity waves (Nakamura and Solomon, 2011). A way to overcome this problem is to define a "pseudo-divergence" operator as in Tung (1986). In general, the contribution to the total A^*_{PE} from gravity waves is smaller compared to Rossby waves (Tung, 1986; Methven, 2013).

The PE formulation of FAWA provides a correct global picture of the distribution of wave activity, including the tropical and equatorial regions. A climatogy of A^*_{PE} is shown in Figure 2.6, where the wave activity maxima in the upper troposphere are associated with baroclinic eddies in the extratropics. Note that A^*_{PE} identifies the maxima related to baroclinic eddies poleward with respect to the one observed using other Eulerian diagnostics such as EKE (see discussion in section 4.3). On the other hand, disadvantage of the PE formulation is that the linearity of the QG formalism is lost, and the computation of the reference state and the mean flow adjustment induced by the eddies involves solving non-linear equations.

2.5 Local Finite Amplitude Wave Activity (LWA)

As discussed in the introduction, the formulations of linear and finite amplitude wave activities presented until now are defined in terms of zonally averaged quantities and therefore are not well suited to diagnose the dynamics of transient synoptic-scale RWPs. In this section we will present the theory of LWA starting from the barotropic model on the sphere and in the the quasi-geostrophic theory following Huang and Nakamura (2016). Then, we will introduce the LWA in the primitive equations in isentropic coordinates following Ghinassi et al. (2018), which is a novelty this thesis. Other novel aspects of this work are the budget equations for the evolution of LWA, which will be

formulated for the barotropic and isentropic LWA, based on the submitted manuscript Ghinassi et al. (2019).

2.5.1 Barotropic model on the sphere[1]

Following Huang and Nakamura (2016), but taking into account spherical geometry, LWA at a given latitude circle ϕ is defined as

$$A(\lambda,\phi,t) = \frac{1}{\cos\phi}\left(\int_{l_S}[q(\lambda,\phi',t) - Q(\phi,t)]\, a\cos\phi' d\phi' + \int_{l_N}[Q(\phi,t) - q(\lambda,\phi',t)]\, a\cos\phi' d\phi'\right) , \tag{2.46}$$

where l_N and l_S are the arcs along the meridian which satisfy the conditions

$$l_N : \quad q \le Q,\ \phi' \ge \phi\ , \tag{2.47}$$

$$l_S : \quad q \ge Q,\ \phi' \le \phi\ . \tag{2.48}$$

The variable $Q(\phi,t)$ represents a specific value of PV which at any time is uniquely related to a given latitude ϕ through the relation 2.31. Note that A is always non-negative by construction. Denoting the meridional diaplacement of the wavy PV contour $Q(\phi)$ from its reference position ϕ by $\Delta\phi(\lambda,\phi,t)$, (2.46) can be rewritten in a compact form as

$$A(\lambda,\phi,t) = -\frac{1}{\cos\phi}\int_{\phi}^{\phi+\Delta\phi}(q-Q)\, a\cos\phi' d\phi'\ ; \tag{2.49}$$

note that $\Delta\phi$ is defined positive northward and can be multivalued in case of multiple crossings of the PV contour along a meridian (a situation which happens when PV contours become highly distorted).

As can readily be verified, the zonal average of A at any given time recovers FAWA A^* evaluated at latitude ϕ. , i.e.

$$\frac{1}{2\pi}\int_0^{2\pi} A(\lambda,\phi)\, d\lambda = A^*(\phi)\ . \tag{2.50}$$

[1]The parts of this section in quotation marks have been published in Ghinassi et al. (2018) or submitted in Ghinassi et al. (2019).

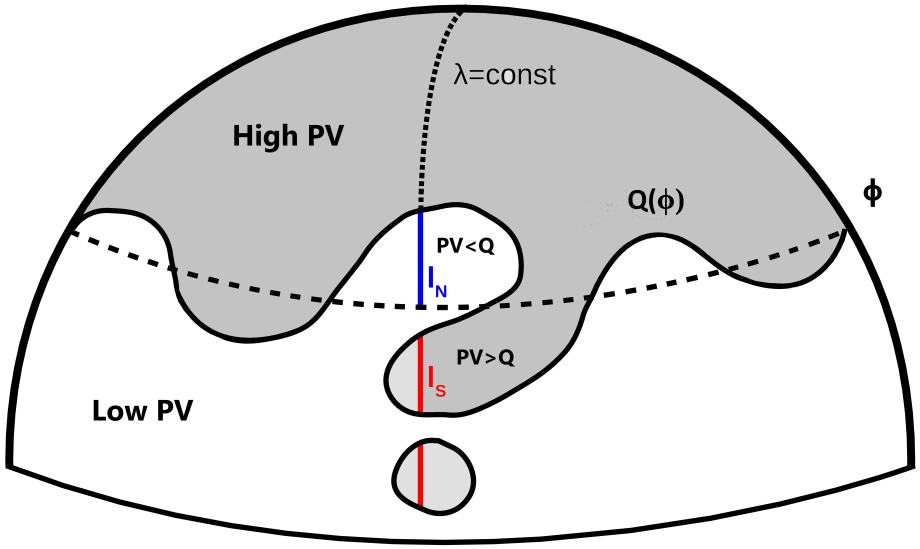

Figure 2.7: Schematic illustration of LWA. Adapted from Ghinassi et al. (2018).

A more intuitive understanding of A can be achieved overcoming the complexity related to spherical geometry. "Let $y = a \sin\phi$, then the expression (2.49) can be written as

$$A(\lambda, \phi) \cos\phi = -\int_{y}^{y+\Delta y} (q - Q)\, dy' \ , \tag{2.51}$$

The last formulation indicates that LWA can be considered to be a PV anomaly $(q-Q)$ integrated over a certain meridional range Δy. This is analogous to the local (in longitude) contribution to small-amplitude wave activity in (2.17); however, in stark contrast with in (2.17), the expression (2.51) does not require any small amplitude assumption"(Ghinassi et al., 2018). Note also that the integration along the meridional implies that LWA is partly-Lagrangian in latitude as FAWA.

We will now present the derivation of the budget equation for the barotropic LWA. "Differentiating (2.49) with respect to time and applying the Leibniz rule one obtains

$$\begin{aligned} \frac{\partial A}{\partial t} \cos\phi = -\int_{\phi}^{\phi+\Delta\phi} \frac{\partial}{\partial t}[(q - Q)]\, a \cos\phi' d\phi' + \\ -\frac{\partial \Delta\phi}{\partial t}[(q - Q) a \cos\phi']_{\phi'=\phi+\Delta\phi} + \frac{\partial \phi}{\partial t}[(q - Q) a \cos\phi']_{\phi'=\phi} \ . \end{aligned} \tag{2.52}$$

The second term on the right hand side vanishes because $q(\lambda, \phi + \Delta\phi, t) = Q(\phi, t)$ at any time (from the definition of $Q(\phi, t)$), and the third term on the right hand side

vanishes because ϕ is a coordinate, which does not explicitly depend on time. By contrast, the reference PV distribution $Q(\phi, t)$ may vary with time in the presence of non-conservative processes. We thus obtain

$$\begin{aligned} \frac{\partial A}{\partial t} \cos\phi &= -\int_{\phi}^{\phi+\Delta\phi} \frac{\partial q}{\partial t} a \cos\phi' d\phi' \\ &+ \int_{\phi}^{\phi+\Delta\phi} \frac{\partial Q}{\partial t} a \cos\phi' d\phi' \ . \end{aligned} \tag{2.53}$$

From (2.3) we have

$$\frac{\partial q}{\partial t} = -\nabla \cdot (\mathbf{v} q) + N_q \ . \tag{2.54}$$

Substituting this into (2.53) and carefully distinguishing between ϕ and ϕ' we finally obtain

$$\frac{\partial A}{\partial t} \cos\phi = T_{\mathrm{C}} + T_{\mathrm{Q}} + T_{\mathrm{N}} \ , \tag{2.55}$$

where

$$T_{\mathrm{C}} = \int_{\phi}^{\phi+\Delta\phi} \nabla' \cdot [(q - Q)\mathbf{v}] \, a \cos\phi' d\phi' \ , \tag{2.56a}$$

$$T_{\mathrm{Q}} = \int_{\phi}^{\phi+\Delta\phi} \frac{\partial Q}{\partial t} a \cos\phi' d\phi' \ , \tag{2.56b}$$

$$T_{\mathrm{N}} = -\int_{\phi}^{\phi+\Delta\phi} N_{\mathrm{q}} \, a \cos\phi' d\phi' \ . \tag{2.56c}$$

The term T_{C} represents the local rate of change of LWA through conservative dynamics, which includes advective processes and momentum exchange with the mean flow. The term T_{Q} arises from the diabatic modification of $Q(\phi, t)$ and represents the non-local, non-conservative impact that remote processes may have on A. The term T_{N} represents non-conservative processes affecting the LWA evolution more locally. Note that T_{C} and T_{N} are truly local only in longitude, since their values on a given point involve an integration in the meridional direction" (Ghinassi et al., 2019).

In the barotropic model and for a conservative flow we have that the dynamics reduces to

$$\frac{\partial A}{\partial t} \cos\phi = T_{\mathrm{C}} \ . \tag{2.57}$$

It can be shown (here we follow a similar derivation as in the Appendix B of Huang and Nakamura (2016) but for barotropic LWA) that when this is the case, the term T_{C} in (2.57) can be expressed as the divergence of a flux. According to Huang and Nakamura (2016), this LWA flux $\mathbf{F}$ consists of the sum of an advective flux $\mathbf{F}_{\mathrm{adv}}$ and the local E-P flux $\mathbf{F}_{\mathrm{EP}}$, i.e.:

$$\frac{\partial A}{\partial t}\cos\phi = T_{\mathrm{C}} = -\nabla\cdot\mathbf{F}\ , \tag{2.58}$$

where

$$\mathbf{F} = \mathbf{F}_{\mathrm{adv}} + \mathbf{F}_{\mathrm{EP}}\ . \tag{2.59}$$

In the barotropic model, the explicit form of $\mathbf{F}_{\mathrm{adv}}$ is

$$\mathbf{F}_{\mathrm{adv}} \equiv \left[u_{\mathrm{REF}}A - \int_{\phi}^{\phi+\Delta\phi}(u_e q_e)\, a\cos\phi' d\phi', 0\right]\ , \tag{2.60}$$

where the subscripts e denote the eddy variable defined as perturbations from the background state, which will be defined below (see equations (2.63)). The first term in the zonal component of $\mathbf{F}_{\mathrm{adv}}$ is the advection of LWA by the mean flow, whereas the second term is the Stokes drift flux of LWA and its influence only become significant at finite amplitudes (Huang and Nakamura, 2016). This term arises due to the partly Lagrangian nature of LWA and represents the difference between the Lagrangian and Eulerian mean flow (Andrews et al., 1987). The explicit form of $\mathbf{F}_{\mathrm{EP}}$ instead is

$$\mathbf{F}_{\mathrm{EP}} \equiv [v_e^2 - u_e^2, -u_e v_e\cos\phi]\ . \tag{2.61}$$

and its divergence express the interaction of LWA with the mean flow which occurs in terms of momentum fluxes. Both $\mathbf{F}_{\mathrm{adv}}$ and $\mathbf{F}_{\mathrm{EP}}$ require the knowledge of a reference state in order to be calculated. This reference state is the Modified Lagrangian Mean (MLM) state discussed in section 2.4.1. There are two equivalent ways to compute it, the first is by inverting the zonally symmetric PV distribution $Q(\phi)$ to obtain the reference zonal wind $u_{\mathrm{REF}}(\phi)$. The fact that $Q(\phi)$ is the zonally symmetric PV state which would arise by "zonalizing" the PV contour in a conservative way means that all

the pseudo-momentum associated to the eddies is returned to the mean flow and for this reason the MLM state is sometimes called "eddy-free" reference state (Huang and Nakamura, 2016). This also implies that a second way to obtain the reference wind profile is simply (Nakamura and Zhu, 2010)

$$u_{\mathrm{REF}}(\phi) = \overline{u} + \mathcal{A}^*(\phi) \ . \tag{2.62}$$

Once obtained the reference state, the eddy variables are defined at any given time as (Huang and Nakamura, 2016)

$$u_e(\lambda, \phi') = u(\lambda, \phi') - u_{\mathrm{REF}}(\phi) \ , \tag{2.63a}$$

$$v_e(\lambda, \phi') = v(\lambda, \phi') \ , \tag{2.63b}$$

$$q_e(\lambda, \phi') = q(\lambda, \phi') - Q(\phi) \ . \tag{2.63c}$$

The LWA flux is a useful tool to diagnose the group propagation of Rossby wave packets along the horizontal. If the phase of the eddies varies slowly compared to their amplitude (i.e. in the Wentzel-Kramers-Brilluin (WKB) approximation), in fact the total LWA flux reduces to the group velocity of the waves multiplied by wave activity (Plumb, 1985, 1986; Takaya and Nakamura, 2001). In addition its finite amplitude nature guarantees its applicability to waves of any amplitudes, unlike the local wave activity fluxes formulations proposed by Plumb (1985, 1986) or Takaya and Nakamura (2001), which are obtained from the linearised guasi-geostrophic equations, and therefore cannot be straightforward applied at finite amplitudes. An example of the use of the LWA flux to diagnose the propagation of both stationary and transient eddies in the barotropic model will be given in section 4.1.

2.5.2 Quasi Geostrophic variant

Quasi-geostrophic LWA at a given latitude circle ϕ is defined as (Huang and Nakamura, 2017)

$$A_{\mathrm{QG}}(\lambda,\phi,t) = \frac{1}{\cos\phi}\left(\int_{l_S}[q_g(\lambda,\phi',t) - Q(\phi,t)]\, a\cos\phi' d\phi' + \int_{l_N}[Q(\phi,t) - q_g(\lambda,\phi',t)]\, a\cos\phi' d\phi'\right), \tag{2.64}$$

replacing q with q_g in the conditions (2.47) and (2.48). As discussed in section 2.4.2 the advantage of the QG formulation is the possibility of express the evolution of LWA in terms of the divergence of a flux which contains several contributions and an easier computation of the eddy-free reference state compared to the primitive equations framework. However, the fact that the QG approximation is poor in the vicinity of the tropopause and it breaks down in the subtropics renders QG LWA unsuitable to identify RWPs over these regions, as we will show in section 4.2.

2.5.3 Primitive equation variant[1]

The limitations of the quasi-geostrophic framework discussed in the previous section motivated us to combine the developments of Huang and Nakamura (2016) with those of Nakamura and Solomon (2011) in order to develop a formulation of LWA which is valid in the primitive equations framework.

According to Ghinassi et al. (2018), LWA in the framework of the primitive equations, with potential temperature θ as a vertical coordinate and evaluated at latitude ϕ is defined as

$$A_{\mathrm{PE}}(\lambda,\phi,\theta,t) = \frac{1}{\cos\phi}\left(\int_{l_S}[P(\lambda,\phi',\theta,t) - Q(\phi,\theta,t)]\sigma\, a\cos\phi' d\phi' + \int_{l_N}[Q(\phi,\theta,t) - P(\lambda,\phi',\theta,t)]\sigma\, a\cos\phi' d\phi'\right), \tag{2.65}$$

[1]The parts of this section in quotation marks have been published in Ghinassi et al. (2018) or submitted in Ghinassi et al. (2019).

where now P and σ are Ertel PV and the isentropic layer density defined in 2.43. The relations (2.47) and (2.48) remain valid except that q is now replaced by P. The relation between a given latitude ϕ and the corresponding PV value $Q(\theta, \phi, t)$ on each isentrope is now defined through 2.44. In constrast with the barotropic and quasi-geostrophic frameworks, the isentropic wind can now be horizontally divergent, which implies that for a given ϕ the associated value $Q(\theta, \phi, t)$ may be time-dependent even for adiabatic flow. Using compact notation, A_{PE} from (2.65) can be rewritten as

$$A_{\mathrm{PE}}(\lambda, \phi, \theta, t) = -\frac{1}{\cos\phi} \int_{\phi}^{\phi+\Delta\phi} (P - Q)\sigma \, a \cos\phi' d\phi' \; . \tag{2.66}$$

We now discuss the derivation of the budget equation for isentropic LWA; the subscript PE will be omitted in the following derivation. "We start differentiating (2.66) with respect to time and obtain

$$\begin{aligned} \frac{\partial A}{\partial t} \cos\phi &= -\int_{\phi}^{\phi+\Delta\phi} \frac{\partial}{\partial t}[(P - Q)\sigma] \, a \cos\phi' d\phi' = \\ &= -\int_{\phi}^{\phi+\Delta\phi} \frac{\partial}{\partial t}(P\sigma) \, a \cos\phi' d\phi' + \\ &\quad + \int_{\phi}^{\phi+\Delta\phi} \frac{\partial}{\partial t}(Q\sigma) \, a \cos\phi' d\phi' \; , \end{aligned} \tag{2.67}$$

because the boundary terms vanish as in the barotropic case. The equation for the mass-weighted PV in isentropic coordinates (see, e.g., (3.8.8) in Andrews et al., 1987) reads

$$\frac{\partial}{\partial t}(P\sigma) = -\nabla \cdot (P\sigma \mathbf{v}) + N_1 \; , \tag{2.68}$$

where

$$N_1 = -\nabla \cdot \begin{pmatrix} -Y + \dot{\theta} \, \partial v/\partial\theta \\ X - \dot{\theta} \, \partial u/\partial\theta \end{pmatrix} \; , \tag{2.69}$$

(X, Y) denote the nonconservative terms in the isentropic horizontal momentum equation, and $\dot{\theta}$ is the material rate of change of potential temperature due to diabatic processes. In addition we have

$$\frac{\partial}{\partial t}(Q\sigma) = \frac{\partial Q}{\partial t}\sigma + Q\frac{\partial \sigma}{\partial t} \tag{2.70}$$

and

$$\frac{\partial \sigma}{\partial t} = -\nabla \cdot (\sigma \mathbf{v}) + N_2 \tag{2.71}$$

with $N_2 = \partial \left(\sigma \dot{\theta} \right) / \partial \theta$ (see, e.g., (3.8.1c) in Andrews et al. 1987). Substituting (2.68) and (2.70) into (2.67) and carefully distinguishing between ϕ and ϕ' yields

$$\frac{\partial A}{\partial t} \cos\phi = T_\mathrm{C} + T_\mathrm{Q} + T_\mathrm{N} \ , \tag{2.72}$$

where

$$T_\mathrm{C} = \int_{\phi}^{\phi+\Delta\phi} \nabla' \cdot [(P-Q)\sigma \mathbf{v}] \, a \cos\phi' d\phi' \ , \tag{2.73a}$$

$$T_\mathrm{Q} = \int_{\phi}^{\phi+\Delta\phi} \frac{\partial Q}{\partial t} \sigma a \cos\phi' d\phi' \ , \tag{2.73b}$$

and $\mathbf{v} = (u, v)$ now denotes the isentropic horizontal wind. As before, the term T_C represents the local conservative dynamics; note that this term may now include vertical RWP propagation. It contains contributions from both Rossby waves and gravity waves, even though the gravity wave contribution is generally smaller for baroclinic eddies than the Rossby wave contribution (Tung, 1986; Methven, 2013). The term T_Q represents the non-local effect due to the rate of change of $Q(\theta, \phi, t)$, which may be due to either conservative or non-conservative processes. The term T_N describes the effect of non-conservative processes, including diabatic heating, radiation, friction and PV mixing (Nakamura and Solomon, 2011; Huang and Nakamura, 2017) and its explicit expression reads

$$T_N = \int_{\phi}^{\phi+\Delta\phi} (-N_1 + N_2) \, a \cos\phi' d\phi' \ . \tag{2.74}$$

" (Ghinassi et al., 2019).

Unfortunately, in the primitive equations framework T_C cannot be expressed in terms of the divergence of a flux for the reasons discussed in section 2.4. Furthermore an hypothetical computation of the LWA requires the solution of a nonlinear equation to determine the eddy-free reference state, as well as the careful choice of vertical boundary conditions, given that some isentropes may intersect the ground.

Chapter 3

Methodology

In this chapter we will first describe the algorithm for the computation of LWA and its budget. The steps for the computation of LWA and its budget are presented in section 3.1 and are identical to the methodology section of Ghinassi et al. (2018) and Ghinassi et al. (2019). Subsequently we present a method to remove the phase information from LWA through a zonal filtering operation which allows one to identify wave packets. Two filters are proposed: the first is based on the convolution of LWA with a Hann window of fixed width (presented in section 3.2.2), while in the second (formulated in Ghinassi et al. (2018), here presented in section 3.2.1) the width of the Hann window is longitude dependent. My colleague Georgios Fragkoulids is acknowledged for the development of the algorithm to extract a local dominant zonal wavenumber based on the wavelet analysis of the meridional wind, which has been used in the longitude dependent filter (for a detailed explanation of the algorithm see Appendix A). Finally section 3.3 describes the algorithm to partition the wind into several contributions developed my colleagues Marlene Baumgart and Franziska Teubler under the supervision of Michael Riemer. We will use this technique when dealing with the LWA budget in the primitive equations in isentropic coordinates discussed in section 6. Sections 3.2.2 and 3.3 have been submitted for publication in Ghinassi et al. (2019)).

3.1 Computation of LWA from meteorological data

"We assume that meteorological data (e.g. model data or re-analysis) are given on an equidistant longitude-latitude grid on pressure levels. The algorithm to compute LWA consists of the following steps, the first two performed only in case of the computation of isentropic LWA:

1. First we select an isentrope θ which samples the upper troposphere in the mid-latitudes. We require this isentrope to intersect the tropopause, which allows us to capture the Rossby wave propagation along the associated sharp gradient of PV. We also require that the chosen isentrope does not intersect the ground within the considered domain. This condition is not too restrictive, since our analysis focuses on the upper troposphere.

2. Next we perform linear interpolation of the horizontal wind (u, v) (including the different wind contributions) and temperature T from the available pressure levels to the chosen isentrope. Then, ζ_θ is calculated from the horizontal wind field using centred differences. Isentropic density σ is first calculated on the original pressure levels (using centred differences) and then linearly interpolated to the considered isentrope (this reduces numerical noise according to (Nakamura and Solomon, 2011). In the case of an unstable vertical profile ($\sigma < 0$) at a given grid point, the value of σ at this grid point is overwritten by the average of the values at the neighboring grid points. This rarely occurs in the midlatitude upper troposphere, but is an eventuality that has to be taken into account. Finally, the Ertel PV is computed as in (2.43).

3. To compute LWA from data we first establish the relation between grid latitudes ϕ and the corresponding $Q(\phi)$ value using (2.31) and (2.44). To do this, we start with a provisional set of Q-contours, which are equidistant between the minimum and the maximum Q-value on the considered isentrope. For each of these values Q_i we evaluate the integral on the left hand side of (2.31) or (2.44), and this will be referred to as $M(Q_i)$. The integration is done by applying a simple trapezoidal rule throughout most of the domain. Particular care is exercised for

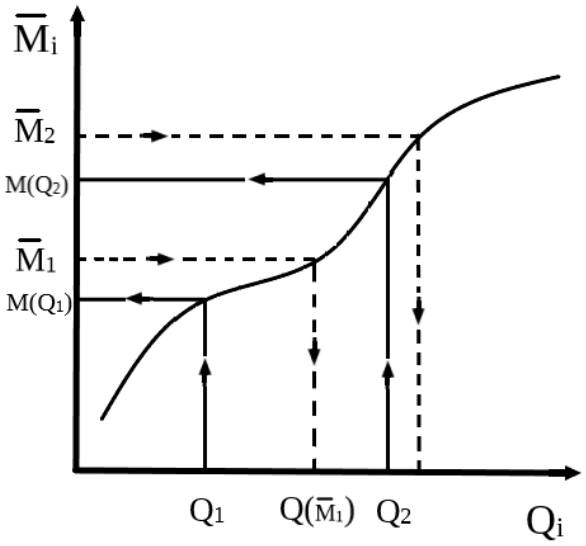

Figure 3.1: Schematic of the computation of the set of $Q(\phi)$ from $\overline{M}_i$. On the x-axis are the equispaced initial values Q_i, while on the y-axis are the values of the integrals bounded by latitude ϕ (right hand side of (2.31) or (2.44)), namely $\overline{M}_i$. Once computed $\overline{M}_i$ and $M(Q_i)$, the values of $Q(\overline{M}_i)$, which are the set of $Q(\phi)$, are determined using linear interpolation.

those grid intervals where the Q-contour intersects the respective meridian; in these grid intervals we introduce an auxiliary grid point at the intersection, which is subsequently used for an improved approximation of the integral. Thereafter we compute the right hand side of (2.31) or (2.44) for our equidistant values of ϕ, yielding a set of values called $\overline{M}_i$. The final set of $Q(\phi)$-values is obtained from the numerical relation $M(Q_i)$ with the help of linear interpolation" (Ghinassi et al., 2018). A schematic illustration of the determination of $Q(\phi)$ from $\overline{M}_i$ is provided in Figure 3.1.

4. "Once we have determined the relation between ϕ and $Q(\phi)$, we compute LWA using (2.46) for barotropic LWA or (2.65) for isentropic LWA. The numerical procedure for the integration is analogous to the one described in the previous item" (Ghinassi et al., 2018)

5. For the computation of the LWA budget according to equations (2.55) and (2.72) we proceed as follows. "For a given time step n we consider data at time $n-1$, n, and $n+1$. The time derivatives are computed using centred differences between

time steps $n+1$ and $n-1$. We then evaluate the integrals for T_{C} and T_{Q} at all three time steps $n-1$, n, and $n+1$ using the algorithms described in item 3. Subsequently, we apply some temporal averaging to the term T_{C} as

$$\tilde{T}_C^{(n)} = \frac{1}{4}\left(T_C^{(n-1)} + 2T_C^{(n)} + T_C^{(n+1)}\right) , \tag{3.1}$$

where $T_C^{(n)}$ denotes the term at the discrete time step n. This is done to make the instantaneous quantity consistent with the effective averaging due to the finite differences time derivatives in $\partial A/\partial t$ and T_{Q}. Finally, the term T_{N} is computed as a residual unless stated otherwise. Once all terms have been obtained, the zonal filter described in section 3.2.1 is applied to all of them to remove their phase information, yielding an equation for the evolution of filtered LWA, which represents the RWP amplitude" (Ghinassi et al., 2019).

3.2 Phase average of LWA through filtering

The definition of LWA involves the meridional displacement of a PV contour from it associated latitude and, therefore, contains the full phase information of the underlying Rossy wave (Huang and Nakamura, 2016; Ghinassi et al., 2018). However, when diagnosing RWPs, it is desirable to discount the phase information and, instead, diagnose the wave packet as a whole. "In the case of a wave packet with a well-defined wavelength, it is straightforward to remove the phase dependence using, e.g., the integration ov LWA over one wavelength (as done by Huang and Nakamura 2016). This approach, however, assumes the existence and an a-priori knowledge of the underlying wavelength, which is not always given. This is especially true when working with real atmospheric data, where different wave packets with different wavelengths may coexist at the same latitude band. In addition, RWPs sometimes enter a highly nonlinear stage, implying that the perturbations are not strictly wavelike any longer and the above method becomes difficult to apply" (Ghinassi et al., 2019). In the following sections we propose two different formulation of a zonal filter to discount the phase information from LWA.

3.2.1 Hann window of fixed width

"Here we propose a zonal filter to the original LWA through convolution with a Hann window (Harris, 1978). The full width at half maximum λ_d of the Hann window is allowed to depend on latitude ϕ and is defined through

$$\lambda_d(\phi) = \frac{2\pi a \cos\phi}{s_d(\phi)} \,, \tag{3.2}$$

where $s_d(\phi)$ is the so-called "dominant zonal wavenumber". The latter is defined as the wavenumber which corresponds to the maximum of the zonal Fourier spectrum of the meridional wind v. In addition we apply a moving average along latitude (with a latitudinal window of 10°) to obtain a smooth transition between the values of s_d at different latitudes." (Ghinassi et al., 2019). More details about this method can be

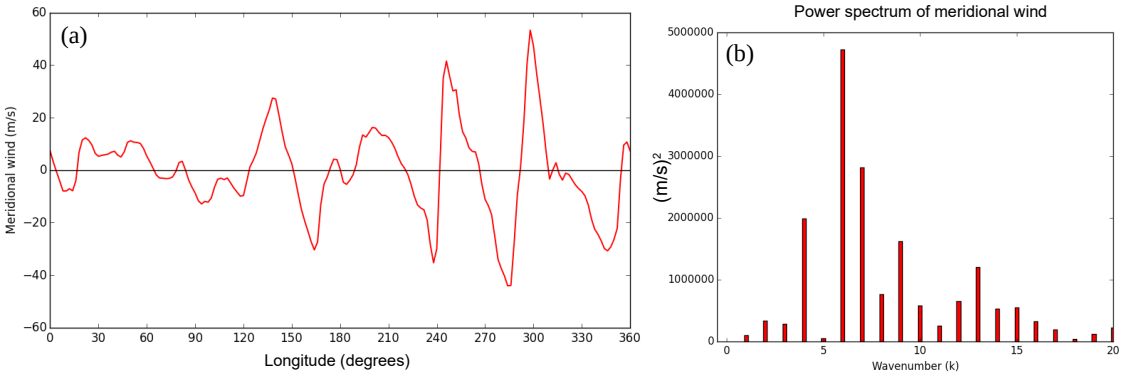

Figure 3.2: a): example of a snapshot of meridional wind v on an upper tropospheric isentrope at one latitude circle (45° N). b) Fourier Power Spectrum of the meridional wind v shown in panel a). In this case the algorithm sets the integer dominant zonal wavenumber as $s_{di}(\phi = 45°) = 6$. Once s_{di} is computed for all latitudes, a moving average along latitude (with a latitudinal window of 10°) is applied to obtain a set of real $s_d(\phi)$ which varies smoothly with latitude.

found in Figure 3.2. The proposed zonal filter may not be ideal in case different RWPs with different carrier wavenumbers are found at the same latitude. When this is the case in fact only the maximum wavenumber of the power spectrum at each latitude circle is considered. This implies that the LWA signal associated with different RWPs with different wavelengths is convolved with a Hann window of constant width along longitude yielding the phase averaging only approximately correct. On the other hand,

one advantage of this filter is the fact that is particularly cheap to compute. Another general remark regards the fact that when the Hann window does not depend on λ the filter commutes with the gradient operator. This is important to preserve the exact validity of the conservation relation for filtered LWA in the general flux form (e.g. the generalised E-P relation (2.36) and its local form (2.58)). Although in the present work we will not make use of the LWA flux when computing the LWA budget, we prefer to use this filter formulation when dealing with the phase removal of LWA and all the terms in the LWA budget equation (see section 6). Denoting the zonal filter with $\langle \dots \rangle$ we can write the filtered LWA budget equation as

$$\left\langle \frac{\partial A}{\partial t} \cos\phi \right\rangle = \langle T_{\mathrm{C}} \rangle + \langle T_{\mathrm{Q}} \rangle + \langle T_{\mathrm{N}} \rangle \, . \tag{3.3}$$

3.2.2 Hann window of variable width (Wavelet filter)

"Here we employ a general method which allows one to always extract a "local zonal wavenumber" $s_d(\lambda, \phi)$ that is local in both longitude and latitude. The method involves a zonal wavelet transform of the meridional wind and is described in more detail in the Appendix A. The zonal wavenumber $s_d(\lambda, \phi)$ is then used to compute a local wavelength as

$$\lambda_d(\lambda, \phi) = \frac{2\pi a \cos\phi}{s_d(\phi, \lambda)} \, . \tag{3.4}$$

Finally, we apply a zonal filter to the LWA field by convolution with a Hann window (Harris, 1978), which has a full width at half maximum of $\lambda_d(\lambda, \phi)$. Our algorithm works independently from the fact that the perturbations are wavelike" (Ghinassi et al., 2018). In case of an almost plane wave the algorithm removes the phase dependence and result in a smooth field that represents a wave packet. A local wavelength is particularly desirable when several wave packets co-exist at the same latitude, such that the LWA signal is convolved with a Hann window whose width is adjusted according to the local dominant wavelength of each wave packet (examples of the local wavelength computed from the meridional wind are given in Figs. A.1 and A.2 in Appendix A). When in the zonal filter the convolution with Hann window is performed with $\lambda_d(\lambda, \phi)$ depending also on longitude, the zonal filter does not commute with the gradient operator. This

implies that if the wavelet filter is chosen, the flux form of the conservation relation for filtered LWA (eq. 2.58) is not anymore exact. We will apply this wavelet filter formulation to LWA exclusively when interested purely in the visual identification of wave packets (sections 4 and 5), i.e. when we are not computing the LWA budget.

3.3 Wind partitioning in the LWA budget

"In the framework of the primitive equations, we further consider a partitioning of the conservative term T_{C} in (2.72) into different contributions. This is achieved by partitioning the wind $\mathbf{v}$ in the term T_{C} in (2.73a) following Teubler and Riemer (2016) and Baumgart et al. (2018). Owing to the fact that partial differentiation, integration, and the filter in which the Hann window has a constant width (section 3.2.1) are linear operations, this partitioning of $\mathbf{v}$ translates to a corresponding partitioning of T_{C}. We first apply Helmholtz partitioning to the horizontal wind $\mathbf{v}$ to separate the non-divergent rotational component from the divergent component $\mathbf{v}_{\mathrm{div}}$ (following Lynch (1989)). Thereafter, the rotational component is further partitioned through piecewiese PV inversion (PPVI, Davis 1992) into a contribution from the lower troposphere (called *tropospheric-deep,* $\mathbf{v}_{TSd}$) and a contribution from the upper levels (called *near-tropopause,* $\mathbf{v}_{nTP}$). The separation between the upper and lower troposphere is defined through the 600 hPa pressure level. The spatial domain used for the inversion extends between 11 – 80° N, and vertical boundary conditions for PV inversion are specified in terms of potential temperature anomalies at 875 and 125 hPa. PV anomalies are determined with respect to a time mean background state $\mathbf{v}_{\mathrm{bg}}$, which is specified as an appropriate time average. Further details can be found in Teubler and Riemer (2016). The full wind $\mathbf{v}$ can thus be written as

$$\mathbf{v} = \mathbf{v}_{\mathrm{bg}} + \mathbf{v}_{\mathrm{nTP}} + \mathbf{v}_{\mathrm{TSd}} + \mathbf{v}_{\mathrm{div}} + \mathbf{v}_{\mathrm{res}} \ , \tag{3.5}$$

where $\mathbf{v}_{\mathrm{res}}$ includes the residual that arises from non-linear effects in the PV inversion operation and from uncertainties related to the boundary conditions. The magnitude of $\mathbf{v}_{\mathrm{res}}$ is generally smaller compared to the magnitude of the other terms in (3.5)

when PPVI is applied to real atmospheric data. In the PUMA experiment, we found that locally the magnitude of $\mathbf{v}_{\text{res}}$ may be similar to the magnitude of $\mathbf{v}_{\text{TSd}}$ and $\mathbf{v}_{\text{div}}$. However, we did not find any evidence that this residual wind compromises the physical interpretation of our results (see section 6.2 for further discussion). The contribution from $\mathbf{v}_{\text{res}}$ in the operational model case of section 6.3 instead is always one orger of magnitude smaller compared to the other terms in the budget and therefore will be neglected.

We then combine the background term and the near-tropopause term into a modified near-tropopause term $\tilde{\mathbf{v}}_{\text{nTP}} = \mathbf{v}_{\text{nTP}} + \mathbf{v}_{\text{bg}}$ to finally obtain

$$\mathbf{v} \approx \tilde{\mathbf{v}}_{\text{nTP}} + \mathbf{v}_{\text{Td}} + \mathbf{v}_{\text{div}} \ . \tag{3.6}$$

Substituting this partitioning into the definition of T_{C} yields

$$T_C \approx T_{\text{nTP}} + T_{\text{TSd}} + T_{\text{div}} \ , \tag{3.7}$$

and, upon filtering

$$\langle T_C \rangle \approx \langle T_{\text{nTP}} \rangle + \langle T_{\text{TSd}} \rangle + \langle T_{\text{div}} \rangle \ , \tag{3.8}$$

where the approximation arises from neglecting $\mathbf{v}_{\text{res}}$. In the following sections, the three terms on the right hand side will be referred to as the near-tropopause, the tropospheric-deep, and the divergent term, respectively" (Ghinassi et al., 2019).

Chapter 4

Diagnosing large amplitude Rossby wave packets

In this chapter we will present the application of our diagnostic based on LWA to identify RWPs first in an idealised simulation (barotropic model on the sphere, section 4.1.1) and then using meteorological data (section 4.2). The LWA diagnostics will also be compared to the envelope of meridional wind (which is an established and widely used diagnostic for RWPs) to compare their performances in identifying wave packets in different flow situations. Several of the results presented in sections 4.1.1 and 4.2 have been published in Ghinassi et al. (2018). Section 4.1.2 discusses the application of the LWA flux to diagnose the group propagation of wave packets in the barotropic model. Finally, in section 4.3 a climatology of RWPs based on filtered LWA is presented. The computation of the RWPs climatology based on filtered LWA has been performed with the help of my colleague Georgios Fragkoulidis. In the following sections we use the zonal filter based on wavelet to remove the phase information from LWA.

4.1 Barotropic model on the sphere

We first test the performance of the LWA diagnostics (including the LWA flux) using a barotropic model on the sphere. The barotropic model allows us to simulate RWPs in different setups, while at the same time we avoid the complications related to real

three-dimensional flows. To relate our diagnostic to a more established one, we will compare the LWA diagnostic with the envelope of the meridional wind of Zimin et al. (2003), where we retain zonal wavenumbers 2 to 9, ranging from the synoptic to the planetary scale.

4.1.1 Rossby wave packets decay[1]

"We consider the barotropic vorticity equation on a sphere

$$\frac{\partial \zeta}{\partial t} = -J(\psi, f + \zeta) - \nu \nabla^4 \zeta \ , \tag{4.1}$$

where relative vorticity ζ is defined as in (2.24), J denotes the Jacobian, and ψ is the streamfunction; the latter is related to the horizontal wind through

$$(u, v) = \left(-\frac{1}{a} \frac{\partial \psi}{\partial \phi}, \frac{1}{a \cos \phi} \frac{\partial \psi}{\partial \lambda} \right) \ . \tag{4.2}$$

The last term in (4.1) represents hyperdiffusion, which dissipates enstrophy near the smallest resolved scale. The coefficient for hyperviscosity is set to $\nu = 10^{15}$ m^4 s^{-1}. Equation (4.1) is discretized with a standard spectral transform method (with triangular truncation at T89) on a regular latitude-longitude grid with a resolution of 2°. The equation is integrated in time for 5 days using a leapfrog scheme (with a time step $\Delta t = 900$ s) including a Robert-Asselin-Williams filter (Williams, 2011) to control the growth of the computational mode.

As initial condition we specify a purely zonal background flow $u_b(\phi)$ with a wavelike perturbation superimposed. For the background flow we follow Held and Phillips (1987) and set

$$u(\phi, t = 0) = A \cos \phi - B \cos^3 \phi + C \sin^2 \phi \cos^6 \phi \tag{4.3}$$

with $A = 25$, $B = 30$ and $C = 300$ m s^{-1}.

This flow resembles the climatology observed in the upper troposphere, with westerly subtropical jets at $\phi = \pm 30°$ and easterlies in the deep tropics"(Ghinassi et al., 2018). The wind profile $u(\phi, t = 0)$ and the PV profile at the initial time for the

[1]The parts of this section in quotation marks have been published in Ghinassi et al. (2018).

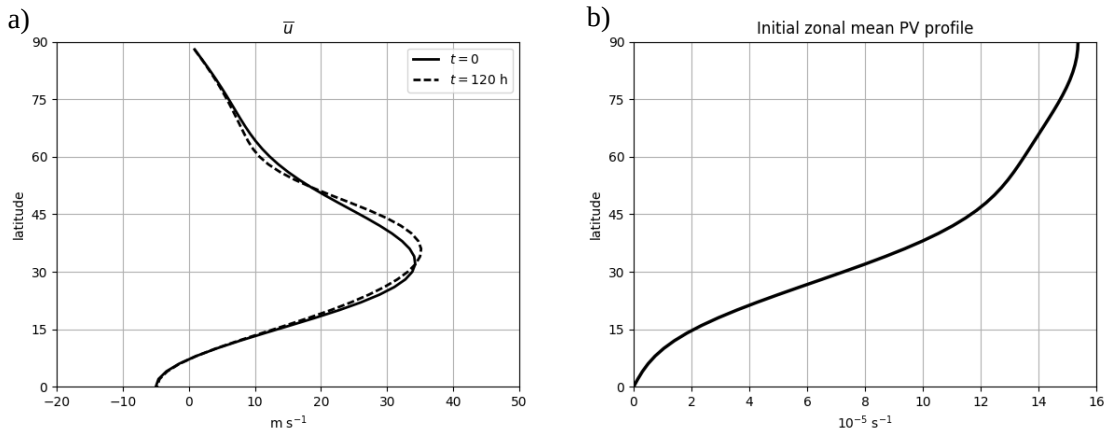

Figure 4.1: a) zonal mean zonal wind a the initial time (zonally symmetric $u(\phi, t = 0)$ as defined in (4.3), solid black line) and at the end of the simulation after 120 h (dashed black line). b) Initial zonally symmetric PV profile.

Northern Hemisphere are shown in Figure 4.1. "Onto this background flow we superimpose two localized wave packets, which are specified in terms of a relative vorticity perturbation as

$$\zeta_p(\lambda, \phi) = \zeta_0 \cos\phi \, e^{-\left[\frac{(\phi-\phi_0)}{\sigma_\phi}\right]^2} [L_1(\lambda) + L_2(\lambda)] \ , \tag{4.4}$$

$$L_1(\lambda) = e^{-\left[\frac{(\lambda-\lambda_1)}{\sigma_\lambda}\right]^2} \cos(s_1\lambda) \ , \tag{4.5}$$

$$L_2(\lambda) = e^{-\left[\frac{(\lambda-\lambda_2)}{\sigma_\lambda}\right]^2} \cos(s_2\lambda) \ , \tag{4.6}$$

with $s_1 = 6$, $s_2 = 9$, $\zeta_0 = 8 \times 10^{-5}$ s^{-1}, $\phi_0 = \pi/4$, $\lambda_1 = \pi/3$, $\lambda_2 = 2\pi/3$, $\sigma_\phi = 10°$, and $\sigma_\lambda = 30°$. Note that we deliberately initialize two RWPs with different carrier wavenumbers ($s_1 \neq s_2$) in order to test the performance of our filtering algorithm.

Figure 4.2 shows absolute vorticity at the initial time as well as at the end of the integration. It can be seen that by the end of the integration both wave packets have evolved into a very nonlinear stage with overturning contours of absolute vorticity and cut-off formation on the poleward side of the jet.

During the simulation, we compute the barotropic variants of both the filtered LWA and the envelope of meridional wind diagnostic for the Northern Hemisphere from snapshots of PV and the meridional wind field, respectively" (Ghinassi et al., 2018). LWA and filtered LWA computed from the PV field at the initial time are shown in

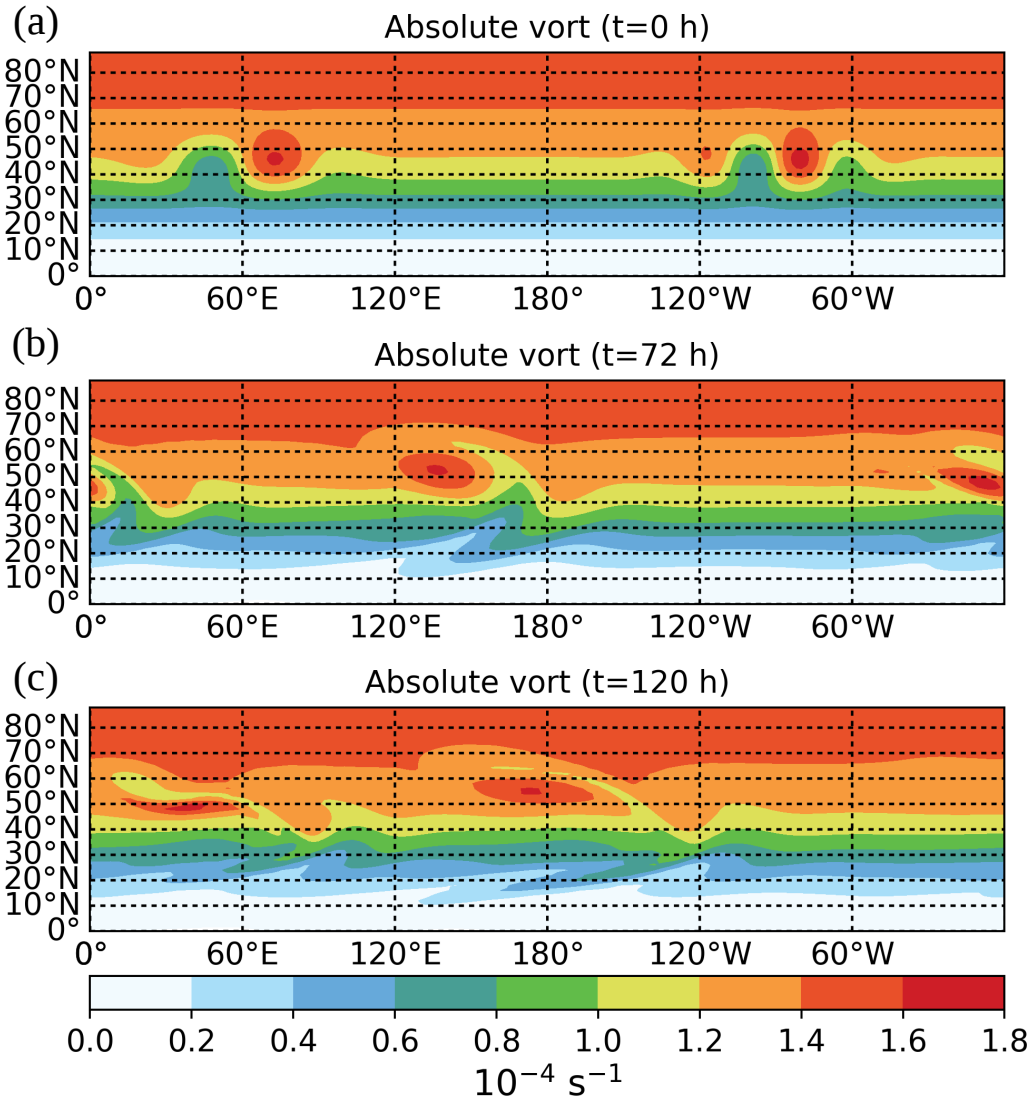

Figure 4.2: Absolute vorticity (colour shading, in 10^{-4} s^{-1}) in the barotropic model simulation, (a) at initial time, (b) after 3 days and (c) 6 days of integration.

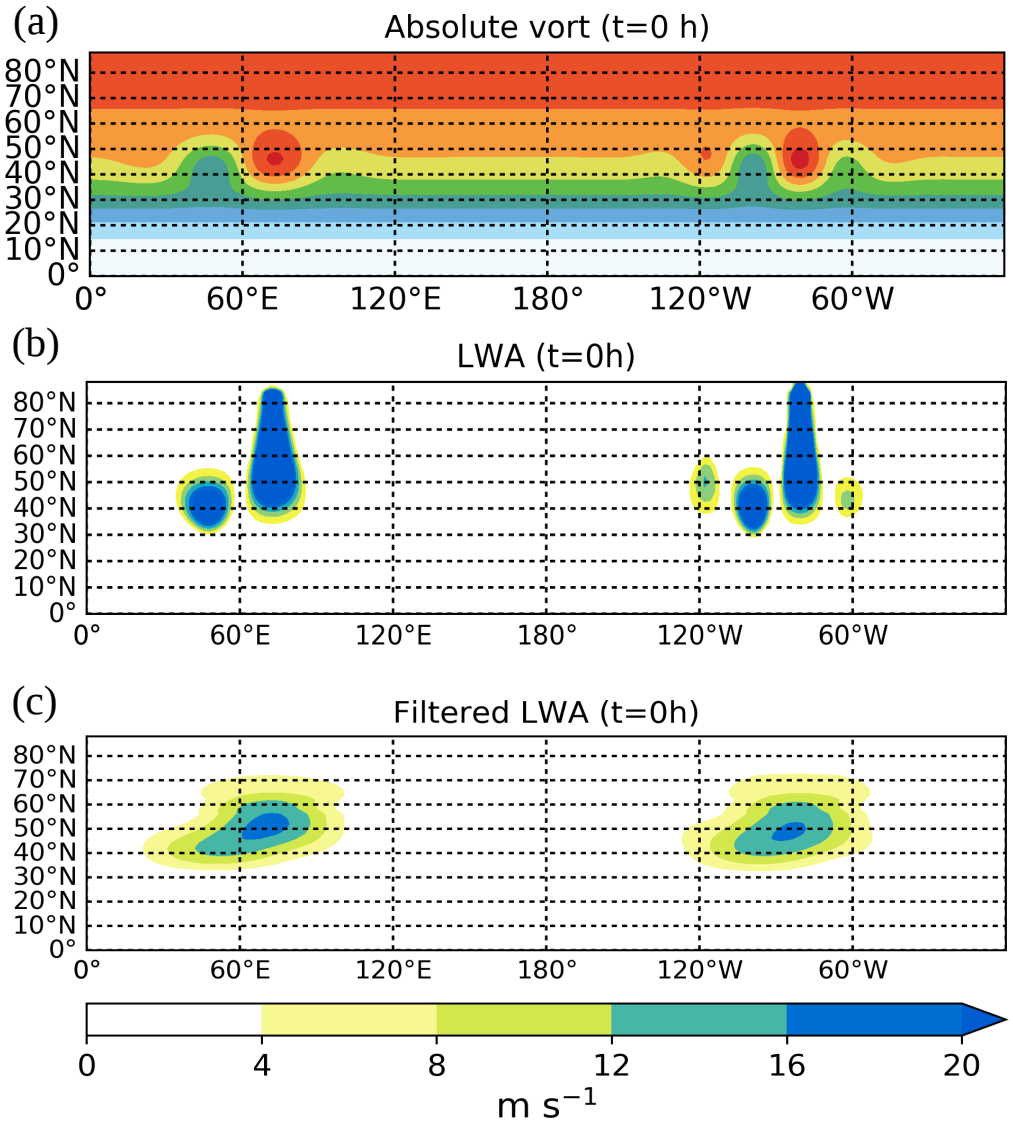

Figure 4.3: Absolute vorticity at initial time (a), LWA (b) and filtered LWA (c) computed from (a).

Figure 4.3. It can be seen ho LWA identifies the series of PV anomalies embedded in the two RWPs and how the filtering along the zonal direction removes the phase information. Note how in both RWPs the LWA associated with the two troughs where the positive PV anomalies are larger extends almost to the North Pole. This non-local effect is related to the fact that the high values of PV in the troughs are associated to a northern latitude (in the Northern Hemisphere); the values of PV in the troughs located at 45° N are indeed comparable to the one found at latitudes poleward of 70° N. This non-local effect is a known property of LWA (see Solomon and Nakamura 2012 and Huang and Nakamura 2016, especially their Fig. 4) and it is related to its partly-Lagrangian nature. It can be observed how the filtering partially removes such non-local effect. At high latitudes the meridional wind is almost zero and this yields $s_d \approx 1$, which implies that the witdh of the Hann window is almost the entire latitude circle, according to (3.4). Therefore after convolution this high, non-local values of LWA are "smeared out" and filtered LWA quantifies the RWPs amplitude only in the latitudinal band where the PV (and therefore v) anomalies associated with the wave packets are found.

"Figure 4.4 shows the evolution of these two diagnostics throughout the simulation. During the first 24 h, both diagnostics provide a similar picture, with both RWPs being clearly visible. This is not surprising, as during this stage the structure of the two wave packets in terms of PV or meridional wind resembles the form of equation (2.15). At later times, the amplitude of the envelope diagnostic decreases very noticeably, while the amplitude of the LWA diagnostic does not. After 120 h, the two RWPs have almost disappeared from the plot in terms of the envelope, while they are still clearly visible in the LWA diagnostic. Interestingly, the decay of the envelope starts to become noticeable roughly at the time when wave breaking sets in with overturning contours of absolute vorticity. It transpires that the LWA diagnostic is much more appropriate for tracking RWPs well into their nonlinear stage than the envelope diagnostic. We also observed that although there is a significant reduction in the magnitude of the meridional wind towards the end of the simulation, it is still large enough to provide a reasonable estimate of the local dominant wavenumber in our algorithm for the phase average.

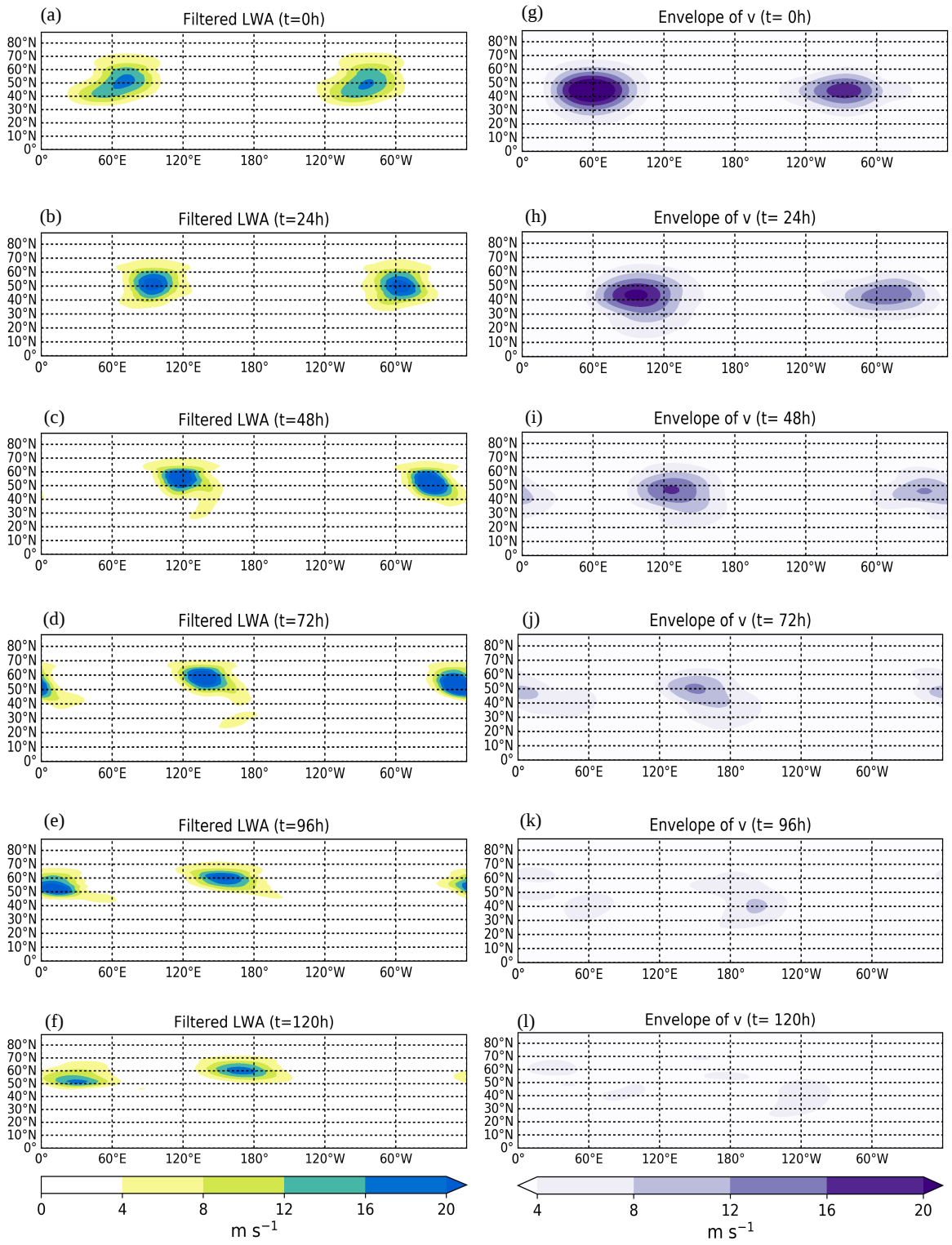

Figure 4.4: Evolution of filtered LWA (left column, colour shading, in m s^{-1}) and the envelope of the meridional wind (right column, colour shading, in m s^{-1}) in the barotropic model simulation, shown as snapshots every 24h. From Ghinassi et al. (2018) © Copyright 2018 American Meteorological Society (AMS). Used with permission.

The two diagnostics also disagree in terms of location and amplitude of the detected RWPs, rather slightly during the early stage, but more strongly during the late (nonlinear) stage. Generally there is a tendency for the LWA diagnostic to put the RWPs at a slightly more northern latitude compared to the envelope diagnostic. This is related to the fact that some of the non-local effects previously discussed are still present in the filtered LWA. Regarding the zonal direction, the LWA diagnostic puts the detected RWPs at a more western position during the late stage in comparison with the envelope diagnostic. Comparison with Fig. 4.2 indicates, that the western part of each RWP is characterized by closed vortex-like structures (or "PV cutoffs") during the late stage. Apparently, it is these vortex-like structures which LWA is particularly sensitive to; on the other hand, the envelope diagnostic tends to focus on the downstream wave-breaking portion of the RWP, which produces a larger signal in terms of the meridional wind than the upstream vortex" (Ghinassi et al., 2018). Presumably the meridional wind v in these highly nonlinear vortex structures is very weak due to the destructive interference created by different PV anomalies of different signs (see Fig. 4.2c). "The upstream vortex, in turn, tends to decouple from the RWP in the sense that it slows down and starts to move with the phase velocity (which is slower than the group velocity)" (Ghinassi et al., 2018).

Then, to investigate the evolution of filtered LWA and the envelope of v we computed the time series of the globally averaged fields, which are shown in 4.5. It can be seen how the globally averaged filtered LWA monotonically decreases, in contrast with the envelope, whose behaviour appear oscillatory. Filtered LWA in fact slowly decreases with time due to the combined effect of momentum transfer back to the mean flow (a slight increase of $\overline{u}$ in the jet core is observed during the simulation, as shown in Fig. 4.1a) and hyperdiffusion damping LWA. The envelope of v instead increases during the early stages of the simulation even though only dissipative processes are present in our simulation. This amplitude increase shown by the envelope of v seems unphysical and it is likely related to the fact that v is not a conserved quantity even in a purely conservative flow, as discussed previously.

Lastly, we investigate on the difference between finite amplitude local wave activity and the small amplitude variant. We computed small amplitude wave activity on the

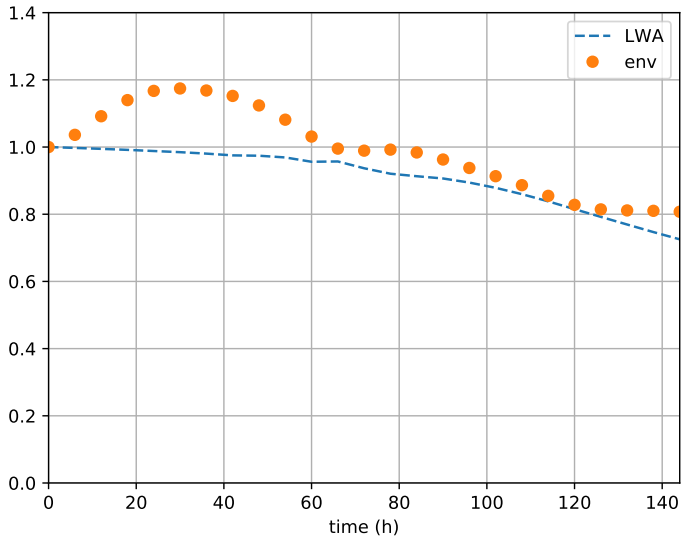

Figure 4.5: Time evolution of globally averaged filtered LWA and envelope of v from the barotropic simulation. Both filtered LWA and envelope are normalised with their respective globally averaged value at $t = 0$.

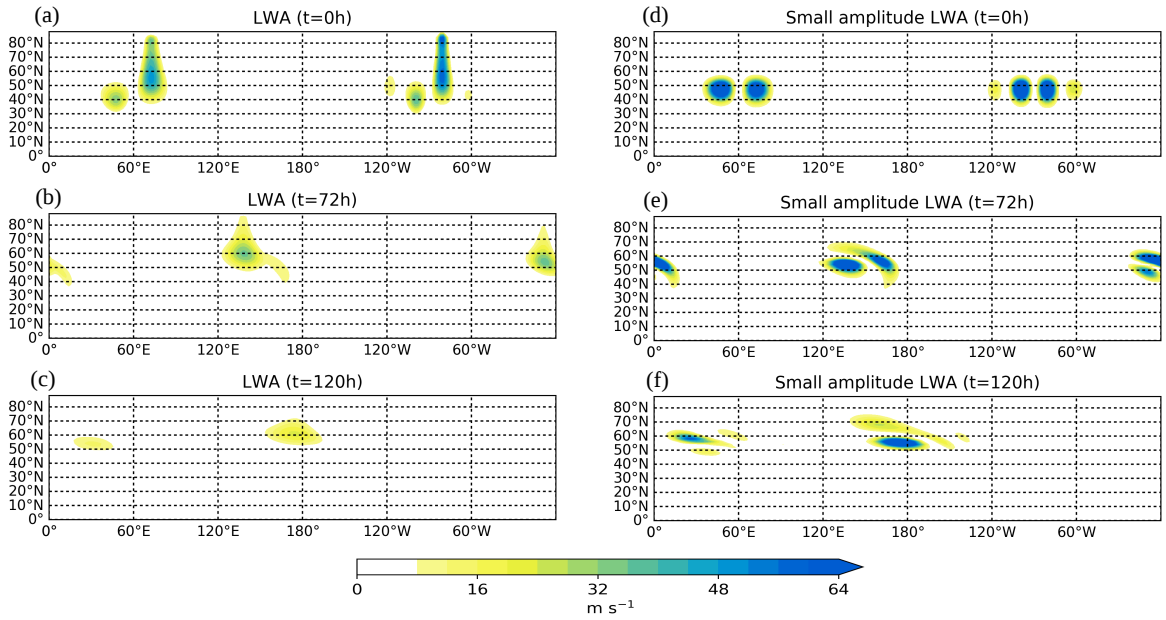

Figure 4.6: Evolution of finite amplitude LWA (left column, colour shading, in m s^{-1}) and small amplitude LWA (right column, colour shading, in m s^{-1}) in the barotropic model simulation, computed from snapshots of the PV field at the initial time, after 72 and 120 hours into the simulation.

sphere as the local contribution to the expression (2.25) and setting the meridional PV gradient in the parameter γ as the time-zonal mean, in order to have $\gamma > 0$ throughout the whole duration of our simulation. The comparison between the unfiltered LWA and its small amplitude variant at the initial time and after 72 and 120 hours of the barotropic model simulation is shown in Figure 4.6. At the initial time it can be seen how the non-local effect of LWA in the PV troughs is not present in the small amplitude LWA. The latter in fact is defined in terms of Eulerian quantities and faithfully captures the location in physical space of the two RWPs. As the simulation proceeds the small amplitude LWA tends to become more and more filamentary, truly resembling the phase structure of the RWPs as they initiate wave breaking. By the end of the simulation LWA on the other hand exhibits a more compact structure with a tendency to merge the different phases observed in the PV field in each wave packet in a whole structure (see PV field in Figure 4.2). In addition, the magnitude of LWA decreases with time, as expected, whereas the magnitude of its small amplitude variant remains suspiciously large even during the decay phase of the wave packets. This is of course due to the fact that as the simulation proceeds the small amplitude assumption is certainly violated. This again evidence the necessity of a finite amplitude measure of wave activity to identify RWPs especially in the real atmosphere, where their structure is often nonlinear and their amplitude is large.

4.1.2 LWA flux in the barotropic model

In this section we provide an illustrative example of the use of the LWA flux to diagnose the group propagation of RWPs in the barotropic model. The application of the finite amplitude LWA flux in the barotropic model is a new result of this thesis and provides some additional insight on the propagation of idealised RWPs. At first we computed the LWA flux $\mathbf{F}$ and its divergence according to (2.59) and (2.58) for the barotropic simulation described in the previous section (4.1.1). The purpose of this analysis is to diagnose the group velocity of transient, zonally propagating RWPs. In the barotropic model, the divergence of the LWA flux $\mathbf{F}$ is approximately equal to minus the conservative term T_{C}, provided that the effect of dissipation on $Q(\phi)$ is weak, as it is the case in our RWPs decay simulation (the impact of non-conservative processes

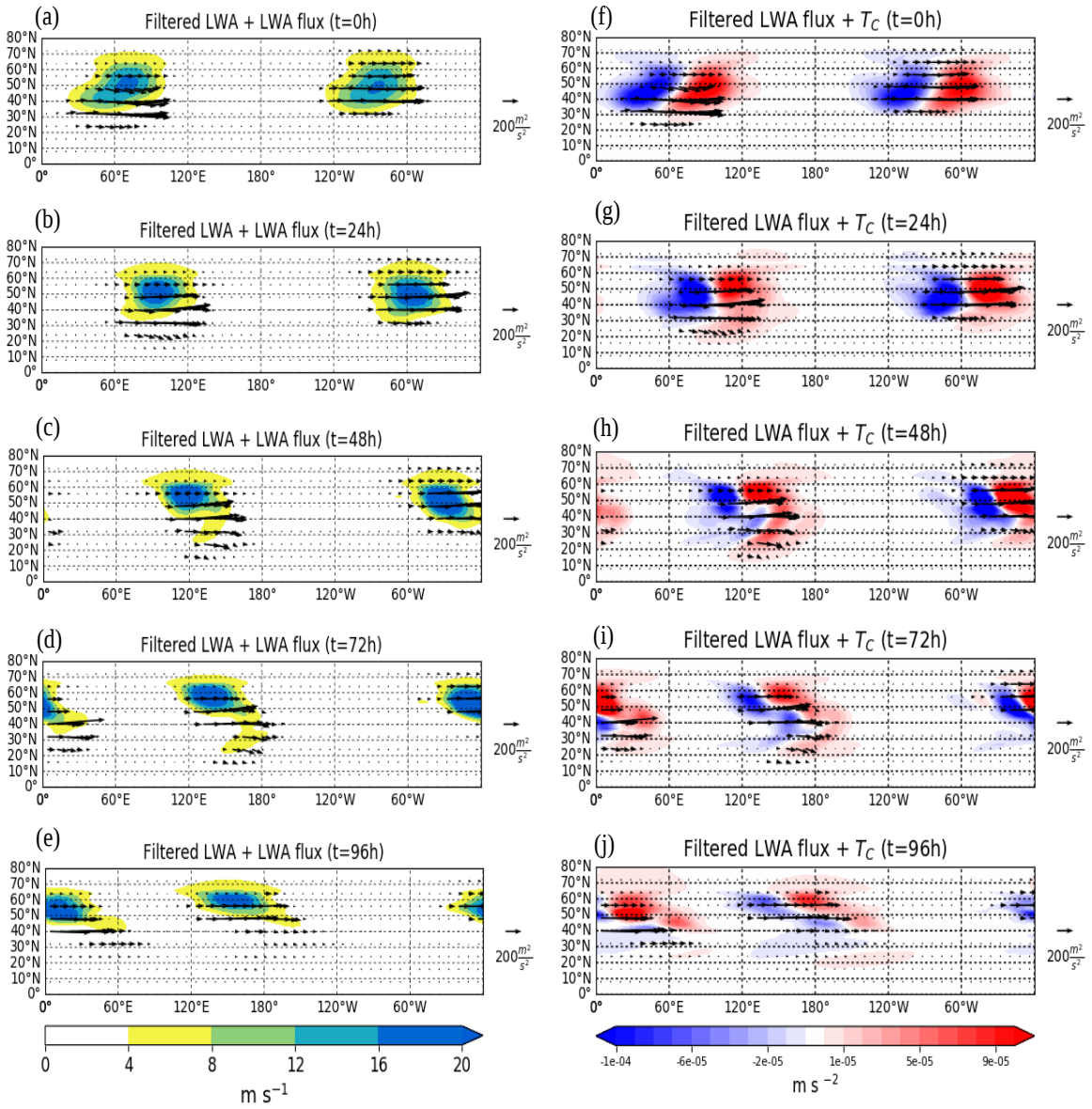

Figure 4.7: Left panels: evolution of filtered LWA (colour shading, in m s^{-1}) and filtered LWA flux **F** (arrows, in m^2 s^{-2}) as defined in equation (2.59) in the barotropic model simulation. Right panels: filtered conservative term T_C (colour shading, in m s^{-2}) and filtered LWA flux for the same simulation. Quantities are showed from the initial time until 96h, every 24h.

on $Q(\phi)$ will be quantified in chapter 6). Here we compute the eddy-free reference state u_{REF} inverting the PV distribution $Q(\phi)$ rather than using (2.62), assuming that the numerical error associated to the PV inversion is smaller compared to the one committed in the computation of A. In any case we checked that u_{REF} computed with the two methods described above only differs by a small value, as Figure 4.8 shows.

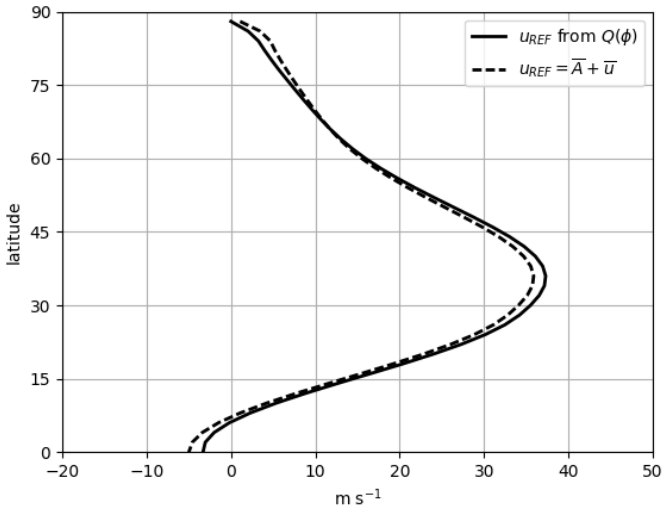

Figure 4.8: Comparison of u_{REF} obtained inverting the PV distribution $Q(\phi)$ (solid black line) and computed according to (2.62) (dashed black line) at the initial time of the simulation.

Then, we removed the phase information from the horizontal components of $\mathbf{F}$ and T_{C} by applying the zonal filter based on wavelets (see section 3.2.2). Since we are interested in the use of the LWA flux for a purely diagnostic purpose we neglect any issue related to the non-linearity of this wavelet filter (see discussion in section 3.3.2). Filtered LWA, the filtered LWA flux $\mathbf{F}$ and T_{C} for the first 4 days of simulation are shown in Figure 4.7. Recall that according to the relation (2.58) we have that the filtered conservative term $T_{\mathrm{C}} \approx -\nabla \cdot \mathbf{F}$, where the approximation arises due to nonconservative flow and the wavelet filter used. It can be seen as $\mathbf{F}$ clearly identifies the eastward propagation of the two RWPs throughout the simulation. T_{C} at this time evidences the LWA export from the rear of the two wave packets, where T_{C} is negative, to the front, where T_{C} is positive, consistent with their eastward motion. After 48 hours the *first RWP* located at 120° E manifests the signs of wavebreaking, with its structure becaming "bow shaped". The *second RWP*, located between 60° W and 0° at t=48 h, on the other hand shows a more coherent propagation, and manifests wavebreaking about 24 hours later than the first RWPs. At initial time and after 24 hours $\mathbf{F}$ and T_{C} show that in the second RWP the propagation is almost entirely eastward and oriented in a purely zonal direction. The magnitude of $\mathbf{F}$ is larger in the center of the RWPs and decreases to smaller

values at its edges. During the same time interval **F** and T_C instead show that the southern flank of the first wave packet travels with a larger group velocity compared to the second and the associated wave activity appears to propagate equatorward. As dicussed above, this wave packet is the first to encounter wave breaking. The behaviour observed in our simulation agrees with what found in the analysis of a Rossby wave breaking event by Wolf and Wirth (2017). The authors observed how wavebreaking caused by a decaying RWP tends to occur in region of strong convergence of wave activity flux (the authors used the formulation of Takaya and Nakamura (2001)) and when the associated wave activity propagates towards regions of smaller PV gradient. This is indeed the case also in our simulation, where the largest meridional PV gradient is found in correspondence of jet maximum (located at 30° N) and it decreases to smaller values to the North and to the South of this latitude (see Fig. 4.1). After 96 hours the decay of the both wave packets is almost complete and their eastward propagation has slowed down considerably, as evidence by the consistent reduction in the magnitude of **F** compared to earlier times. Note how LWA and the LWA flux can be computed even when the eddy PV field is highly nonlinear and nonmonotonic along the meridional (see PV field in Fig 4.2). The finite amplitude LWA flux formulation therefore certainly represents an improvement compared to the LWA flux formulation of Takaya and Nakamura (2001) which assumes the small amplitude of the waves.

We now investigate the utility of the LWA flux in diagnosing the propagation of both transient and stationary eddies but at a planetary scale. In a similar setup of the one of Yang and Hoskins (1996) we consider the forced-dissipative barotropic vorticity equation:

$$\frac{\partial q}{\partial t} = -J(\psi, q) + F - \alpha(q - q_0) - \nu\nabla^4(q - q_0) \ , \tag{4.7}$$

where F is pseudo-orographic forcing specified as

$$F(\lambda, \phi, t) = -\nabla \cdot [\mathbf{v} f \, \Gamma(\lambda, \phi)] \ , \tag{4.8}$$

where $\mathbf{v}$ is the horizontal wind and $\Gamma(\lambda, \phi)$ is a non-dimensional Gaussian function. The Gaussian has a maximum height of 0.15, is centred at (45° N, 45° E), and has a circular base with a standard deviation of 15°. The third term on the right hand side

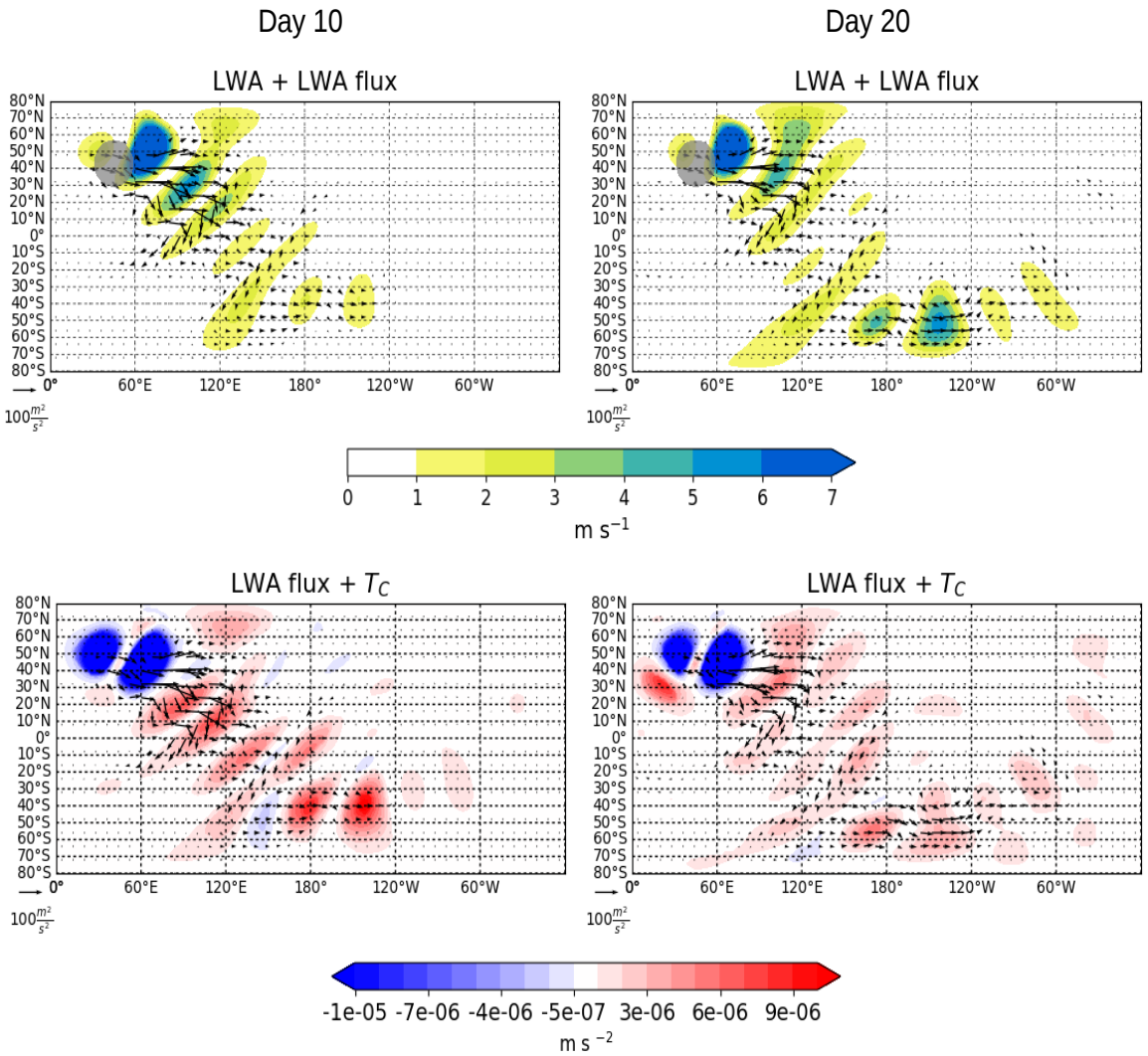

Figure 4.9: LWA (colour shading, in m s^{-1}) and LWA flux $\mathbf{F}$ as defined in equation (2.59) (arrows, in m^2 s^{-2}), and conservative term T_C (colour shading, in m s^{-2}) and LWA flux in the barotropic model simulation with pseudo-orographic forcing. Quantities are showed after 10 days (left panels) and 20 days (right panels) of simulation. The grey shading in the top panels represents the region in which the amplitude of the pseudo-orographic forcing exceeds 0.075.

of (4.7) represents linear relaxation of PV towards the zonally symmetric initial state q_0, such that q_0 is a solution of (4.7) at the initial time. In our simulation we chose $\alpha = (15\,\text{days})^{-1}$. The fourth term on the right hand side of (4.7) is hyperdiffusion, in which $\nu = 10^{15}$ m^4 s^{-1}.

As initial condition we consider an atmosphere in solid body rotation with the

Earth, in which the initial zonal wind is

$$u_0(\phi) = 20 \cos\phi \ \text{m s}^{-1} \ . \tag{4.9}$$

The interaction of the flow with the orography gives rise to an initial transient Rossby wave train that is radiated away from the source along a great circle until a stationary state is reached Hoskins and Karoly (1981). Since in this experiment we are interested in planetary scale Rossby waves which propagate also in the meridional direction across the equator we will not apply the zonal filter to LWA. Figure 4.9 shows LWA as well as its flux and $T_{\rm C}$ after 10 and 20 days of simulation. At day 10 a stationary state has yet to be reached, and LWA and its flux clearly identify a Rossby wave train which propagates downstream of the forcing in a southeasterly direction. The zonal wind is westerly all over the globe and this allow the Rossby waves to propagate in the Southern Hemisphere across the equator. At day 20 the system has almost reached a stationary state and Rossby wave activity is distributed all over the globe. During the entire simulation $T_{\rm C}$ clearly evidence that LWA is radiated away from the source region (where $T_{\rm C}$ is negative) towards South East and the group propagation of the Rossby wave train is clearly identified by the direction of $\mathbf{F}$. An advantage of the finite amplitude LWA flux is that it can be used to diagnose both the transient and stationary propagation of the eddies from any snapshot of the flow. This is an improvement compared to the flux proposed by Plumb (1985), which is valid only for small amplitude, stationary eddies or by Plumb (1986), which is valid for transient eddies but requires the knowledge of a slowly varying background state (usually set as the time average). Due to the total LWA flux $\mathbf{F}$ given by the sum of the advective flux and the stationary E-P flux (see eq. (2.59)) it would be also easy to partition $\mathbf{F}$ in its two components to distinguish the contribution from transient eddies from the stationary ones, however this task remains open for future work.

4.2 Diagnosing Rossby wave packets in reanalysis data[1]

"We now apply our LWA diagnostic to an episode that occurred in April 2011. This episode was characterized by RWP propagation and Rossby wave breaking. It is of particular interest since it was associated with a "forecast bust" for the majority of the operational forecast models, showing a huge drop in the medium range forecast skill over Europe (Rodwell et al., 2013). The authors associated this poor performance to the misrepresentation of moist convective processes over North America a few days earlier, and this error was subsequently communicated downstream embedded in a RWP. Data are retrieved from the ERA-Interim reanalyses (Dee et al., 2011) with a horizontal resolution of $2 \times 2^\circ$ on equispaced pressure levels ranging from 1000 to 100 hPa. First we analyze a snapshot from the observed episode. Figure 4.10 shows PV, LWA, and filtered LWA on the 320 K isentrope (which intersects the tropopause in the mid-latitudes). The PV field shows a series of troughs and ridges over North America, indicating the presence of an RWP. In addition, there is strong Rossby wave activity over Europe and over Asia. The field of LWA (Fig. 4.10b) shows overall larger values in regions where the PV field is more disturbed. For instance, the troughs and ridges over North America in Fig. 4.10a coincide with increased values of LWA in Fig. 4.10b. Over Europe and eastern Asia, the PV field (Fig. 4.10a) shows very large amplitude perturbations, which are mirrored by large values of LWA in Fig. 4.10b. Finally, the filtered LWA field in Fig. 4.10c discounts the phase information altogether — as desired. Instead, it shows a much smoother field with three relative maxima, one over eastern Asia, one over North America and one over Europe. The regions surrounding these three maxima are regions of strong waviness and represent the RWPs identified by the LWA diagnostic and we will refer to them respectively as "Pacific RWP" (marked with "A" in Fig. 4.10c), "Atlantic RWP", (marked with "B" in Fig. 4.10c) and "Eurasian RWP" (marked with "C" in Fig. 4.10c)" (Ghinassi et al., 2018).

We also computed the analogous quasi-geostrophic LWA field of Fig. 4.10b using (2.64). QGPV, QG LWA and filtered QG LWA are shown in Figure 4.11. In the

[1]The parts of this section in quotation marks have been published in Ghinassi et al. (2018).

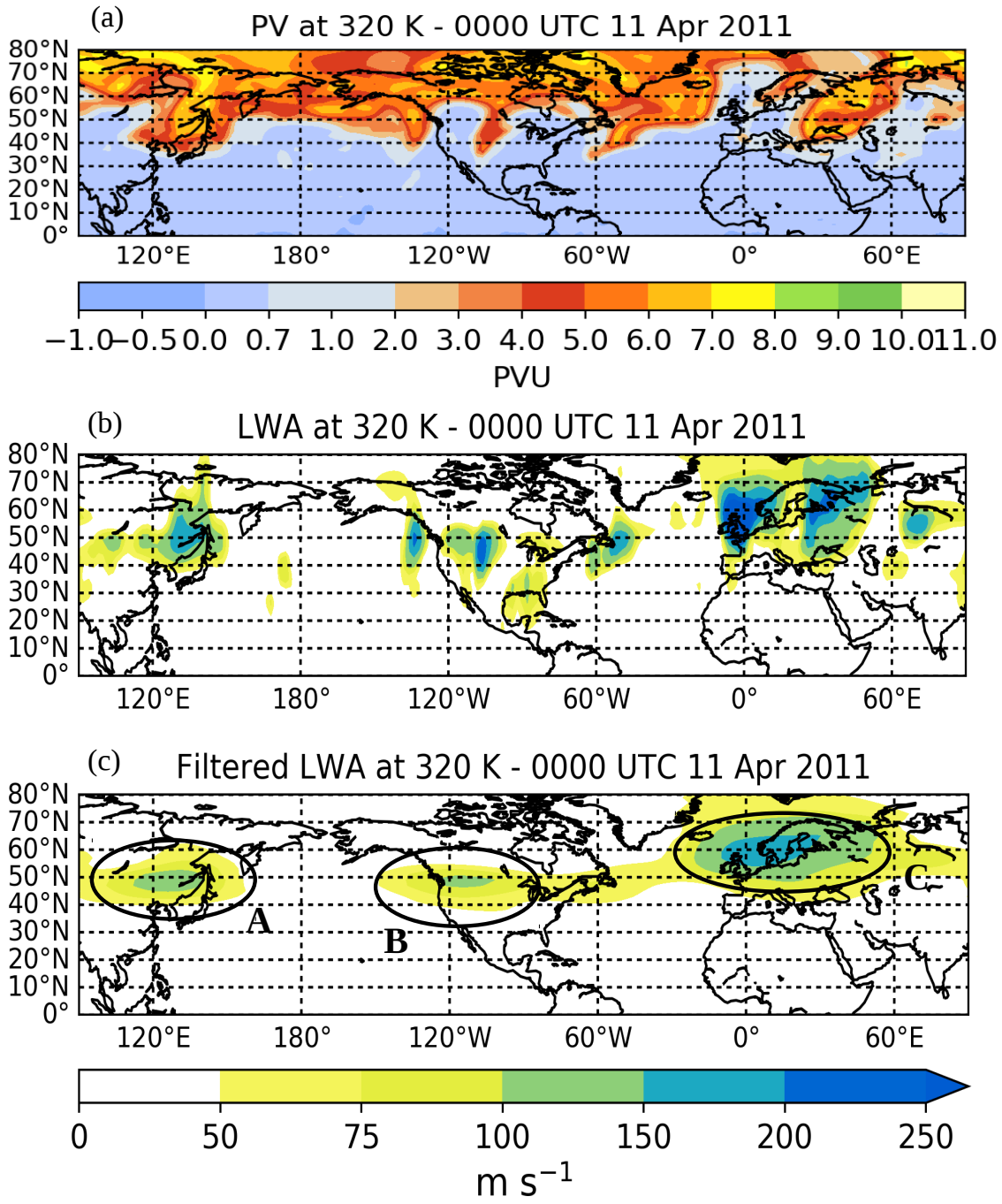

Figure 4.10: Analysis of the flow on 0000 UTC 11 April 2011 on the 320 K isentrope. (a) Potential vorticity (colour shading, in PVU, 1 PVU $\equiv 10^{-6}$ K m^2 s^{-1} kg^{-1}), (b) local finite amplitude wave activity LWA (colour shading, in m s^{-1}), and (c) filtered LWA (colour, shading in m s^{-1}). The colour bar for both (b) and (c) is provided below panel (c). From Ghinassi et al. (2018) © Copyright 2018 American Meteorological Society (AMS). Used with permission.

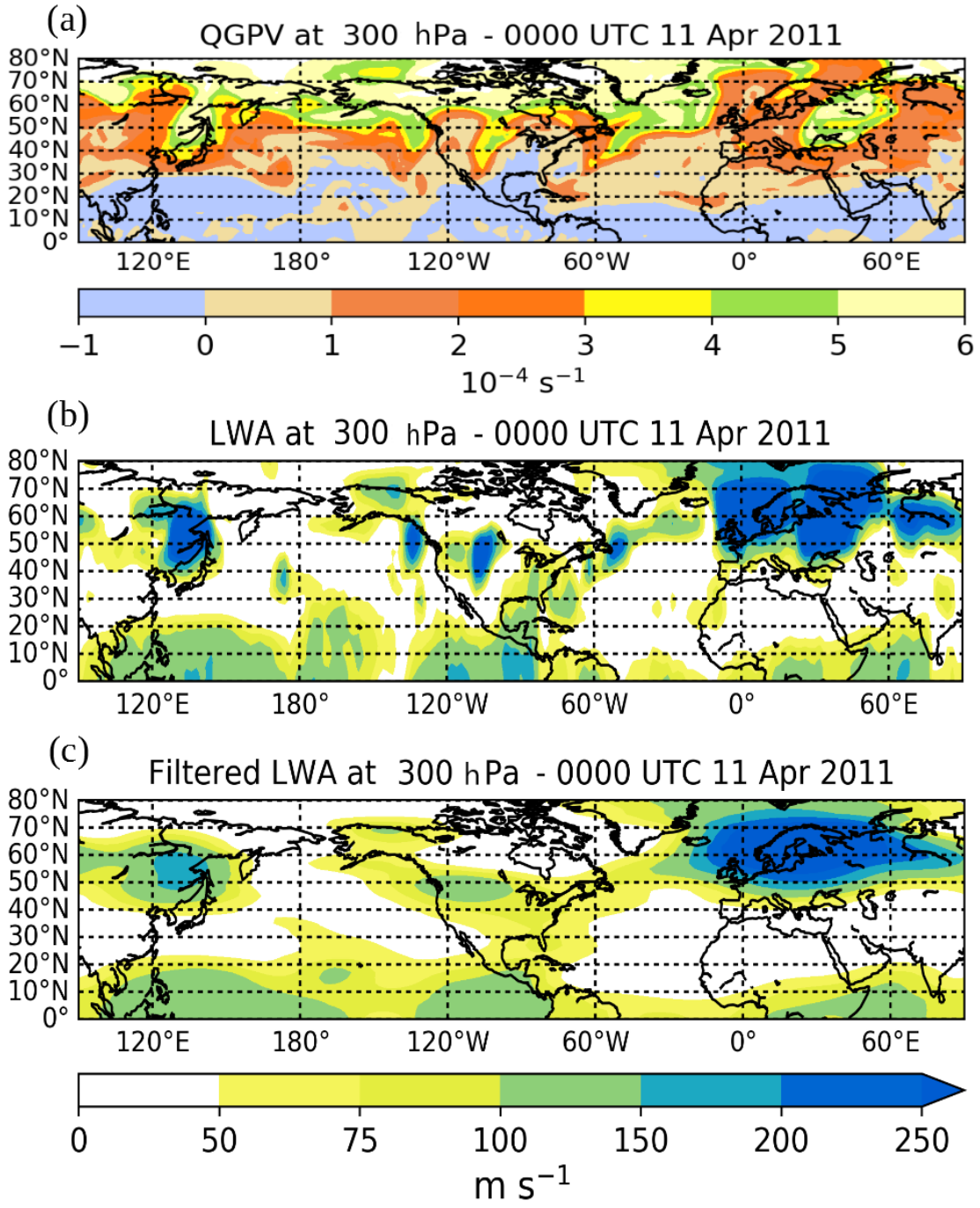

Figure 4.11: Analysis of the flow on 0000 UTC 11 April 2011 at 300 hPa. (a) Quasi-geostrophic potential vorticity (colour shading, in m s^{-1}), (b) quasi-geosprophic local finite amplitude wave activity LWA (colour shading, in m s^{-1}), and (c) filtered QG LWA (colour shading, in m s^{-1}). The colour bar for both (b) and (c) is provided below panel (c).

extratropical upper troposphere (at 300 hPa) quasi-geostrophic LWA shows a fairly similar picture over North America, although some differences in the magnitude and location of LWA arise over northern Europe and Scandinavia (compare Fig 4.10b with Fig 4.11b). In particular, in the large amplitude ridge aver the north-western portion of the Atlantic (located approximately at 65° N, 0° E), QGPV (Fig 4.11a) does not show a sharp PV gradient as the Ertel PV at the tropopause (Fig 4.10a). This is likely to be related to the fact that at the tropopause the sudden change in the static stability violates the QG assumption. It is in the tropics that the major differences between the QG and PE LWA are evident, with a longitudinally extended band of QG LWA extending from the equator up to 25° N (4.11b). This spurious QG LWA is related to the reversal of the QGPV observed in the subtropics, where potential temperature largely deviates from its global reference value $\tilde{\theta}$ in the definition of QGPV (2.27). This spurious region of QG LWA prevents one from identifying RWPs which originate from or migrate into this region. Presumably the time-zonal mean of such quasi-geostrophic LWA is related the spurious region of quasi-geostrophic FAWA found in the climatology of Nakamura and Solomon (2010), which, on the other hand, is not found anymore in the primitive equation analysis of Nakamura and Solomon (2011). It is not surprising that the quasi-geostrophic approximation does not provide a realistic picture of the tropical dynamics, and this provides an explicit example of the advantage of LWA in the primitive equations/isentropic coordinates compared to its quasi-geostrophic formulation.

"Next we consider a sequence of consecutive maps following the stage of Fig. 4.10. This is done in order to follow the evolution of the three RWPs identified above. For reference, Fig. 4.12 presents the corresponding sequence of PV maps. Apparently, PV shows large-amplitude waviness throughout the episode. The large trough that was initially located over the east coast of Asia develops a very strong and highly nonlinear low-PV anomaly on its downstream side (i.e., over North-East Siberia). In addition, there is a sequence of troughs emanating from the North American continent. Typically, these troughs tend to become thinner as time proceeds, leading to anticyclonic wave breaking and cut-off formation reminiscent of "life-cycle 1" of Thorncroft et al. (1993). Eventually this sequence of events lead to blocking, i.e., a quasi-stationary low-PV

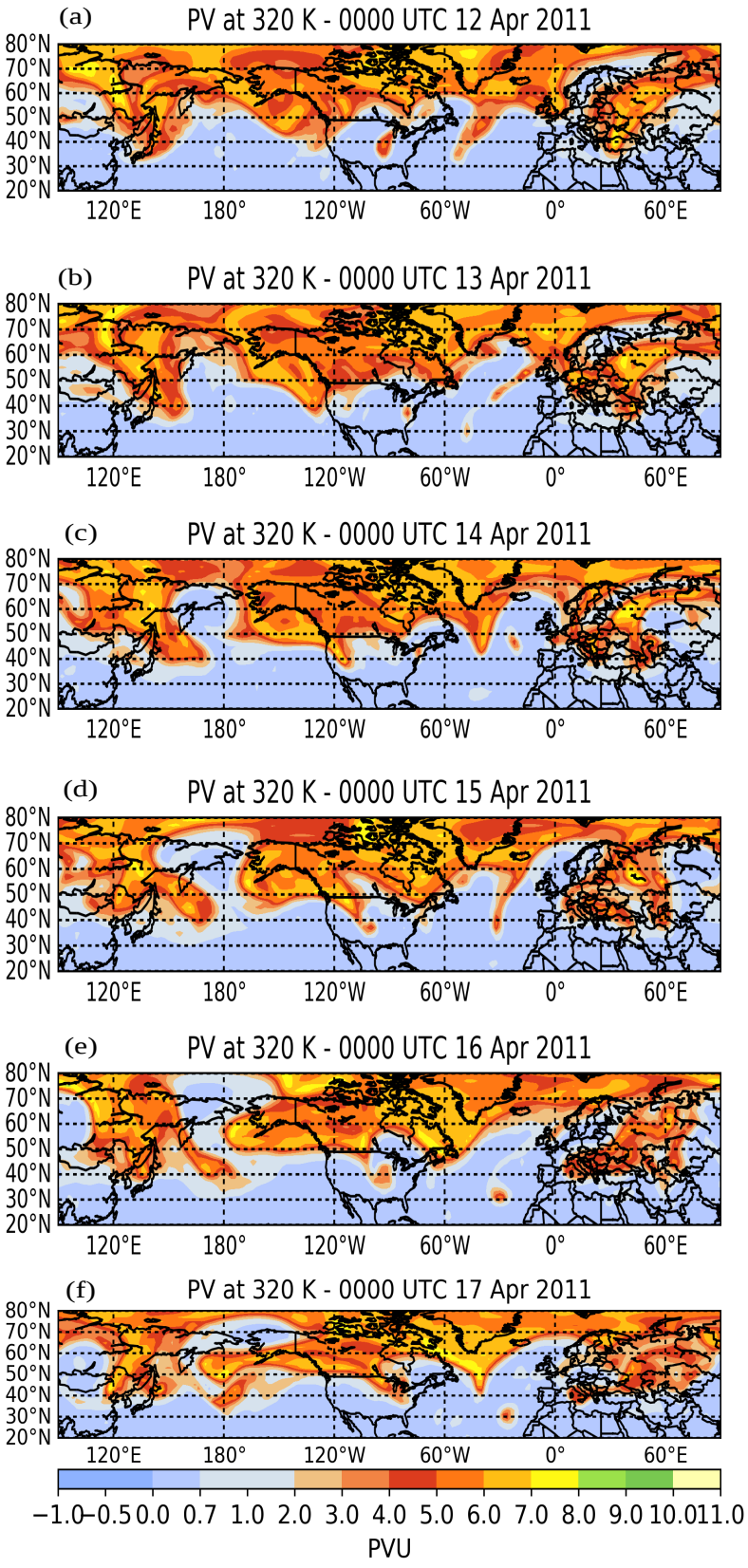

Figure 4.12: Evolution of PV (colour shading, in PVU) on the 320 K isentrope starting on 0000 UTC 12 April 2011 for the following 5 days period. From Ghinassi et al. (2018) © Copyright 2018 American Meteorological Society (AMS). Used with permission.

anomaly over the eastern Atlantic and Europe. Apparently it was the onset of this blocked flow situation that was missed in practically all numerical weather predictions models during this episode (Rodwell et al., 2013).

The left column of Fig. 4.13 shows the filtered LWA for the same episode. The field is dominated by three areas with high values which identifies our three RWPs (the labeling of RWPs follows from Fig. 4.10c). The Pacific RWP originates from the east Asian trough mentioned earlier. It shows a steady eastward progression by about 60° in 5 days, which means an eastward group velocity of 12° per day. By contrast, the Atlantic RWP has a somewhat larger eastward group velocity initially, but around April 14 it seems to slow down and merge with the Eurasian RWP. The latter is quasi-stationary during the first half of the episode, but later starts to move eastward across the dateline. Interestingly, the Atlantic RWP turns retrograde (i.e. starts to propagate westward) during the end of the displayed episode.

To set our new diagnostic into perspective, we also computed the envelope of the meridional wind field according to Zimin et al. (2003). In our application, we combine this technique with a zonal filter restricting the range of zonal wavenumber to the interval 2–9 (as in the barotropic model simulation), allowing us to focus on synoptic-to-planetary scales. Note that the envelope of meridional wind is Eulerian in both latitude and longitude, in contrast with LWA, which instead is partly Lagrangian in the meridional coordinate. During most of the episode, this envelope diagnostic (right column of Fig 4.13) provides a similar representation of the Pacific RWP as our LWA diagnostic (left column of Fig 4.13). However, by April 17 the Pacific RWP turns rather weak in terms of its envelope, while it remains strong in terms of filtered LWA. This large difference occurs at a time when the flow was characterized by highly nonlinear overturning of PV isolines, which cannot be described any longer as a "wave" to whatever approximation. Turning to the Atlantic RWP, the picture obtained from the envelope diagnostic is much less coherent in comparison with the LWA diagnostic. In particular, the envelope diagnostic does not show a clear eastward progression of the RWP during the first half of the episode. Note that this Atlantic RWP, too, was characterized by highly nonlinear behaviour such as trough elongation and cut-off formation. Finally, the Eurasian RWP can be found in the envelope diagnostic, but again

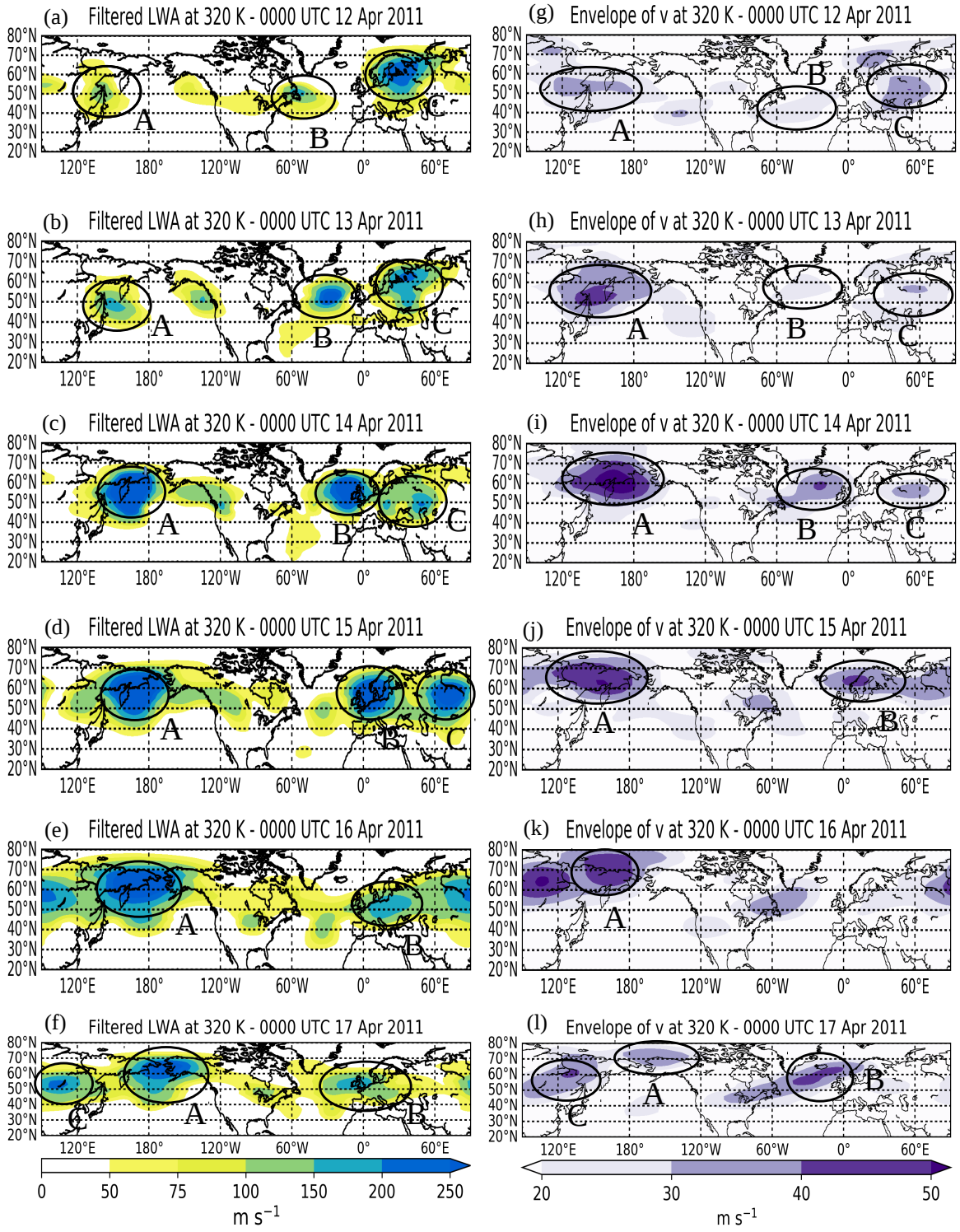

Figure 4.13: Evolution of filtered LWA (left column, colour shading, in m s^{-1}) and envelope of meridional wind (right column, colour shading, in m s^{-1}) on the 320 K isentrope starting on the 0000 UTC 12 April 2011 for the following 5 days period. From Ghinassi et al. (2018) © Copyright 2018 American Meteorological Society (AMS). Used with permission.

its evolution appears somewhat less coherent in comparison with the LWA diagnostic.

The results from this comparison suggest that the LWA diagnostic is more appropriate to follow the evolution of RWPs — in particular during their nonlinear stage. Obviously, this result was to be expected, because LWA is, by design, able to deal with highly nonlinear flows. By contrast, the framework of envelope reconstruction implicitly assumes that the perturbation is wavelike (see eq. (2.15)), but this property is lost as the perturbation reaches its nonlinear stage with overturning PV contours and wave breaking"(Ghinassi et al., 2018).

4.3 A climatology of Rossby wave packets based on filtered LWA

The filtered LWA diagnostic has been applied to the Era-Interim reanalysis spanning the period starting from January 1979 until December 2016. The aim is to investigate on the longitudinal structure of finite amplitude wave activity in the climatology. A climatology of the zonally averaged FAWA was presented in Nakamura and Solomon (2011) (see Fig. 2.6 in section 2.5.3). Filtered LWA is computed globally with the same horizontal, vertical and temporal resolution of section 4.2 and then averaged over each month of the considered period. Subsequently the seasonal climatologies are presented for winter (December, January, February), spring (March, April, May), summer (June, July, August) and autumn (September, October, November). Even though we computed filtered LWA globally we want to stress our attention on the Northern Hemisphere. Therefore for each season we selected an isentropic surface which intersects the tropopause approximately in the midlatitudes of Northern Hemisphere and lies above the ground over the whole domain at each time step. For this reason we chose the 325 K isentropic surface for winter, spring and autumn and 335 K for summer. The resulting seasonally averaged filtered LWA fields are shown in Figure 4.14.

During the winter months (Fig. 4.14a) filtered LWA shows two pronounced maxima over the West Pacific and over the North Atlantic. The North Atlantic maximum appears stronger in magnitude compared to the Pacific one and extends well above

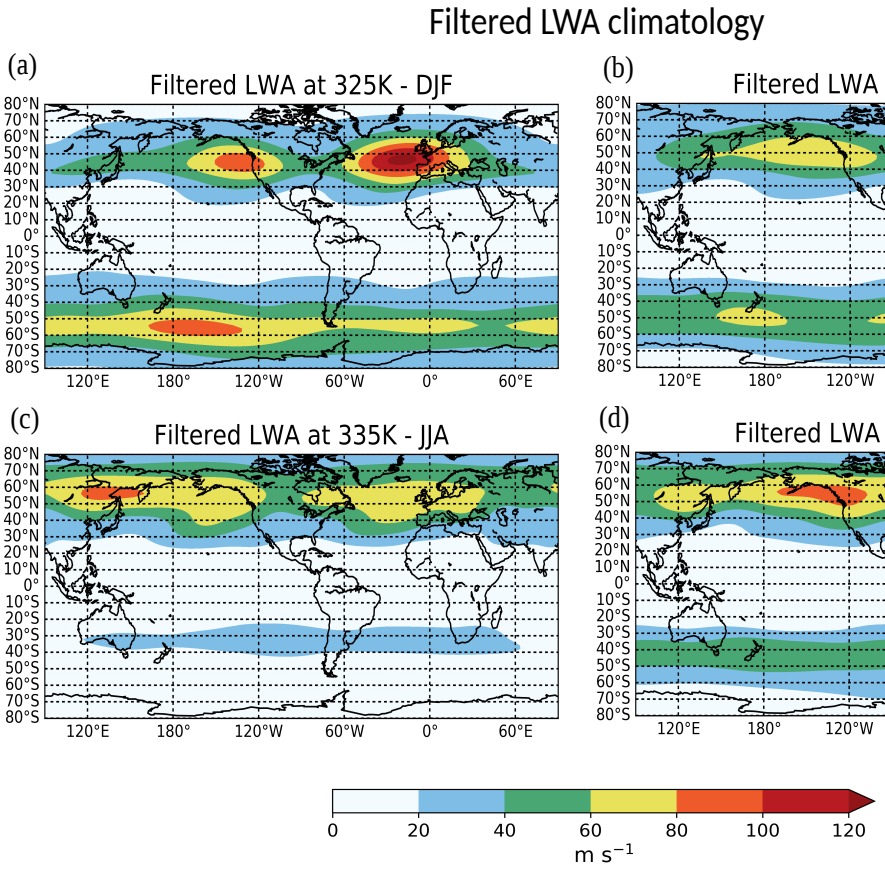

Figure 4.14: Filtered LWA climatology based on the Era Interim database (1979-2016). a) winter season (December, January, February, DJF) on the 325 K isentrope, b) spring (March, April, May, MAM) on the 325 K isentrope, c) summer (June, July, August, JJA) on the 335 K isentrope and d) autumn (September, October, November, SON) on the 325 K isentrope.

Western Europe. These localised maxima are arguably associated with the high transient Rossby wave activity found in the extratropics in the FAWA analysis of Nakamura and Solomon (2011) and Methven (2013). During spring the magnitude of filtered LWA slightly decreases compared to the winter season over the storm track regions and the maxima of wave activity are found over a broader longitudinally extended area. This is particularly evident in the Pacific storm track. During autumn the longitudinal extension of filtered LWA further increases and the two storm tracks are almost merged in a single structure in the upper troposphere. This could suggest that during Autumn some RWPs which originate over the East Pacific find favourable conditions to propagate across North America and the North Atlantic and eventually decay over Europe.

The RWPs behaviour observed in autumn emerged also in the analysis of Grazzini and Vitart (2015). In summer, the magnitude of wave activity is weaker compared to the other seasons, in particular over the North Atlantic. This fact is consistent with a weaker transient eddy activity observed during the Northern Hemisphere Summer (Nakamura and Solomon, 2011; Shaw et al., 2016). In addition, in autumn and spring another region of high wave activity is found over Eastern Asia at the beginning of the Pacific storm track, while the Rossby wave activity over this region appears weaker during winter and spring. During winter, spring and autumn, the longitudinal loca-

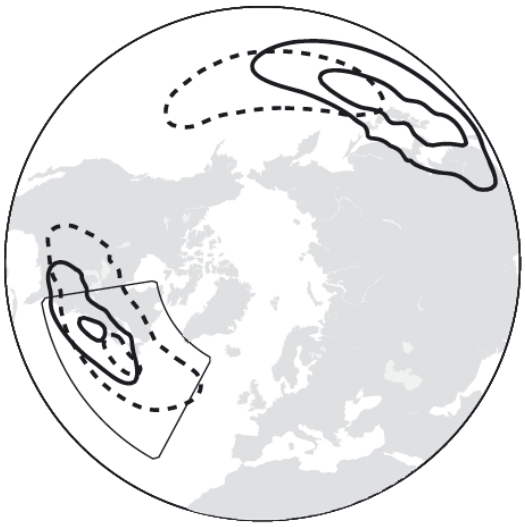

Figure 4.15: Polar stereographic view of the low level baroclinicity defined as the maximum Eady growth rate (solid contours, displaying values of 0.5 and 0.6 day^{-1}) and heat flux (dashed contours, displaying values of 10 and 20 K m s^{-1}) averaged over the 1957–2002 DJF winters. Figure taken from Ambaum and Novak (2014).

tion of the storm tracks identified in terms of filtered LWA appears to extend more downstream (to the East) when compared to other widely used metrics to identify the storm tracks. These metrics include the low level baroclinicity or the eddy heat fluxes (Hoskins and Valdes (1990); Ambaum and Novak (2014), see Fig. 4.15), or the EKE (Chang et al. (2002); Shaw et al. (2016), see Fig. 4.16b).

A possible explanation is related to the fact that metrics such as the eddy heat fluxes usually maximise during the baroclinic growth phase of the eddies (Simmons and Hoskins, 1978; Ambaum and Novak, 2014) and therefore their location matches fairly well with the regions of high baroclinicity found in the upstream part of the

Northern Hemisphere storm tracks (see Fig. 4.15). Interestingly, these regions of high baroclinicity are also regions of frequent intense RWPs occurrence according to the analysis of Souders et al. (2014), as can be observed from the comparison of Figure 4.16a with the map of baroclinicity in Figure 4.15. The analysis of Souders et al. (2014) however was computed extracting the envelope of the meridional wind according to Zimin et al. (2006)). Given that the envelope of v is particularly suitable to identify almost plane RWPs, the results of Souders et al. (2014) suggest that almost plane RWPs are often observed during their baroclinic growth phase. Filtered LWA on the other hand tends to manifest the largest values during the mature stage of the eddies (when their amplitude becomes large) and during wave breaking episodes, as we have shown in section 4.2. This may explain why large values of LWA are found also in the dowstream region of the Pacific and Atlantic storm tracks (in particular over the West coast of North America and western Europe), which are both regions of frequent wavebreaking occurrence (Martius et al., 2007; Masato et al., 2012).

The filtered LWA in the Southern Hemisphere has an annular, more longitudinally uniform structure over the four seasons. During the Southern Hemisphere winter (JJA) its magnitude is very low due to the fact that the 335 K isentropic level is well above the tropopause and therefore does not capture the transient Rossby wave activity associated with RWPs in the upper troposphere. There is a tendency for wave activity to be stronger over the Pacific compared to the Atlantic, in particular during the austral summer (DJF). Another important feature which emerges from the analysis of the Southern Hemisphere is that during the austral summer a considerable Rossby wave activity is found on the 325 K, whereas during the boreal summer wave activity is found very weak on such isentrope (not shown). During the Northern Hemisphere summer in fact the transient wave activity at the tropopause is found on higher isentropic levels (between 335 and 340 K). This could be related to the fact that that the dynamical tropopause height, which is associated with a strong isentropic PV gradient, during the respective summer seasons is lower in the Southern Hemisphere compared to the Northern one (see for example Fig.5 in Wilcox et al. (2012) and Fig. 2.6 in section 2.5.3 of this work for a climatology of the dynamical tropopause height based on PV). Overall, the magnitude of LWA exhibits a weaker inter-seasonal variability in the

Southern Hemisphere and this was also evident in the FAWA climatology of Nakamura and Solomon (2011) (see Fig. 2.6).

A final remark concerns the latitudinal position of the local Rossby wave activity maxima, which are found poleward in both hemispheres compared to Eulerian metrics such as EKE or the envelope of v (compare the Rossby wave activity of Fig. 4.14 with the RWPs analysis in which their amplitude is computed extracting the envelope of v or EKE of Fig. 4.16b), especially in autumn and summer. This is likely to be a manifestation of the nonlocal nature of LWA, as observed in the analysis of single RWPs in the previous sections.

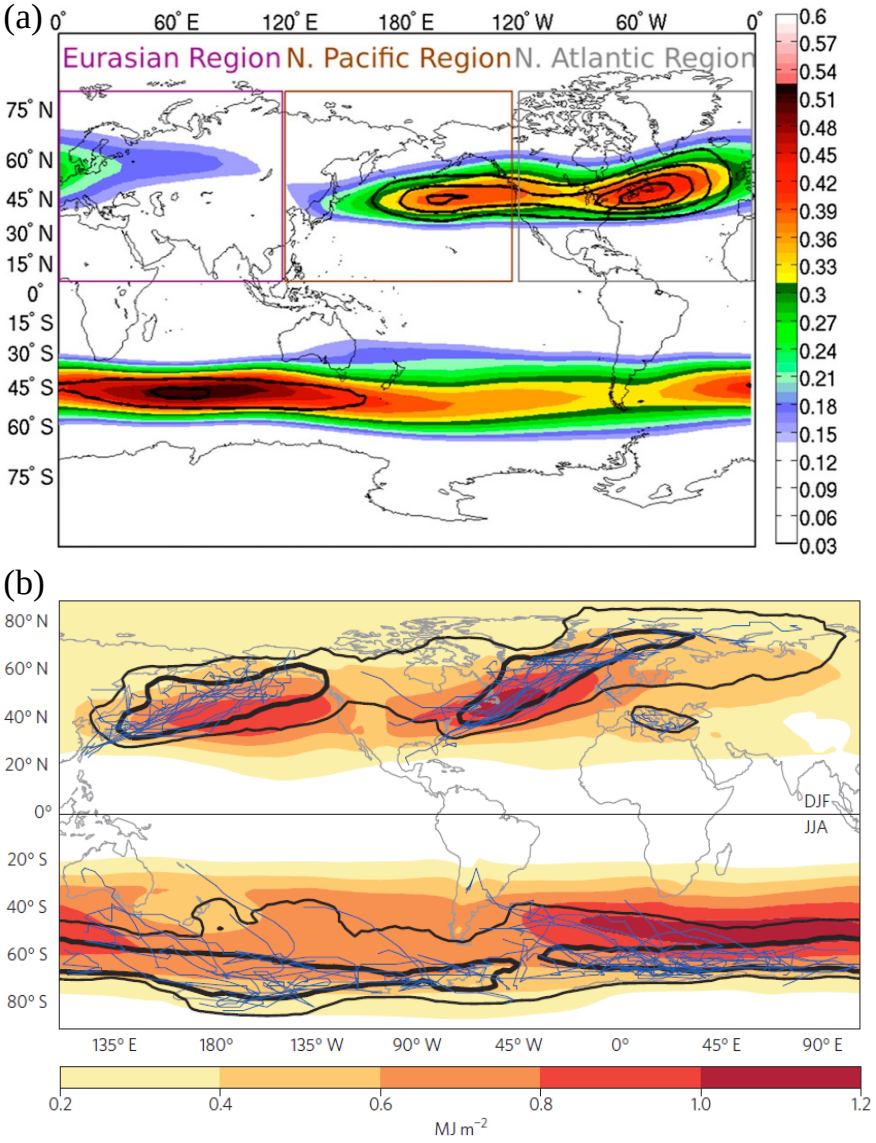

Figure 4.16: a): the probability of significant (shaded) and extreme (contoured every 0.5% beginning at 1.0% in black) RWPs (those exceeding the amplitude threshold of 30m s^{-1}) at any time. The RWP amplitude is computed extracting the envelope of meridional wind at 300 hPa with the method of Zimin et al. (2006). Figure taken from (Souders et al., 2014),c opyright 2018 American Meteorological Society (AMS). b): vertically averaged, ten-day high-pass filtered EKE from ERA-Interim reanalysis data set (coloured shading) for wintertime (December–February, DJF, in the Northern Hemisphere and June–August, JJA, in the Southern Hemisphere). From (Shaw et al., 2016), copyright 2016 Macmillan Publishers Limited. Used with permission.

Chapter 5

LWA diagnostic applied to upscale error growth[1]

This chapter is based on my contribution to the paper Baumgart et al. (2019). In this work, a diagnostic based on potential vorticity and the LWA diagnostic are are used to investigate upscale error growth in an ensemble simulation. The experiment setup, as well as the description of the diagnostics is provided in section 5.1. The PV based diagnostic retains the phase structure of the large scale flow, and therefore cannot be used to investigate the error growth from the synoptic up to the planetary scale, since it reaches saturation on the synoptic scale. For this reason the LWA diagnostic, which is phase independent, is used to identify the envelope of Rossby waves and permits the analysis of the error growth until it has reached the planetary scale. In section 5.2 the two diagnostics are applied first to two of the ensemble members of the simulation for one month to gain information on the spatial distribution of the error, to identify the regions in which the error growth is the largest. Finally, in section 5.3, spatial maps and time series of the error are produced by spatially averaging the PV error squared and the envelope error squared for all ensembles and all months.

[1]The parts of this chapter in quotation marks have been published in Baumgart et al. (2019).

5.1 Experimental setup and diagnostics definition

"For our experiment we use the icosahedral non-hydrostatic global forecasting model ICON of the German weather service (Zängl et al., 2015). The model was run with a horizontal resolution corresponding to about 40 km. Convection is parametrized using the stochastic Plant-Craig (PC) convection scheme (Plant and Craig, 2008). The PC scheme uses a random value of the convective mass flux, which is drawn from a quasi-equilibrium distribution that uses the ensemble mean mass flux given by a standard CAPE closure. For each ensemble member a different seed is used to generate the random draw, resulting in a different realization of convective variability (see Fig. 1 in Selz (2019) for illustration). At the initial time, this is the only difference between ensemble members, but as the simulations evolve, differences in the resolved flow will also lead to differences in the closure.

Twelve different cases are considered, one for each month from October 2016 to September 2017. These cases are initialized 12 h before the start of the month, using initial conditions from ECMWF. After a spin-up period of 12 h, we create an ensemble of five members by changing the random seed of the PC scheme. Initially, the only difference between these members thus lies in the convective scheme. All simulations are run for a duration of 31 days. Further information on the set up of the simulations are provided in Selz (2019)"(Baumgart et al., 2019).

For the further analysis of the error growth, data are interpolated from pressure to isentropic levels. Different isentropes are used for each case to account for the seasonal dependence of the tropopause location. For each case, the isentrope is chosen such that the tropopause is located at approximately 45°N. The choice of the different isentropic levels for each month is made on a "visual approach" of Figure 2 of the climatology of Liniger and Davies (2004). The selected isentropes are 315 K for Dec., Jan., and Feb., 320 K for Nov., Mar., and Apr., 325 K for Oct. and May, 330 K for Jun. and Sep., and 335 K for Jul. and Aug..

5.1.1 Potential enstrophy error

This section introduces the PV based diagnostics developed by my colleague Marlene Baumgart and her supervisor Michael Riemer. "This diagnostic quantifies the difference in terms of PV between the individual ensemble members, ΔP, defined as

$$\Delta P = P_{\mathrm{n}} - P_{\mathrm{m}} \ , \tag{5.1}$$

where P_{n} and P_{m} denote the PV of two different ensemble members n and m. Our ICON ensemble contains five members. It is thus possible to define the PV difference for ten different member pairs: member 2 – member 1, member 3 – member 1, member 3 – member 2, ...[1] In the following, we use the terminology 'error' for the difference between two members although, strictly speaking, none of the members describes the true evolution.

In order to have a positive definite metric, we consider the (potential) enstrophy error, $(\Delta P)^2/2$. The mean enstrophy error $\mathcal{P}$ is then defined a each time t as the spatial average of the enstrophy error over the midlatitudes of the Northern Hemisphere (30–80°N),

$$\mathcal{P} = \frac{1}{A} \int_A \frac{(\Delta P)^2}{2} dA \ , \tag{5.2}$$

where A is the area of integration, $dA = a^2 \cos\phi d\lambda d\phi$ is the area element in spherical coordinates, a denotes the radius of the Earth, λ is longitude, and ϕ is latitude. $\mathcal{P}$ is then averaged over the 12 cases and 10 member pairs within each case, which allows us to obtain reasonably robust statistics (a sample of 120), yielding $\overline{\mathcal{P}}$. The statistical uncertainty of $\overline{\mathcal{P}}$ associated with the month-to-month variability is estimated as the standard error for the 12 cases, i.e., $\sigma_{\mathrm{SD}}(\overline{\mathcal{P}}) = \sigma_{\mathrm{SD}}/\sqrt{12}$, where σ_{SD} denotes the standard deviation of the 12 cases (averaged over the 10 possible combinations)" (Baumgart et al., 2019).

[1] Note that for the further analysis of the error amplification it is not necessary to investigate the other possible combination of two members (e.g., one does not need to investigate member 1 – member 2 in addition to member 2 – member 1) as enstrophy and LWA are positive definite variables.

5.1.2 Rossby wave envelope error

The Rossby wave envelope is obtained by, first, quantifying Rossby "waviness" through Local Finite Amplitude Wave Activity (LWA) and then extracting the envelope through the zonal filter based on wavelets described in section 3.2.2. "In our work we decided to use the envelope of LWA instead of the more established envelope of the meridional wind based on Zimin et al. (2003). While both yield very similar results during the linear stage of a Rossby wave, the former was shown to be more appropriate in the case of finite amplitude waves (see discussion in chapter 4).

It is important to recall the fact that LWA is Eulerian in longitude and partly Lagrangian in latitude. This characteristic has to be kept in mind when comparing LWA-based diagnostics with our earlier-defined PV-based diagnostics, since the latter is fully Eulerian. In addition, the LWA-based diagnostic is nonlocal in the sense that (possibly remote) nonconservative processes affect the relation between ϕ and Q. This effect renders the relation $Q(\phi)$ dependent on time; however, this time-dependence turns out to be small in our ICON experiment, in the sense that $Q(\phi)$ varies by less than 10% within a one-month period and, by consequence, the difference between P and Q in the expression for LWA (2.65) is dominated by variations in P. Regarding our ensembles, it is appropriate to define a common $Q(\phi)$-relation for all members, and this is achieved by using the corresponding relation at initial time where all ensemble members are identical. This guarantees that LWA at one latitude ϕ is computed with respect to the same PV contour $Q(\phi)$ for each ensemble member. For computational efficiency, we use a spatial resolution of 2°x2° for the computation of LWA.

We use the filtered LWA to identify the Rossby wave envelope which we will call E throughout this section. Analogously to the PV diagnostic we consider the difference ΔE in the envelope between two ensemble members n and m,

$$\Delta E = E_{\mathrm{n}} - E_{\mathrm{m}} \, . \tag{5.3}$$

Note that ΔE (in contrast to E) is a signed variable and includes both amplitude and position errors of the envelope.

As for the enstrophy error, we consider the squared envelope error, $(\Delta E)^2/2$, which

is a positive definite quantity. From this, the mean squared envelope error is calculated at each time by a spatial average yielding

$$\mathcal{E} = \frac{1}{A}\int_A \frac{(\Delta E)^2}{2} dA \ , \tag{5.4}$$

where the integration area A extends over the midlatitudes of the Northern Hemisphere (20–80°N)" (Baumgart et al., 2019). In the spatial averaging of $(\Delta E)^2/2$ we extend the southern boundary up to 20°N to include some of the Q contours which partially lies South of 30°N. "Finally, $\mathcal{E}$ is averaged over the 12 cases and 10 member pairs within each case yielding $\overline{\mathcal{E}}$. The statistical uncertainty of $\overline{\mathcal{E}}$ associated with the month-to-month variability is estimated as the standard error for the 12 cases, i.e., $\sigma_{\mathrm{SD}}(\overline{\mathcal{E}}) = \sigma_{\mathrm{SD}}/\sqrt{12}$ as for the mean enstrophy error" (Baumgart et al., 2019).

5.2 Illustrative case study

"The October ensemble is used to illustrate the spatial patterns of our error-growth diagnostics. This section starts with a discussion of the differences between the first two members. Recall that the difference between two ensemble members is here referred to as error. The contributions from the individual processes to error growth are then discussed in terms of their spatial pattern. Finally, the error growth in the two-member ensemble is compared to that in the five-member ensemble.

The PV and envelope error (ΔP and ΔE) derived from the first two members of the October ensemble at selected time steps are shown in Figures 5.1, and 5.2. At day 1, the PV error occurs near the grid scale and exhibits appreciable values (0.1 PVU) only in very localized regions (not shown here). These regions are spatially correlated with regions of precipitation. By day 5 (Fig 5.1a), the PV error amplifies by an order of magnitude and starts to develop spatially more coherent patterns. Differences in the position of the dynamical tropopause become apparent by day 5. During these first five days the envelope error is very small in magnitude (not shown).

Between day 5 and 10, the PV error further amplifies (Fig. 5.1a and b) and the previously localized PV errors change to a larger-scale and more coherent error pattern

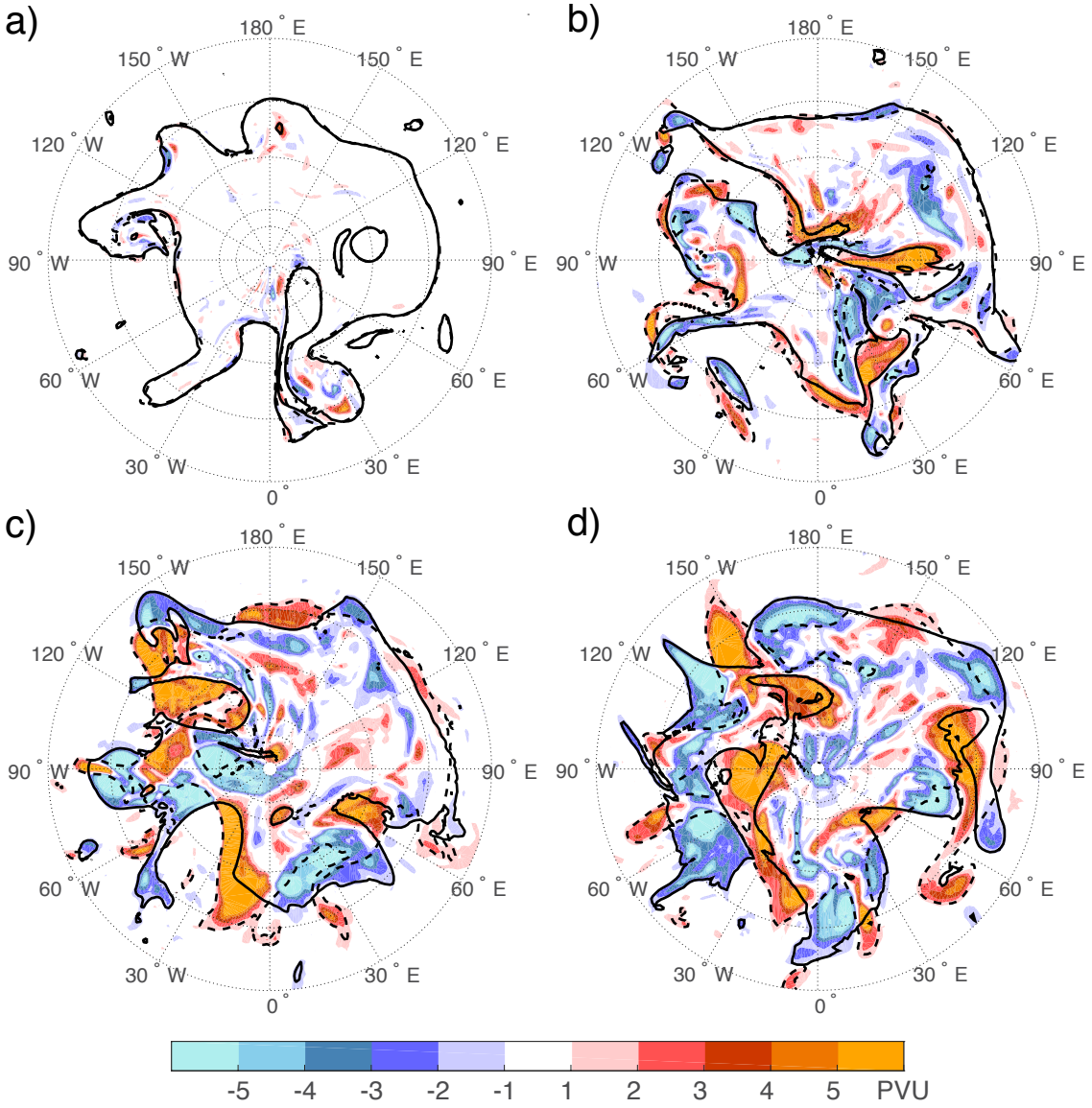

Figure 5.1: PV error derived from the first two members ($\Delta P = P_2 - P_1$) of the October ensemble at a) day 5, b) day 10, c) day 15, and d) day 20. Black contours denote the dynamical tropopause of member 1 (solid) and member 2 (dashed). Plot produced by Marlene Baumgart. From Baumgart et al. (2019) © Copyright 2019 American Meteorological Society (AMS). Used with permission.

that maximizes in regions where the tropopause is highly distorted. By day 10, the PV error projects more strongly on the planetary scale and now the error at the Rossby wave envelope scale becomes appreciable (Fig. 5.2g). The envelope error manifests as a dipole around $120 - 150°$W, suggesting that the error consists in a shift of the envelope. The second envelope-error maximum is a monopole located around $30 - 60°$E,

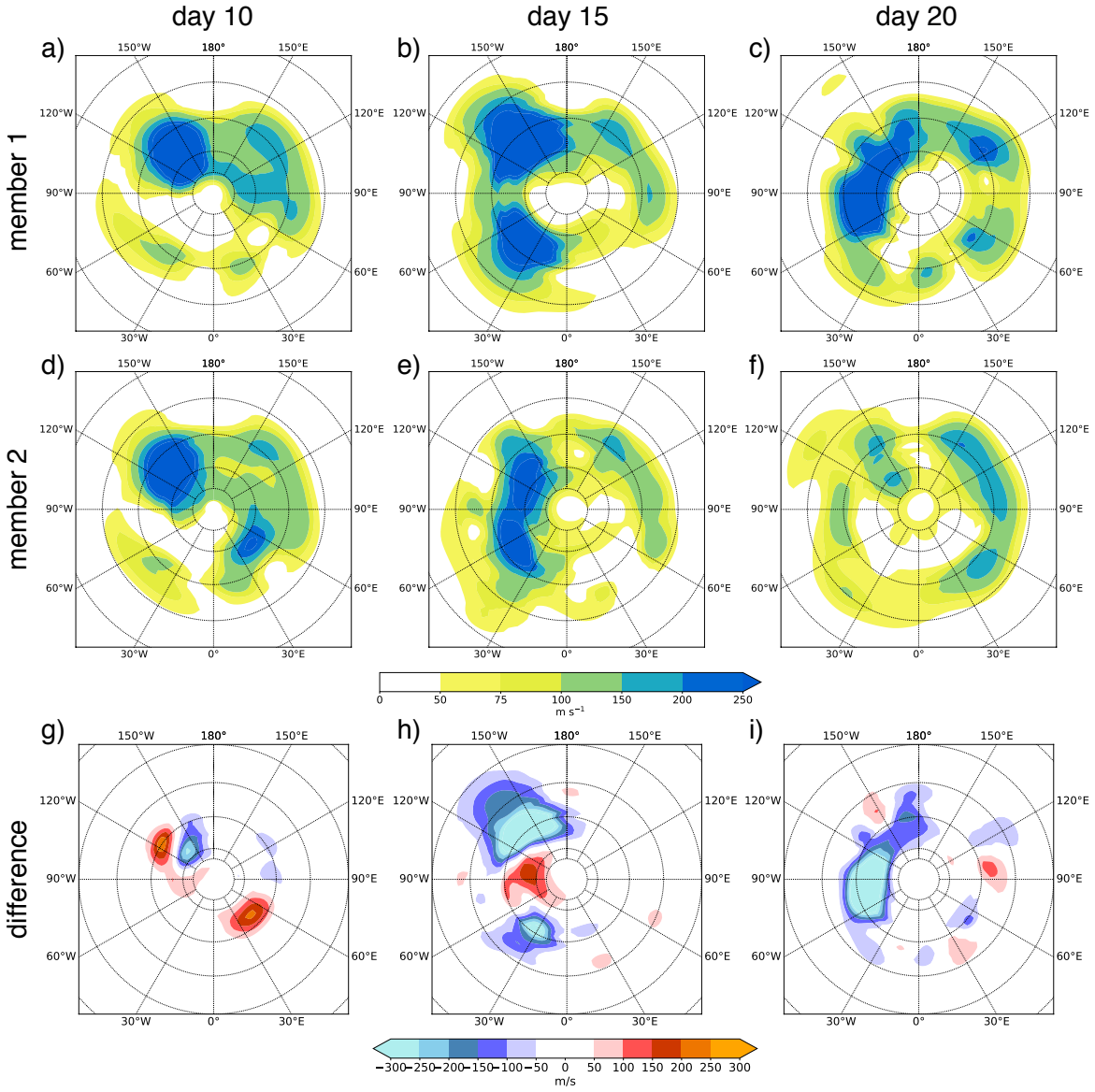

Figure 5.2: Rossby wave envelope, E, from member 1 of the October ensemble at a) day 10, b) day 15, and c) day 20 . The same for member 2 in d)–f) and for the envelope difference, ΔE, in g)–i). From Baumgart et al. (2019) © Copyright 2019 American Meteorological Society (AMS). Used with permission.

suggesting instead an error in the amplitude of the envelope.

At day 15, the PV error exhibits approximately the same scale and magnitude as the troughs and ridges within the Rossby wave pattern (Fig. 5.1c). At the same time, the envelope error ΔE is found over an extended part of the midlatitudes of the Western Hemisphere, with two large negative errors over the North East Pacific and North Atlantic sector and a positive error in between (Fig. 5.2h). The region with a

more zonally oriented tropopause (70–140°E) shows only small errors both in PV and the envelope.

Between day 15 and 20, the PV error amplification is less pronounced than previously (Fig. 5.1c and d), indicating that the PV error starts to saturate. The Rossby wave pattern in the Western Hemisphere seems to be completely decorrelated. This decorrelation appears as a large error in the envelope diagnostic, mostly in the form of an amplitude error (Fig. 5.2i). At the same time, more pronounced PV errors start to occur in the Eastern Hemisphere. These errors also become apparent as small errors in the envelope diagnostic"(Baumgart et al., 2019).

5.3 Spatio-temporal evolution of the error in the ensembles

"To quantify the relative importance of the processes governing the error growth, we consider all twelve cases including all pairwise combinations of the five-member ensembles. We start discussing the time series of the mean enstrophy error $\mathcal{P}$ and mean squared envelope error $\mathcal{E}$. Afterwards, the contributions of individual processes to error growth are quantified. Spatial maps of the squared envelope error are then discussed to identify 'error hot spots'. Finally, our results are compared with the conceptual three-stage error growth model of Zhang et al. (2007).

Time series of the mean enstrophy error ($\overline{\mathcal{P}}$) and mean squared envelope error ($\overline{\mathcal{E}}$) over the midlatitudes of the Northern Hemisphere are shown in Fig. 5.3 together with the (statistical) standard error for the cases.

Both the enstrophy and the envelope diagnostic show the typical form of an error-growth function (e.g., Selz, 2019): The initially very fast error growth seems to follow a power-law behaviour in the first two days (as seen on a log-log plot, not shown), which is followed by quasi-exponential growth until day 6–7. Afterwards, error growth slows down significantly, until the error eventually reaches saturation after a certain time.

Two main differences exist between the enstrophy and the envelope diagnostic. First, the envelope diagnostic shows larger differences between the 12 cases as measured

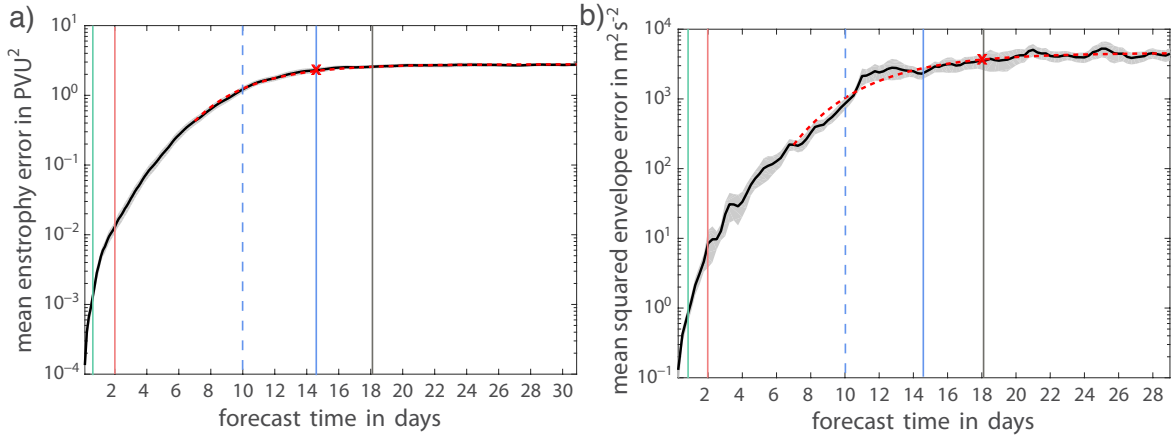

Figure 5.3: Time series of a) mean enstrophy error ($\overline{\mathcal{P}}$), and b) mean squared envelope error ($\overline{\mathcal{E}}$) over the midlatitudes of the Northern Hemisphere. $\mathcal{P}$ and $\mathcal{E}$ are averaged over the 12 cases and 10 member pairs within each case. These averages are shown as thick black lines, while the shading next to the lines denotes the (statistical) standard error for the 12 cases. The red dashed line shows the fit of the temporal development of the mean enstrophy error and mean squared envelope error to Eq. 5.5 and the red cross indicates the predictability time (as measured by Eq. 5.6) of the diagnostics. Panel a) has been produced by Marlene Baumgart. From Baumgart et al. (2019) © Copyright 2019 American Meteorological Society (AMS). Used with permission.

by the standard error. Second and more importantly, the envelope error saturates at a later time than the enstrophy error.

To quantify the different saturation levels in the enstrophy and envelope diagnostic, we calculate the predictability time τ in the two diagnostics, according to Selz (2019). For that purpose, the temporal development of $\overline{\mathcal{P}}$ and $\overline{\mathcal{E}}$ after day 7 is fitted to the following function with the fitting parameters a and b

$$\overline{\mathcal{X}} = \overline{\mathcal{X}}(t_0) \exp\left(a\left(1 - \exp(-b(t - t_0))\right)\right) \ , \tag{5.5}$$

where t_0 is set to 7 days as in Selz (2019) and $\overline{\mathcal{X}}$ denotes either $\overline{\mathcal{P}}$ or $\overline{\mathcal{E}}$. From Fig. 5.3 it is evident that Eq. 5.5 provides a very good fit for the temporal development of $\overline{\mathcal{P}}$ and $\overline{\mathcal{E}}$, respectively.

Selz (2019) defined the predictability time as the time when 80% of the error magnitude at $t \to \infty$ is reached, that means

$$\overline{\mathcal{X}}(\tau) = 0.8\overline{\mathcal{X}}(t_\infty) = 0.8\overline{\mathcal{X}}(t_0) \exp(a) \ . \tag{5.6}$$

With this definition, we derive a predictability time of about 14.5 days for the enstrophy diagnostic and of about 18 days for the envelope diagnostic. For difference kinetic energy, Selz (2019) derived a predictability time of 17 days, which lies in between the result for the enstrophy and envelope diagnostic. This intermediate time can be explained by the fact that the enstrophy spectrum has larger weight on small scales than kinetic energy, while small scales are filtered out in the envelope diagnostic.

Based on Fig. 5.3, we are able to quantitatively derive a time lag of 3.5 days between the enstrophy diagnostic (which saturates at the synoptic scale) and the envelope diagnostic (which instead reaches saturation at the planetary scale). This suggests that the predictability of individual ridges and troughs in a Rossby wave pattern is about 3.5 days shorter than the predictability of the wave-pattern envelope.

The spatial distribution of the squared envelope error, $(\Delta E)^2/2$, at day 5, 10, 15, and 20 is shown in Fig. 5.4. At day 5, the envelope error appears still very localized and small in magnitude. At day 10 (Fig. 5.4b), two distinct error regions are found around $120-90°$W and around 30°W. By day 15 (Fig. 5.4c), large error amplification occurs in the Western Hemisphere: an extended region of large error is found around $150-110°$W and secondary maxima are found around 180° and over an "error belt" extending from North America towards Europe. Between day 15 and 20 (Fig. 5.4c and d), error growth continues further both in magnitude and in its spatial extension. At day 20 (Fig. 5.4d), the error affects almost the whole mid-to-high latitudes of the Northern Hemisphere. At this stage, the predictability time in the envelope diagnostic is already reached (see Sec. 5.35.3, Fig. 5.3b).

From Fig. 5.4 it is evident that the envelope error tends to appear and amplify more in the western portion of the Northern Hemisphere, whereas in the eastern portion its magnitude is lower and its spatial extent more confined. This difference may be due to the fact that in our cases the Rossby wave amplitude was, in general, weaker in the eastern than in the western Northern Hemisphere"(Baumgart et al., 2019). This particular feature was also observed in the Rossby wave activity climatology presented in section 4.3.

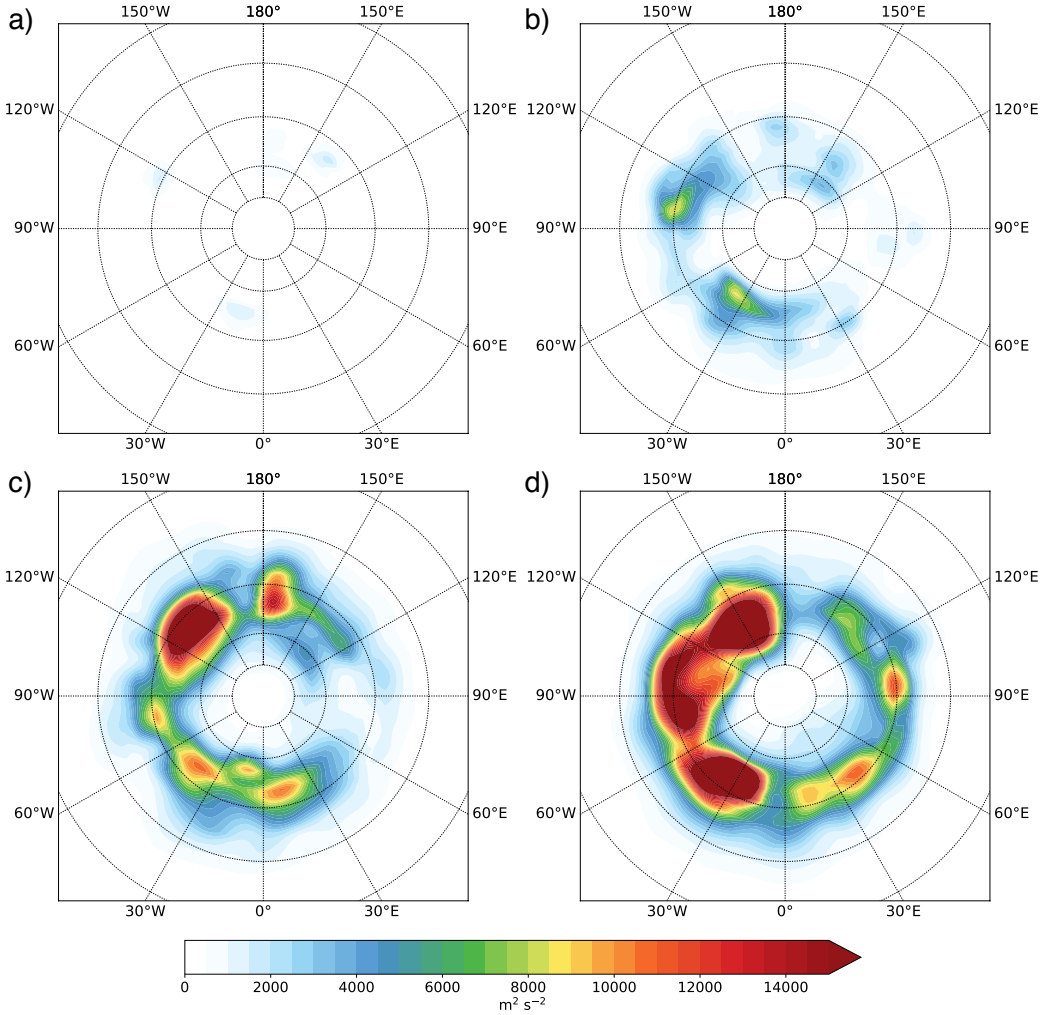

Figure 5.4: Squared envelope error $(\Delta E)^2/2$ averaged over the 12 cases and 10 member pairs within each case at a) day 5, b) day 10, c) day 15, d) day 20. From Baumgart et al. (2019) © Copyright 2019 American Meteorological Society (AMS). Used with permission.

Chapter 6

Rossby wave packets dynamics from a LWA perspective

In this chapter we discuss the application of the filtered LWA budget in two idealized simulations (barotropic model on the sphere and dry primitive equation model) and in an operational weather forecast model. In this section we use the zonal filter with a Hann window of constant width to perform the phase averaging on LWA and its budget. These results have been submitted to (Ghinassi et al., 2019, manuscript under review; the portions of the text which appear in the submitted manuscript are identified with quotation marks).

6.1 Barotropic model simulation with pseudo-orographic forcing

This section aims to test our diagnostic framework in a barotropic model simulation to identify local sources and sinks of filtered LWA. The interpretation of these results is rather straightforward and, therefore, a helpful step towards the situation in more complex three-dimensional flows, which will be the subject of the two subsequent sections.

6.1.1 Model setup

We consider a forced-dissipative model configuration with pseudo-orographic forcing similar to section 4.1.2:

$$\frac{\partial q}{\partial t} = -J(\psi, q) + N_{\mathrm{q}} \ , \tag{6.1a}$$

$$N_{\mathrm{q}} = F - \alpha(q - q_0) - \nu\nabla^4(q - q_0) \ . \tag{6.1b}$$

"The term F in (6.1b) is now defined such as to provide a source of LWA which is both local and transient,

$$F(\lambda, \phi, t) = -\nabla \cdot [\mathbf{v}_0 f \, \Gamma(\lambda, \phi) \sin^2 \Omega_{\mathrm{f}} t] \ , \tag{6.2}$$

where $\mathbf{v}_0$ is the horizontal wind at initial time and $\Gamma(\lambda, \phi)$ is a non-dimensional Gaussian function. The Gaussian has a maximum height of 0.15, is centred at (30° N, 30° E), and has an elliptic base with a standard deviation of 7.5° and 30° in the zonal and meridional direction, respectively. The period of the forcing is set to be 24 days by choosing $\Omega_{\mathrm{f}} = \pi/24 \ \mathrm{days}^{-1}$. The interaction of the flow with the pseudo-orography gives rise to Rossby waves that subsequently propagate eastward in the sense of the group velocity. Therefore, in this setup orography has to manifest as a source of LWA. In our simulations we set the timescale for linear relaxation equal to $\alpha = (15 \, \mathrm{days})^{-1}$ and the coefficient of hyperviscosity to $\nu = 10^{15} \ \mathrm{m}^4 \ \mathrm{s}^{-1}$. We expect both linear relaxation and the hyperdiffusion to damp waviness and therefore to act as a sink of LWA " (Ghinassi et al., 2019)

As initial condition we specify the same zonal background flow $u(\phi, t = 0)$ defined in (4.3). This initial wind profile consists of a barotropically stable westerly jet at $\phi = \pm 30°$ and easterly winds at the equator and in the deep tropics (see Fig 4.1a in section 4.1.1). The wind profile is associated with substantial meridional gradients of q_0 around $\phi = \pm 30°$ (Fig. 4.1b), which allow RWPs to propagate downstream of the forcing.

"For the numerical simulations we use a standard pseudo-spectral method with triangular truncation at T89 and a leapfrog time-stepping scheme in combination with a

Robert-Asselin-Williams filter (Williams, 2011) to damp the growth of the computational mode. The corresponding physical grid has a resolution of $2^\circ \times 2^\circ$ in longitude and latitude. The model is integrated with a time step $\Delta t = 900$ s for 24 days, which corresponds to one period of the pulsation of our forcing.

LWA and the corresponding terms in the LWA budget equation are computed globally using 6-hourly model output of q and (u, v). This is done in order to simulate the availability of model data from more complex models or reanalyses, which usually do not provide output every model time-step, but typically only every few hours.

6.1.2 Results

At first, we consider day 10, at which the orographic forcing is close to its maximum and, therefore, likely to be stronger than the dissipation. The potential vorticity field at this time (Fig. 6.1a) shows an area of waviness located above the forcing region and extending downstream, and it is in these regions that we find elevated values of A (Fig. 6.1b). Over these regions, $(\partial A/\partial t)\cos\phi$ is positive, which means that LWA increases (Fig. 6.1c). The conservative term T_C at day 10 (Fig. 6.1d) is negative over the forcing region and positive more downstream, suggesting that LWA is radiated away from the orographic source. This happens especially in the south-east direction, although a small positive region is also found north-east of the forcing. We believe that one of the factors related to such asymmetry in the meridional component of RWP radiation is the spherical geometry, which profoundly affects the horizontal propagation of the waves (Hoskins and Karoly, 1981; Held, 1983; Orlanski, 2003). There is a large region above the orographic forcing with positive values of the non-conservative term T_N, which confirms its role as a source of LWA, as expected. A region in which the local non-conservative term is negative is found further downstream and equatorward of the orographic forcing, and it is presumably associated with damping of LWA due to friction and diffusion. The contribution from T_Q is not shown in these maps, since its magnitude is much smaller compared to the other budget terms (see Fig. 6.2 below).

As indicated in the methodology section, we generally computed the non-conservative term T_N as a residual. In the barotropic simulation, we alternatively computed T_N using the explicit formula (2.56c), with N_q defined according to (6.1b). The comparison

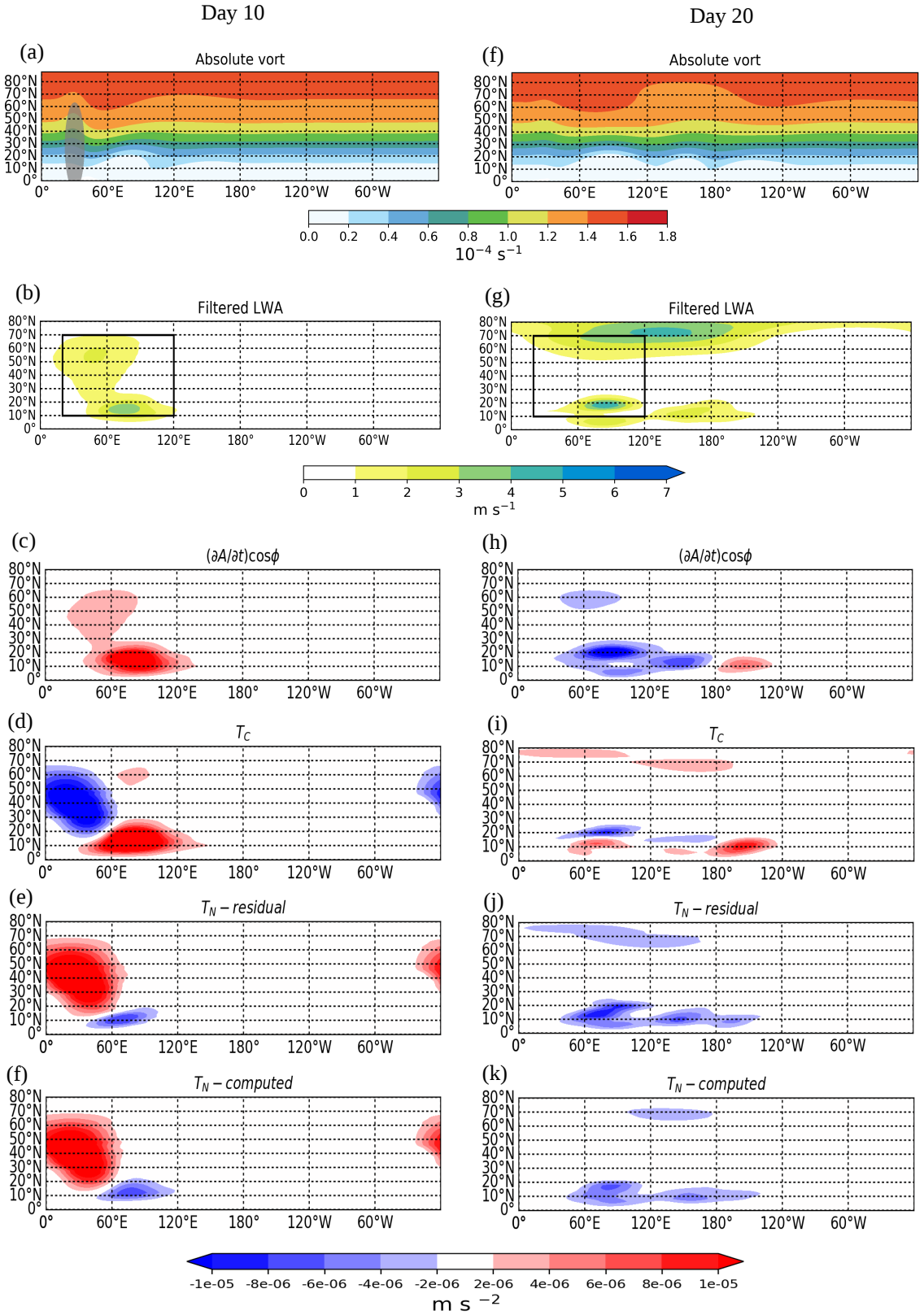

Figure 6.1: Analysis of the barotropic model simulation after 10 days (left column) and after 20 days (right column) of integration. (a) and (f): Potential vorticity, (b) and (b): filtered LWA A, (c) and (h): $(\partial A/\partial t)\cos\phi$, (d) and (i): conservative term T_{C}, (e) and (j): local non-conservative term T_{N} computed as a residual, (f) and (k): T_{N} computed by meridionally integrating N_q from (6.1b). colour bar and units for panels (c)–(e) and (h)–(k) are the same. The grey shading in (a) represents the region in which the amplitude of the pseudo-orographic forcing exceeds 0.075. The rectangles in (b) and (d) mark the area used later for spatial averaging.

of the residual computed integrating N_q (Fig. 6.1f and k) with the corresponding computation of T_N as a residual (Fig. 6.1e and j) shows broad agreement both in terms of the overall shape and in the amplitude the respective fields. This indicates that the numerical error incurred due to the finite differencing in computing (2.55), together with numerical diffusion introduced by the time filter are noticeable, but small.

At day 20, the orographic forcing is close to zero, and at this time we expect non-conservative processes to dominate and act as a sink of LWA. Figure 6.1j shows that this is, indeed, the case: T_N is negative everywhere. LWA itself (Fig. 6.1g) has continued an overall eastward shift, and we can identify three wave packets: The first lies poleward of the orography (north of 65° N) and is well extended in longitude, and we will refer to it as the *poleward RWP*. Two other wave packets are more longitudinally confined and located on the equatorward flank of the jet (the location of jet maximum is at around 30 ° N); we will refer to them as the *first equatorward RWP* (at around 20 ° N and between 60°–120° E) and the *second equatorward RWP* (at 15° N and 120° E – 160° W). The values of $(\partial A/\partial t)\cos\phi$ at this time are negative in a large portion of the domain (Fig. 6.1h), implying an overall decrease of LWA in the absence of forcing. The poleward wave packet is almost stationary, consistent with the fact that only a small (compared to the wave packet extension) region of negative LWA tendency is found on the rear of the RWP. The first equatorward wave packet is decaying ($(\partial A/\partial t)\cos\phi$ is negative here), whereas the dipole of positive/negative $(\partial A/\partial t)\cos\phi$ associated with the second equatorward wave packet suggests that it is propagating eastward along the zonal direction. The conservative term T_C (Fig. 6.1i) shows, at low latitudes, areas of positive and negative values in close proximity to each other, indicating RWP propagation in a southerly or south-easterly direction.

Fig. 6.1 clearly indicates that the non-conservative term T_N may be either predominantly positive (day 10) or negative (day 20), and in our experiment this depends on whether the weak dissipation is overwhelmed by strong orographic forcing (day 10) or not (day 20). By contrast, the conservative term T_C shows approximately as much positive as negative values. In fact, this is to be expected since finite amplitude wave activity is globally conserved for purely conservative conditions in the barotropic model (Nakamura and Zhu, 2010; Solomon and Nakamura, 2012). This means that conser-

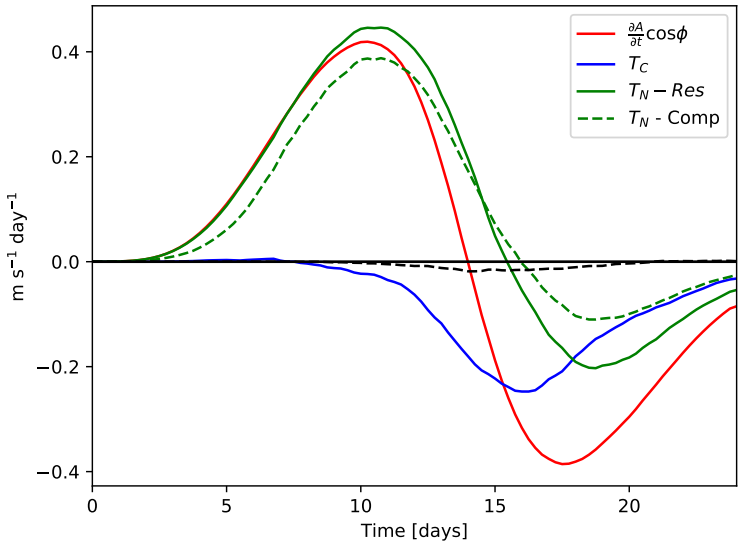

Figure 6.2: Time evolution of the LWA budget terms in the barotropic simulation averaged over a finite region that includes the orography: $(\partial A/\partial t)\cos\phi$ (red line), conservative term T_{C} (blue line), local non-conservative term T_{N} estimated a residual (green line) and computed by meridionally integrating N_q from (6.1b) (dashed green line) and non-local non-conservative term T_{Q} (dashed black line).

vative processes essentially act to redistribute LWA across the surface of the sphere without affecting globally integrated LWA.

To further analyze the LWA budget, Fig. 6.2 shows the evolution of spatially averaged terms from (2.55). Here, spatial averaging is performed over a finite region delimited by 60–10° N, 20–120° E (marked in Fig. 6.1b and g), which contains the orographic forcing. During the first 16 days the non-conservative term T_{N} is positive implying that orographic LWA generation dominates over LWA dissipation. The averaged conservative term is zero until approximately day 7, suggesting that the LWA created by the forcing is still confined within the region used for averaging. Thereafter, this term becomes negative, which means that LWA is radiated away leading to a net export from the considered region. After day 16 the non-conservative term T_{N} becomes negative, which means that dissipation of LWA starts to dominate over forcing. The term T_{Q} is very small and always negative (black dashed line in Fig. 6.2). The two methods to compute the non-conservative term T_{N} in Fig. 6.2 exhibit some differences in the magnitude, but the overall temporal behaviour of the two curves is very similar. One can interpret the difference between the solid and the dashed green

line as a broad estimate for the uncertainty related with the computation of the budget terms and numerical diffusion. This suggests that the main features discussed above are significant and not a result of numerical errors and demonstrate the possibility of quantifying nonconservative sources and sinks of LWA using (2.55)" (Ghinassi et al., 2019).

6.2 Dry primitive equation model

In this section we apply the primitive-equation version of the LWA budget to simulations of idealized RWP life cycles in a dry general circulation model. These simulations allow us to study the full three-dimensional flow in a quasi-realistic midlatitude set-up, including the partitioning of the conservative term into the different contributions as described in (3.8).

6.2.1 Model setup and simulation

"For our simulations we use the so-called "Portable University Model of the Atmosphere" (short: PUMA, Fraedrich et al. 2005). PUMA is a spectral model which solves the primitive equations on the sphere. Our experiments include neither moisture nor orography. All tendencies from physical processes are parameterized as linear relaxation like in Held and Suarez (1994). This corresponds to linear friction in the momentum equation and Newtonian cooling in the heat equation, respectively. The reference temperature for the Newtonian cooling term includes a local dipole in the Northern Hemisphere, superimposed on an otherwise zonally symmetric profile similar as in Frisius et al. (1998) and Fraedrich et al. (2005). This dipole locally increases cooling at higher latitudes and warming at lower latitudes. The strength of the dipole is largest at lower levels and decreases to zero in the upper troposphere and above. The precise formulation of the reference temperature field for the Newtonian cooling is provided in Appendix B. This device creates a local region of enhanced low-level baroclinicity, resulting in downstream eddy development like in an idealized strom track experiment (Chang and Orlanski, 1993; Frisius et al., 1998). What we expect to see is the growth and the upward and eastward propagation of baroclinic eddies originating

from the low-level dipole region, and this should manifest itself as a source of LWA in the upper troposphere through the conservative term T_{C}. Newtonian cooling, which implies a direct diabatic modification of PV, may act either as a source or as a sink of LWA on the instantaneous flow field; however, we expect such linear relaxation to overall damp LWA. Similarly, friction and hyperdiffusion are expected to always damp LWA as for the barotropic case.

PUMA is run for 2 years under perpetual equinox conditions (no seasonal or diurnal cycles) with spectral resolution T42, with 20 vertical levels and with a time step of 30 minutes. Friction is applied only to the four lowermost levels. The relaxation timescale for Newtonian cooling is set to 4 days near the surface increasing to 30 days in the upper troposphere and above. Every six hours the model output is interpolated onto a regular $2^\circ \times 2^\circ$ (longitude $\times$ latitude) grid on equispaced pressure levels ranging from 850 to 100 hPa. The first year of the simulation is discarded to eliminate the model spin up, and our analysis is performed only on the second year. LWA is computed only for the Northern Hemisphere" (Ghinassi et al., 2019).

6.2.2 Results

An analysis of snapshots of PV and filtered LWA reveals that our simulation, indeed, produces upper tropospheric RWPs that originate over the dipole region, then grow while propagating downstream, and eventually decay, which is often associated with wave breaking. An example of consecutive snapshots of PV and filtered LWA for a random period of our PUMA simulation is provided in Figure 6.3. "In our PUMA simulation we have less control over the generation of RWPs than in the previous barotropic model simulation. In the latter, in fact, RWPs were directly generated by the pseudo-orographic forcing term. By contrast, in the PUMA simulation the opposing tendencies from baroclinic instability and general dissipation result in a chaotic transient flow, and it is not possible to predict the temporal behaviour of LWA. This fact motivates us to consider the time-averaged behaviour first and thereafter to analyse episodes of transient RWPs" (Ghinassi et al., 2019).

One-year climatologies of the zonally averaged potential temperature and zonal wind are shown in Figure 6.4. In particular the zonally averaged zonal wind in the

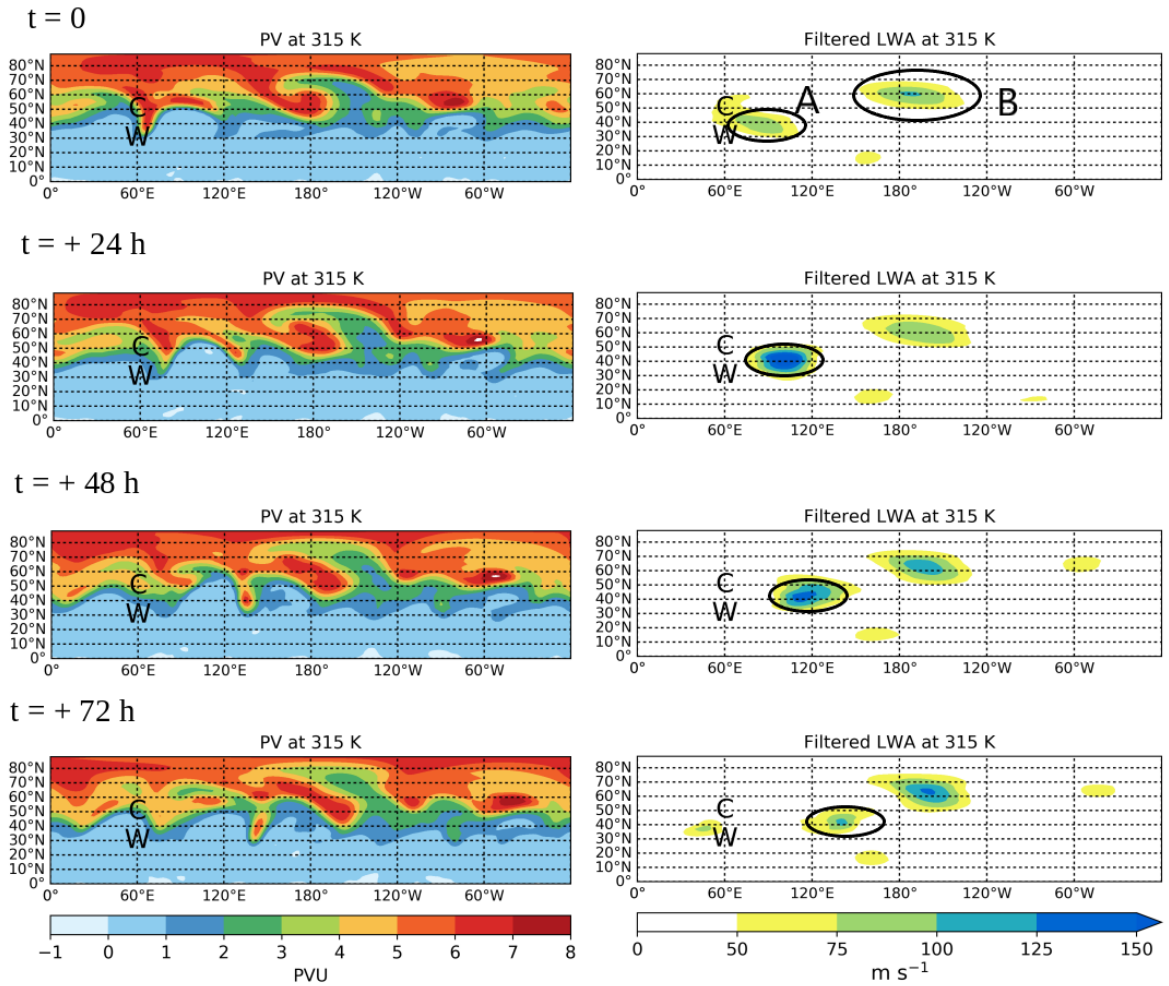

Figure 6.3: Left panels: snapshots of PV (in Potential Vorticity Units, 1 PVU = 10^{-6} K kg^{-1} m^2 s^{-1}) in the upper troposphere (at 315 K). Right panels: filtered LWA A computed from the PV snapshots showed on the left. Maps of PV and A are shown at four consecutive times of the PUMA simulation every 24 h. The letters C and W in all plots mark the centres of the cold and warm anomalies in the relaxation temperature field. Note how in the filtered LWA plot a RWP (labelled A at t=0) is found immediately downstream of the dipole at the initial time. This transient RWP propagates eastward in the considered period and its amplitude substantially increases after 24 h. Between 48 and 72 h its amplitude instead decreases as it enter its decay phase. Note the other region of waviness associated with a large amplitude ridge far away from the dipole (labelled B at t=0) which instead remains almost stationary in longitude during the considered period, resembling blocking.

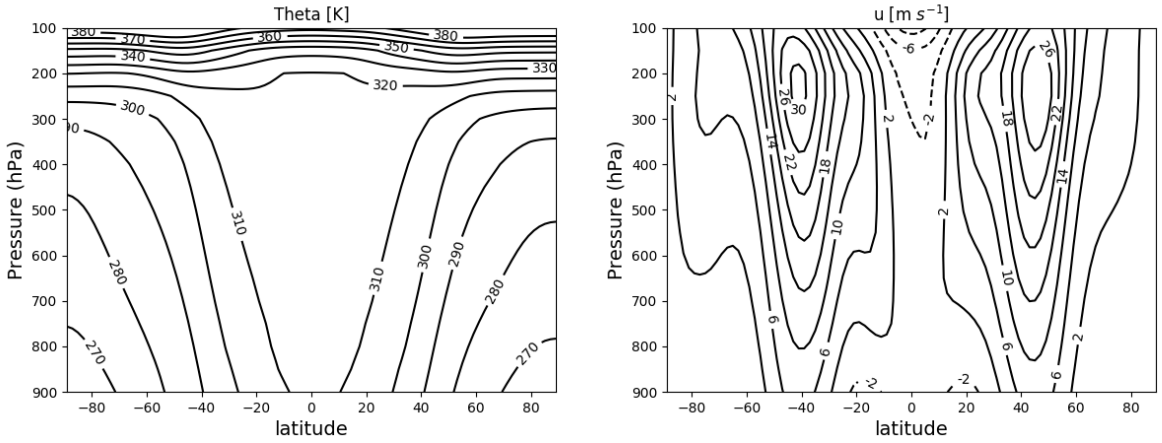

Figure 6.4: Cross sections (on the meridional-vertical plane) of the zonally averaged annuanl mean of potential temperature (left panel) and zonal wind (right panel) from the PUMA experiment.

Northern Hemisphere, which contains the localised storm track, exhibits weaker westerlies in the upper troposphere (at around 300 hPa) and slightly stronger westerlies in the lower and mid troposphere (between 800 and 600 hPa). This translates into a more barotropic structure of the Northern Hemisphere jet stream compared to the Southern Hemisphere and can be interpreted as a preliminary evidence that the zonally averaged circulation in the Northern Hemisphere contains a larger amount of wave activity compared to the Southern one, for the reasons discussed in section 2.3.3.

"Latitude-longitude maps of the one-year climatologies of relevant quantities on the 315 K isentrope are shown in Figure 6.5. This particular isentrope is chosen since it intersects the tropopause in the midlatitudes, where a considerable isentropic PV gradient is found (see PV in Fig. 6.5b). The map of time-averaged zonal wind (Fig. 6.5a) shows a strong, narrow jet over the dipole region associated to the strong PV gradient (Fig. 6.5b), whereas downstream both the jet and the associated PV gradient appear weaker. Time-averaged LWA (Figure 6.5c) features a longitudinally extended maximum in the midlatitudes downstream of the heating dipole. This maximum arises from the transient Rossby wave activity associated with RWPs in this region.

Another secondary maximum of LWA is found to the south of the warm anomaly; this confined pocket of LWA appears to be associated with very low values of PV and is arguably a result of the diabatic heating happening below (see Fig. 6.6 for discussion).

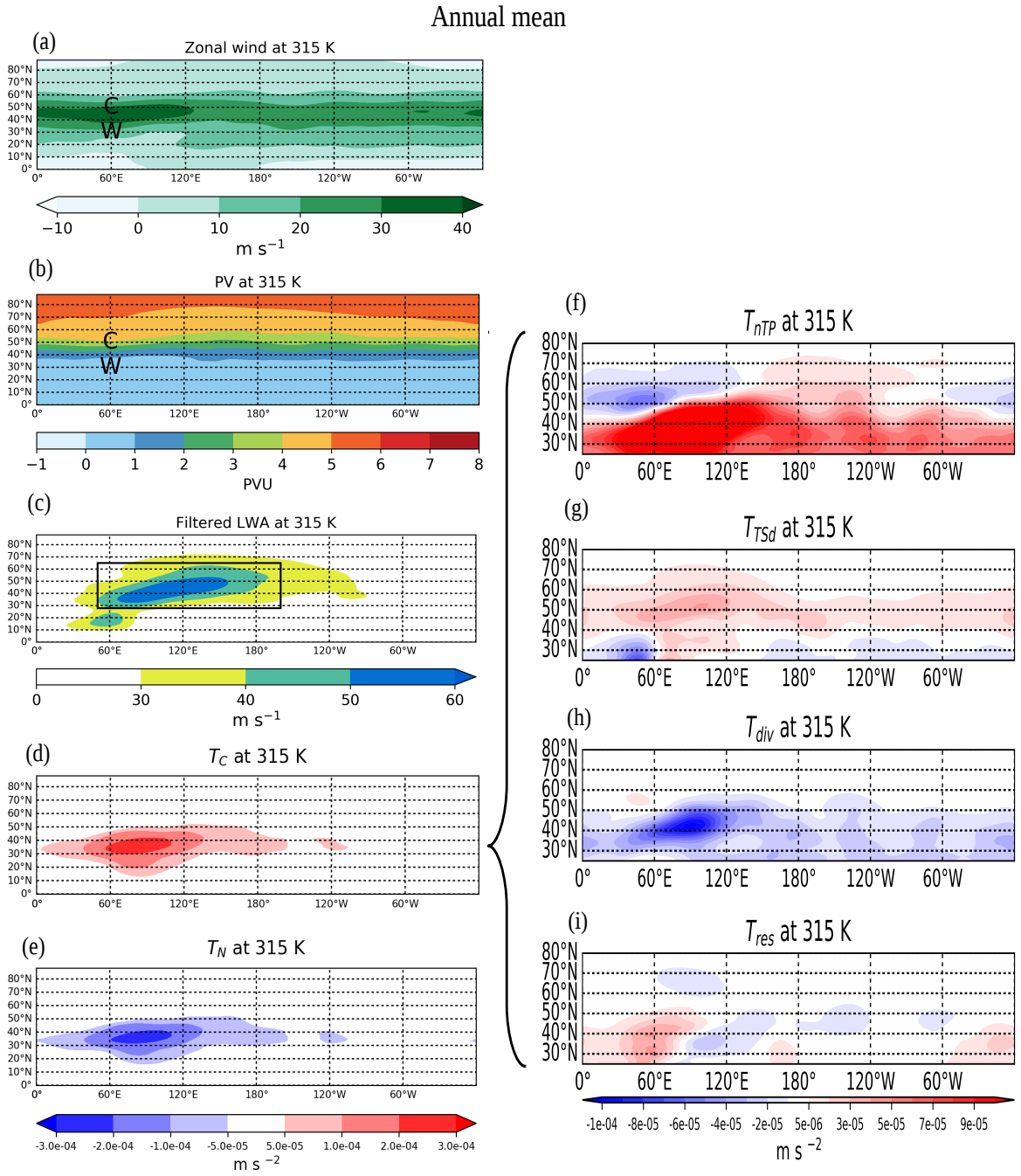

Figure 6.5: Left panels: time averaged variables on the 315 K isentrope from the PUMA model simulation: (a) zonal wind, (b) PV (in Potential Vorticity Units, 1 PVU = 10^{-6} K kg^{-1} m^2 s^{-1}), (c) filtered LWA, (d) conservative term T_{C} , and (e) local non-conservative term T_{N}. The letters C and W in (a) and (b) mark the centres of the cold and warm anomalies in the relaxation temperature field; the rectangular box in (c) marks the area for the spatial averaging used below in connection with Figs. 6.7 and 6.8. Units and colour bar are the same for panels (d) and (e). Right panels: time averaged contributions to T_{C} on the 315 K isentrope, (f) near-tropopause T_{nTP}, (g) tropospheric-deep T_{TSd}, (h) divergent T_{div} and (i) T_{res}, i.e. the contribution which would arise from the residual wind in the PPVI. Units and colour bar are the same for all panels. Note the different colour bar compared to T_{C}.

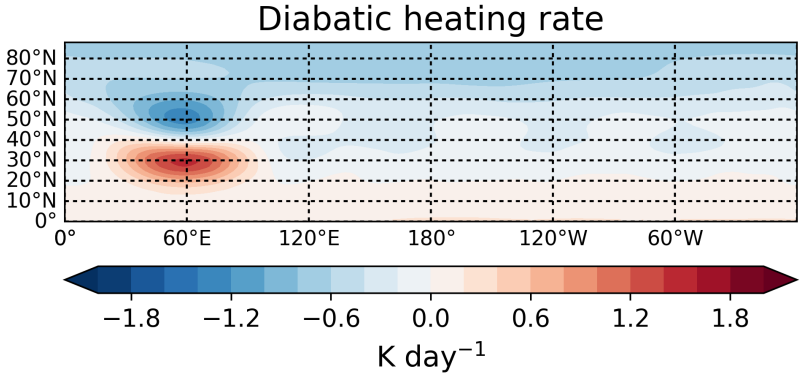

Figure 6.6: Annual mean of the vertically averaged diabatic heating rate (in K per day) in the lower troposphere (between 600 and 900 hPa). The diabatic heating rate at each time is computed as $D\theta/Dt = -(\theta - \theta_\mathrm{R})/\tau_\mathrm{R}$, where θ_R is the potential relaxation temperature (computed from the relaxation temperature defined in eq. B.2 in Appendix B) and τ_R denotes the relaxation time scale for Newtonian cooling. Note that in our setup τ_R increases along the vertical to mimic a stronger diabatic heating in the lower troposphere and a quasi-adiabatic atmosphere in the upper troposphere. The material derivative of Ertel PV considering only diabatic heating can be approximated as $DP/Dt \approx -g(f + \zeta_\theta)\, \partial/\partial p(D\theta/Dt)$. In our setup, above the warm anomaly the vertical gradient of the heating rate is negative, since the heating rate decreases with height. This leads to a decrease of P above the warm anomaly.

Regarding the time-mean LWA budget, we first note that the tendency term $(\partial A/\partial t)\cos\phi$ as well as T_Q are very small (not shown) as expected for a climatology. The conservative term T_C (Fig. 6.5d) is positive throughout the domain shown, most notably over the dipole region and immediately downstream. This is in stark contrast with the barotropic model simulation above, where we saw positive and negative areas of similar size and magnitude. The key difference between these two model configurations is their dimensionality. The barotropic model describes two-dimensional horizontal flow, and the conservative term only redistributes wave activity with zero net source or sink upon horizontal averaging. Similarly, the conservative term can be expected to merely redistribute wave activity in the PUMA simulation, however this process now includes also the vertical dimension (see 2.4). This implies that the conservative term at one particular isentropic level spanning the upper troposphere may well be positive everywhere throughout the domain, as it is the case in our simulation. The conservative LWA generation is balanced by non-conservative term T_N (Fig. 6.5e). This is plausible because the term T_N includes linear relaxation of temperature towards a zonally

symmetric state, which corresponds to a tendency to suppress waviness.

The left panels of Figure 6.5 disentangles the different contributions to T_{C} (as detailed in (3.8)) in the climatology. The background PV state for the PPVI for the PUMA experiment is defined as the annual mean. Figure 6.5f shows that the conservative dynamics associated with the near-tropopause wind contribution T_{nTP}, which also includes the contribution from $\mathbf{v}_{\mathrm{bg}}$, is positive almost everywhere in the considered domain, apart from a region of negative values in the vicinity of the cold anomaly. The tropospheric deep wind contribution T_{TSd} (Fig. 6.5g) is positive in the midlatitudes, especially immediately downstream of the dipole. Note that T_{TSd} has a lower magnitude compared to T_{nTP}. This is consistent with the fact that in our upper-tropospheric analysis, the influence along the vertical of PV and potential temperature perturbations located near the surface is lower compared to the PV anomalies located into the mid and upper troposphere. The T_{div} contribution is always negative (Fig. 6.5h), in particular immediately downstream of the dipole, implying a negative LWA tendency. We also investigated the contribution to the conservative dynamics of LWA that would arise from $\mathbf{v}_{\mathrm{res}}$, namely T_{res} and found that it has a magnitude comparable to T_{TSd} and T_{div} only in the vicinity of the dipole and decreases to smaller values further away (see Fig. 6.5i). The fact that the T_{res} is found larger in the proximity of the warm anomaly is presumably related to a larger error in the wind obtained through PPVI due to the reduced static stability over this region. Such neglected contribution would only marginally affect the LWA dynamics over the region where the averaging is performed, which is located mostly downstream of the dipole.

We now shift our attention to the transient RWPs that underly the climatological mean picture. Similar as for the barotropic model, we produced time series by averaging all terms in the LWA budget over a finite box (shown in Fig. 6.5c) which contains the region of enhanced transient Rossby wave activity. A first look at the time series (time series for the first 30 days are shown in Fig 6.7) reveals that the increase of LWA ($(\partial A/\partial t)\cos\phi$) tends to occur in burst-like events, followed by a rapid decay of the growth rate. This behaviour is likely to be an upper tropospheric signature of periodic bursts of baroclinic eddy activity, which is observed both in idealized simulations and in real data of storm tracks (Novak et al., 2017; Ambaum and Novak, 2014). In order

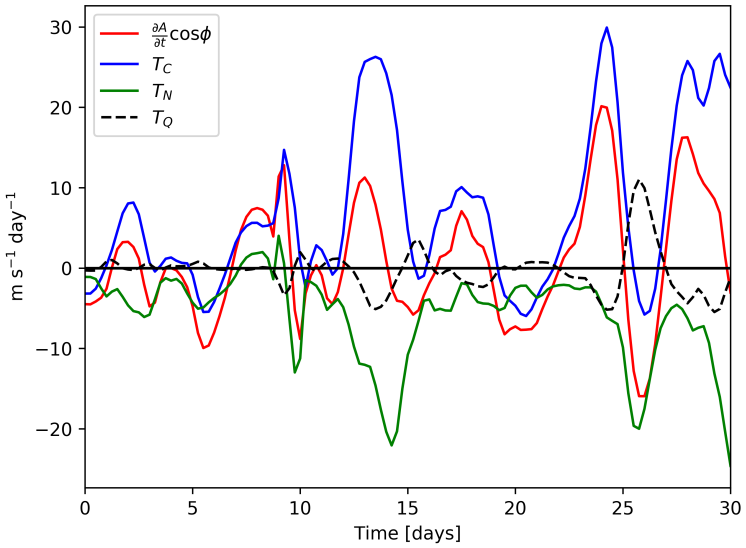

Figure 6.7: Time series of the first 30 days of the terms from the LWA budget equation (2.72) on the 315 K isentrope in the PUMA-simulation: $(\partial A/\partial t)\cos\phi$ (red line), conservative term T_{C} (blue line), local non-conservative term T_{N} (green line), and non-local non-conservative term T_{Q} (dashed black line). All terms in the LWA budget are averaged over the strom-track region (indicated by the box in Fig. 6.5c).

to obtain an average picture of such events, we now onsider a composite average by selecting those maxima of $(\partial A/\partial t)\cos\phi$ that exceeded 10 m s^{-1} per day and then taking a time window of ± 5 days centred over the respective $(\partial A/\partial t)\cos\phi$ peaks. With this criterion, a total of 46 episodes of LWA growth and decay that occurred during our one year integration are examined. The resulting composite (Fig. 6.8a) shows that the growth rate of LWA during these transient events indeed occurs with peaks of positive values of $(\partial A/\partial t)\cos\phi$ followed by a rapid decrease. The growth rate of LWA then becomes negative about 1 day after the peak. These LWA growth episodes are accompanied by positive values of the conservative term T_{C}, consistent with our earlier interpretation that the growth on the chosen upper-tropospheric isentrope is essentially due to conservative upward propagation of LWA. The non-conservative term T_{N} is always negative and indicates a sharp decrease immediately after the peaks in $(\partial A/\partial t)\cos\phi$ and T_{C}. This suggests that the LWA damping through linear relaxation and dissipation increases to counteract the conservative growth of LWA shortly after the burst, eventually leading to a negative tendency of $(\partial A/\partial t)\cos\phi$. The term T_{Q}, which is related to the non-conservative modification of $Q(\phi, t)$, is one order of magnitude

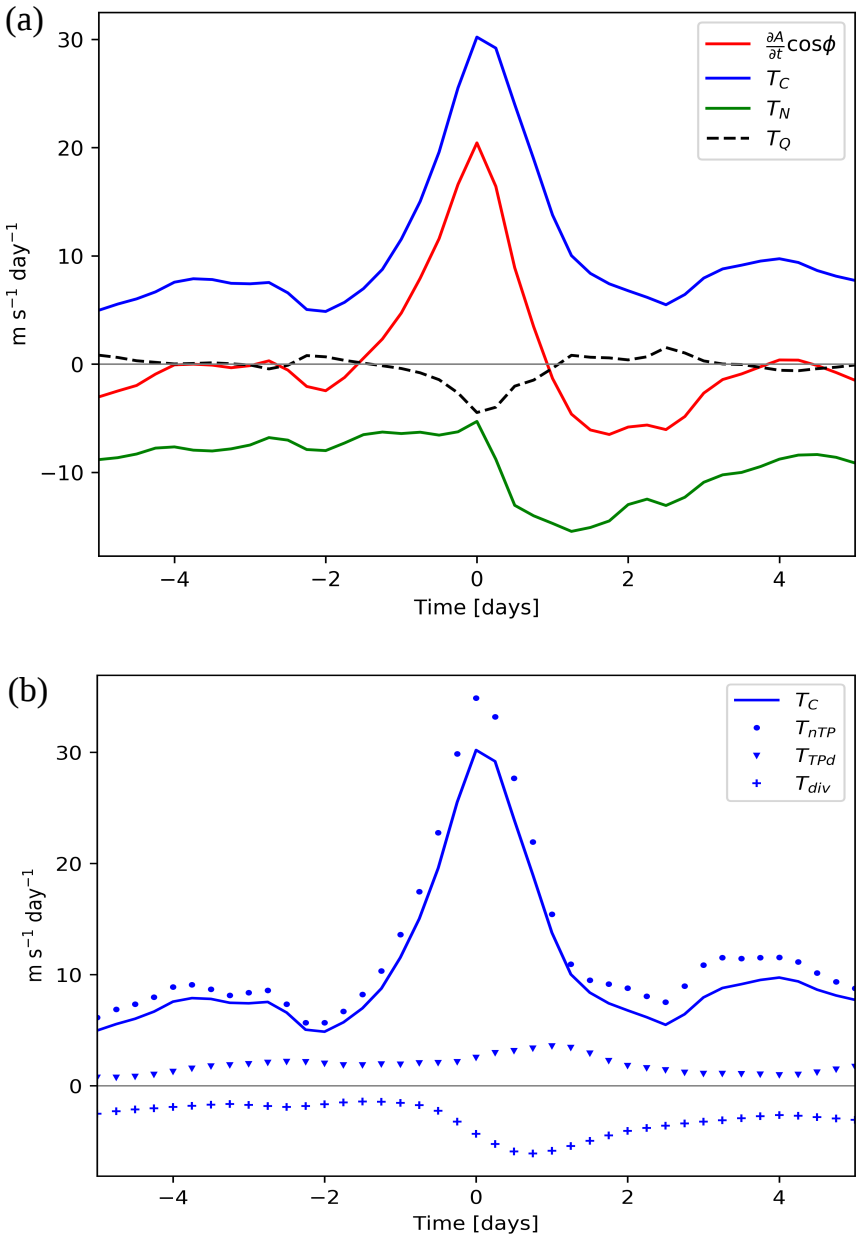

Figure 6.8: Composite mean of the time series of the terms from the LWA budget equation (2.72), averaged over the strom-track region (indicated by the box in Fig. 6.5c) on the 315 K isentrope in the PUMA-simulation. (a) $(\partial A/\partial t)\cos\phi$ (red line), conservative term T_{C} (blue line), local non-conservative term T_{N} (green line), and non-local non-conservative term T_{Q} (dashed black line); (b) same as in (a) but for T_{C} and its partitioning into near-tropopause (T_{nTP}, blue dots), tropospheric-deep (T_{TSd}, triangles) and divergent (T_{div}, plus) contributions).

smaller compared to the other terms; it decreases during the peaks of $(\partial A/\partial t)\cos\phi$ and it recovers immediately afterwards.

We now investigate the time behaviour of the different contributions to T_{C} for the composite event. Figure 6.8b shows that in the time mean the conservative dynamics LWA tendency is mainly associated with the near-tropopause wind contribution T_{nTP}, as observed in the analysis of the climatology maps discussed previously. As expected, the tropospheric deep wind contribution T_{TSd} is always positive, with a lower magnitude compared to T_{nTP}. The magnitude of T_{TSd} slightly increases about one day after the peaks of T_{C}. This growth input from the lower levels is likely to be associated with the positive feedback of upper level PV anomalies interacting with the lower PV and temperature anomalies during baroclinic instability (Hoskins et al., 1985; Methven et al., 2005), as discussed in section 2.2. The T_{div} contribution is always negative and acts to decrease the wave packets amplitude, in particular after the T_{C} peak.

We now apply our diagnostic to a snapshot of the flow containing a large RWP (see Fig. 6.9), in order to obtain insight into its dynamics at a particular time, which is the main scope of the present work. The map of filtered LWA (Fig. 6.9b) shows a major RWPs in the vicinity of the dipole (approximately at 40° N and between 50°–100° E) associated with a PV trough and a ridge located immediately to the East (Fig. 6.9a). This RWP will be referred to as the first RWP in the following. Another region of waviness is located further downstream (approximately between 120°–190° E), where the flow looks more nonlinear and resembles wavebreaking (see PV map in Fig. 6.9a). Compared to the first RWP, this second RWP is associated with smaller values of LWA, while they are distributed over a larger region. The tendency $(\partial A/\partial t)\cos\phi$ associated with the first RWP is negative at the trailing edge and positive at the leading edge, suggesting eastward propagation. Another region of positive $(\partial A/\partial t)\cos\phi$ is found in proximity of the large amplitude ridge belonging to the second RWP, implying an amplitude increase of this structure. The non-conservative term T_{N} is mainly negative over the considered domain, especially where the first RWPs is located. This is consistent with Newtonian cooling acting as a sink of wave amplitude. In the second RWP the contribution from T_{N} is very small.

The partitioning of T_{C} into the different contributions (Fig. 6.10) emphasizes again

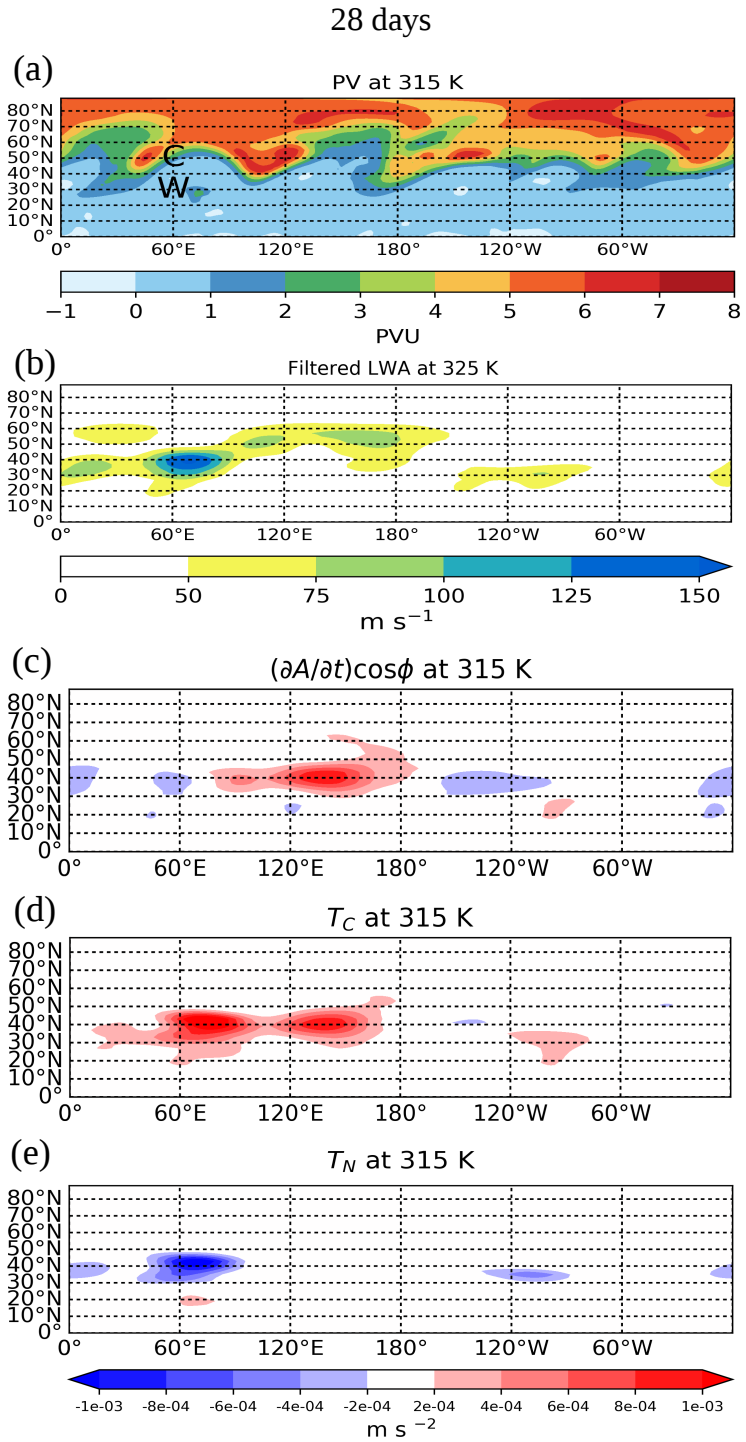

Figure 6.9: Snapshots of relevant variables on the 315 K isentrope in the PUMA simulation after 28 days of integration: (a) Potential vorticity (in PVU), (b) filtered LWA A, (c) observed tendency term $(\partial A/\partial t)\cos\phi$, (d) conservative term T_{C}, and (e) local non-conservative term T_{N}. The letters C and W in (a) mark the centres of the cold and warm anomalies, respectively, in the relaxation temperature field.

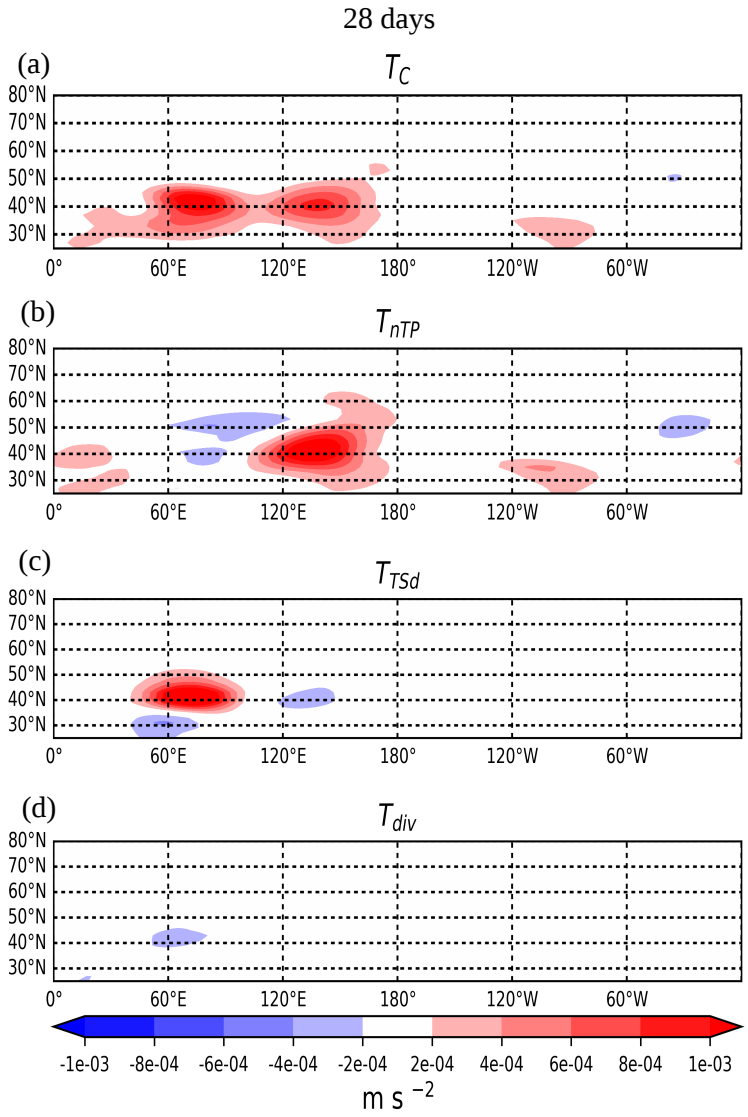

Figure 6.10: Partitioning of the conservative term in the LWA budget at day 28 on the 315-K isentrope in the PUMA-simulation. (a) Full conservative term T_{C}, (b) contribution T_{nTP}, (c) contribution T_{TSd}, (d) contribution T_{div}. Here only the area between 25 – 80° N is shown to exclude boundary effects related to the PPVI, which usually are larger close to the southern boundary (located at 11° N). Units and colour bar are the same for all plots.

the large differences between the two RWPs considered. In the region of the first RWP T_{C} is almost entirely related to its tropospheric-deep contribution T_{TSd} (Fig 6.10c), and this is consistent with the RWP growth due to baroclinic instability. On the other hand, the near-tropopause contribution T_{nTP} is slightly negative in the vicinity of the first RWP and positive further downstream (Fig 6.10b). This suggests that part of the LWA from the first RWP is transferred to the second region of waviness through near-tropopause dynamics, as one would expect from the downstream development of LWA associated with the first RWP. Lastly, the divergent contribution T_{div} (Fig. 6.10d) is very small, except in the neighbourhood of the dipole of the diabatic forcing, where its contribution is negative. We consider this to be consistent with the fact that vertical motion associated with diabatic heating and cooling maximizes close to the heating dipole. These vertical motions translate into horizontal divergence of the isentropic wind. In the present case, the effect of the divergence contribution is to reduce the overall amplitude of the first RWP. As we will see in the next section, the divergent contribution in our PUMA simulation is much weaker than in the real atmosphere, and we relate this to the lack of moist processes in our dry primitive equation model" (Ghinassi et al., 2019).

6.3 Operational weather forecast model

"We now move on and apply our diagnostic to real meteorological data analyzing the propagation of a particular RWP that occurred in April 2011. The RWP propagated from North America towards Europe, where it produced wave breaking and eventually evolved into blocking. This episode was associated with below average forecast skill in the medium range over Europe in the majority of numerical weather prediction models (Rodwell et al., 2013). Our analysis uses data from the integrated forecasting system of the European Centre for Medium Range Weather Forecasts (ECMWF). We compare the ECMWF forecasts issued on the 10th of April 2011 at 00 UTC with the respective verifying analyses to investigate the difference between the two in terms of LWA and its evolution. We retrieved 6-hourly data for both the forecasts and the analyses on pressure levels between 100-850 hPa with a grid resolution of 1 degree for the Northern

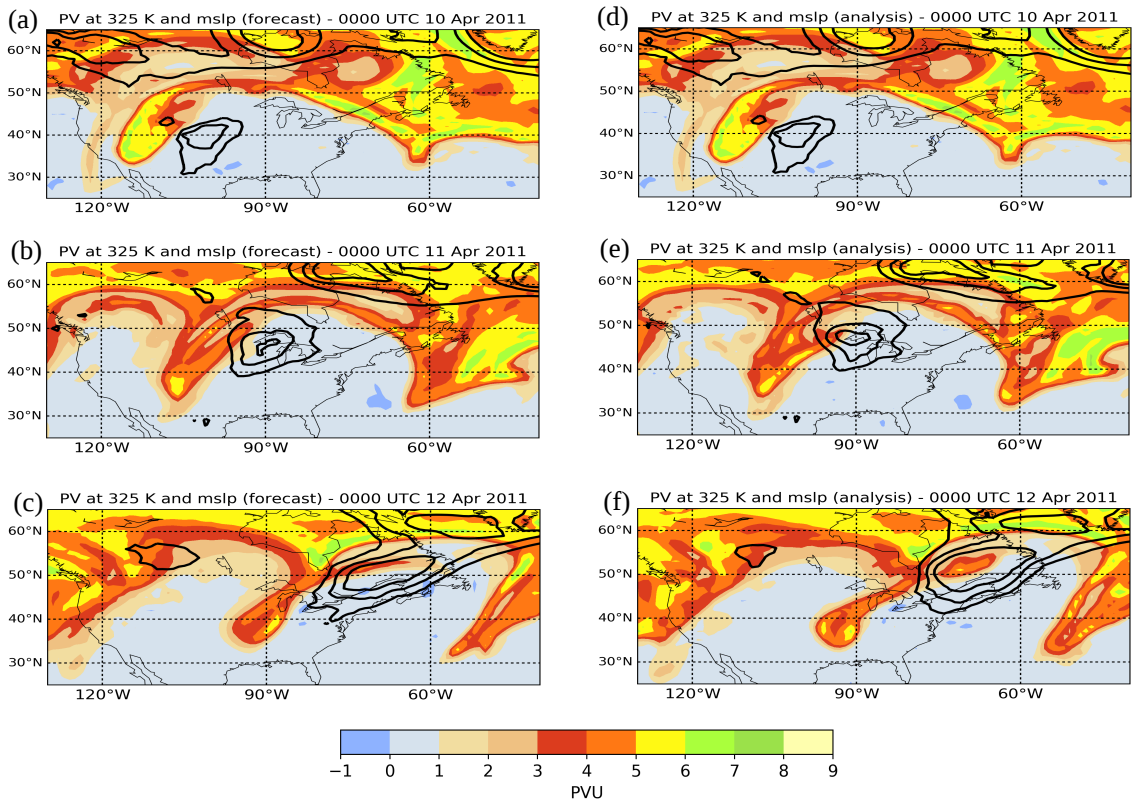

Figure 6.11: Evolution of the flow in the upper troposphere and at the surface during an episode in April 2011 in the ECMWF model forecast issued on 10 April 2011 0000 UTC (left column) and in the corresponding analyses (right column). The colour shows PV on the 325 K isentrope (in PVU) and the black contours show the 990, 995, and 1000 hPa isobars of surface pressure.

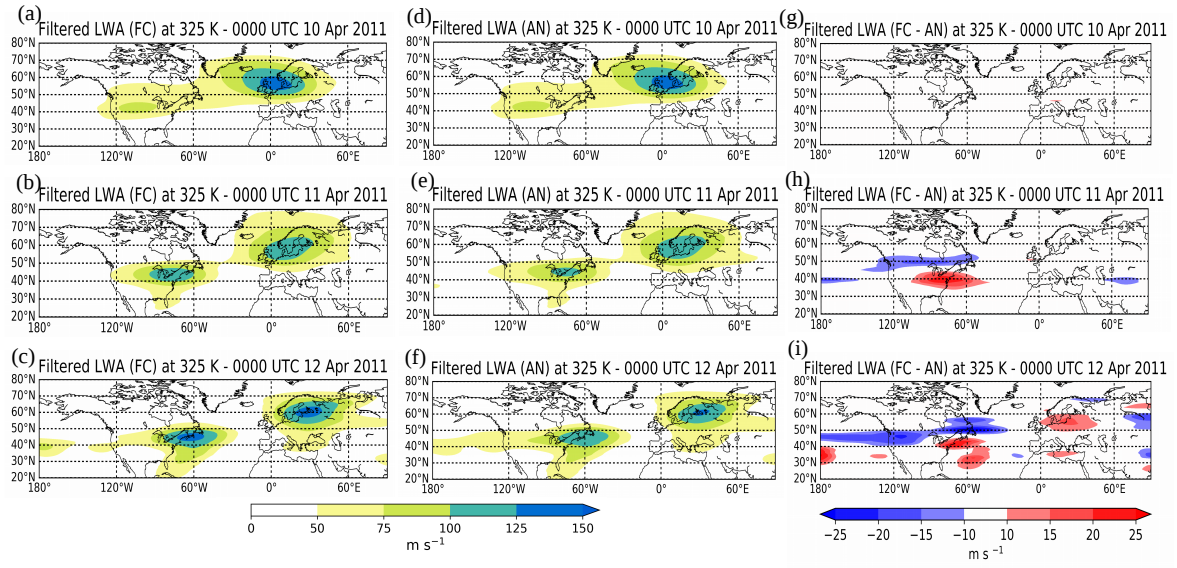

Figure 6.12: Evolution of filtered LWA on the 325 K isentrope for the same episode as shown in Fig. 6.11: ECMWF model forecast (left column), verifying analysis (middle column), and the difference (forecast minus analysis, right column), for the first 2 days into the forecast.

Hemisphere. LWA and the related budget terms (including the partitioning of the conservative term) were computed as described in chapter 3. Here, we focus on the first 48 hours of lead time. During this time a cyclone was found over North America, associated with heavy precipitation over a region spanning from the midwest towards the East Coast of the USA (Rodwell et al., 2013). We focus on this time window to see how the diabatic modification of PV associated with moist processes manifests itself in the non-conservation of LWA.

An overview over the selected episode is given in Fig. 6.11 showing a sequence of maps of upper-tropospheric PV on the 325 K and mean sea level pressure. At initial time (Fig. 6.11a) the upper level flow consisted of a trough located over the Rocky Mountains and a ridge downstream over the Great Plains of the USA. This trough-ridge couplet was part of a more extended RWP. At the surface, there was a cyclone developing immediately to the east of the upper level trough, a typical situation of baroclinic development as discussed in section 2.2 (see Fig. 2.3). Subsequently, the upper-tropospheric trough and the ridge moved eastward and became more tilted, and at the same time the surface cyclone deepened and moved in a north-eastward

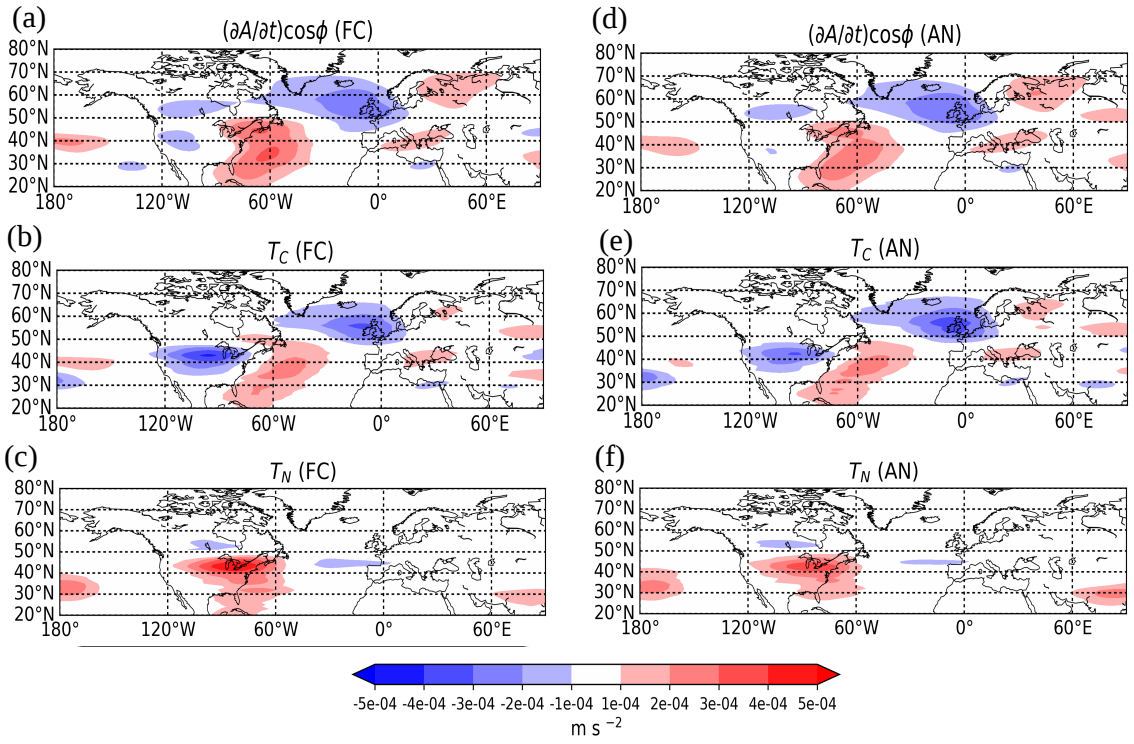

Figure 6.13: Terms of the LWA budget on the 325 K isentrope averaged between 10th and 12th of April 2011, for the ECMWF model forecast (left column) and the corresponding verifying analysis (right column). (a) and (d): Tendency term $(\partial A/\partial t)\cos\phi$, (b) and (e): conservative term T_{C}, (c) and (f): local non-conservative term T_{N}.

direction (Fig. 6.11b and c). During the first 24 hours some appreciable differences are already visible when comparing the forecast and the analysis, especially regarding the magnitude of PV in the upper tropospheric wave packet (compare the trough-ridge couplet located around 100° W in Fig. 6.11b and c). These differences in the upper level PV field become more pronounced after 48 hours lead time. In particular, the PV trough located at 90° W appears broader and less filamented in the forecast than in the verifying analysis. Another region of interest is the one located around 55° N and 75° W: here the longitudinal extent of the ridge is broader in the forecast, and higher values of PV compared to the analysis are found in the trough immediately above the dynamical tropopause (cf. Fig. 6.11c and f). The fact that these upper level differences are found right above the surface cyclone suggests that an erroneous diabatic modification of the upper level PV (associated with the physical processes within the cyclone) may have occurred in the forecast.

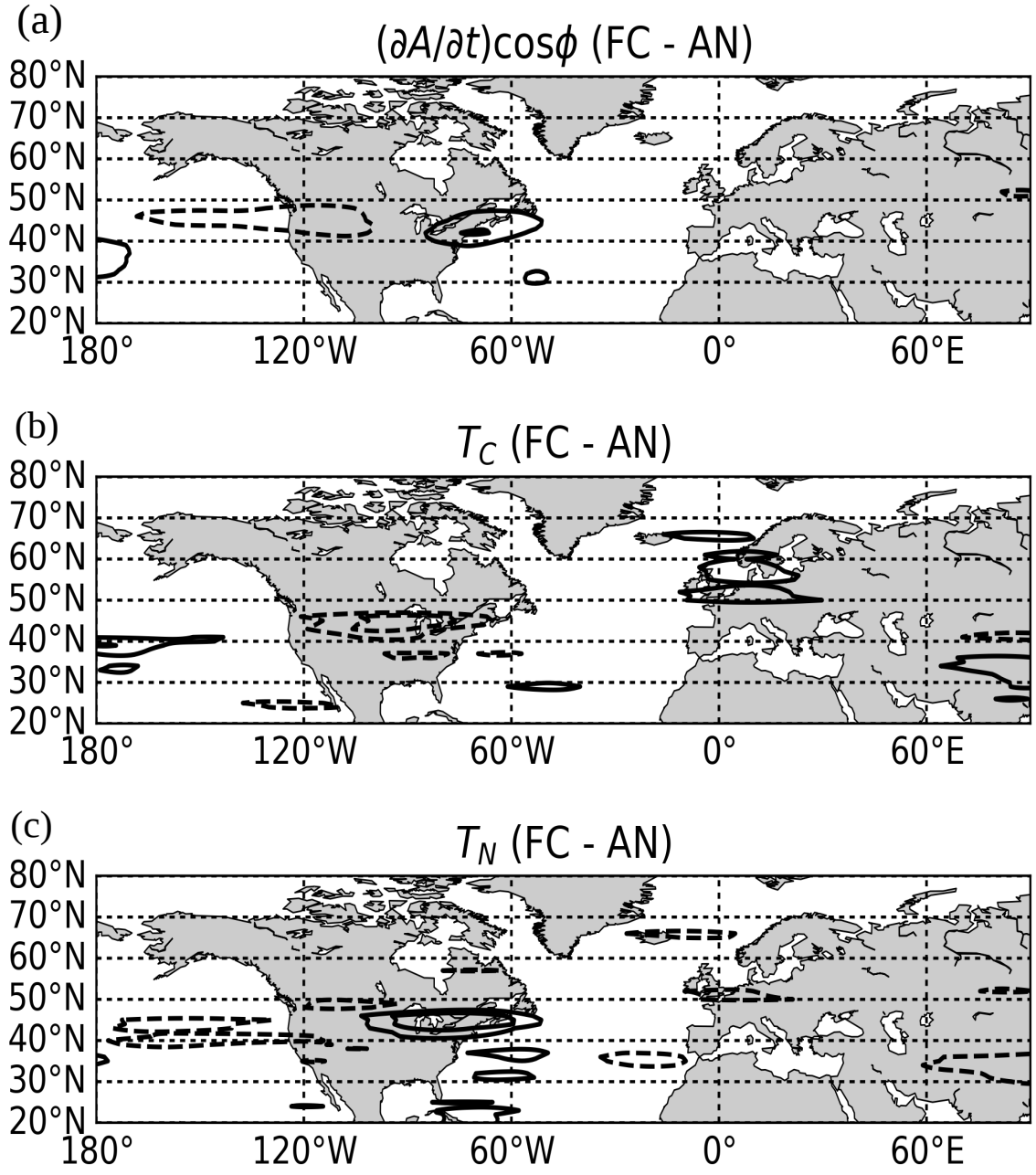

Figure 6.14: Error (forecast minus analysis) in the LWA budget terms from Fig. 6.14: (a) tendency term $(\partial A/\partial t)\cos\phi$, (b) conservative term T_{C}, (c) local non-conservative term T_{N}. Contours for all plots are between -10^{-4} m s^{-2} and 10^{-4} m s^{-2} every $5 * 10^{-5}$ m s^{-2}. The zero contour is not shown and the dashed contours represent negative values.

The same episode is shown from an LWA perspective in Fig. 6.12, which provides the forecast fields (left column), the verifying analyses (middle column), as well as the difference between the two (right column). It can be seen how LWA identifies two separate RWPs, the one from the previous figure located over the North American continent, as well as an additional one over Europe. While the latter seems to be well represented in the forecast during the first 24 hours, the RWP over North America shows an appreciable error in terms of LWA as early as 24 hours into the forecast. In particular, the RWP amplitude is too strong in the forecast immediately to the South of the Great Lakes region (Fig. 6.12h). After 48 hours, this amplitude error persists and shifts towards the North Atlantic, and this eastward shift seems to be associated with the eastward propagation of the RWP. At the same time, the forecast LWA is too weak on the northern flank of the RWP (see the band of negative LWA difference between the USA and Canada in panels (h) and (i)).

The terms from the LWA budget, averaged over the first 48 hours lead time, are shown in Fig. 6.13 both for the forecast (left column) and the verifying analysis (right column). The corresponding forecast errors, computed as the difference "forecast minus analysis", are shown in Fig. 6.14. What emerges from this comparison is that the conservative term T_{C} is more negative in the forecast, especially at the trailing edge of the wave packet (compare Fig. 6.13b and e and Fig. 6.14b). The non-conservative term T_{N} is positive in both the forecast and the analysis, which means that the overall contribution from non-conservative processes in this case was to increase the RWP amplitude. However, the magnitude of T_{N} is larger in the forecast. The net effect of the conservative and non-conservative terms corresponds to an overestimation of the forecast LWA tendency over the east coast of the USA (positive values in Fig. 6.14a).

Finally, we turn to the partitioning of T_{C} into the different contributions (Fig. 6.15). As background state for the PPVI we chose a 30 day mean centred on the 13th of April from the analysis for both the forecast and the analysis. The tropopause-near contribution T_{nTP} recovers a large part of the full conservative term T_{C} (compare Fig. 6.15a with Fig. 6.13b). The deep-troposphere contribution T_{Td} (Fig. 6.15b) is positive both in the forecast and the analysis.

This is consistent with the growth of the RWP through baroclinic instability, which

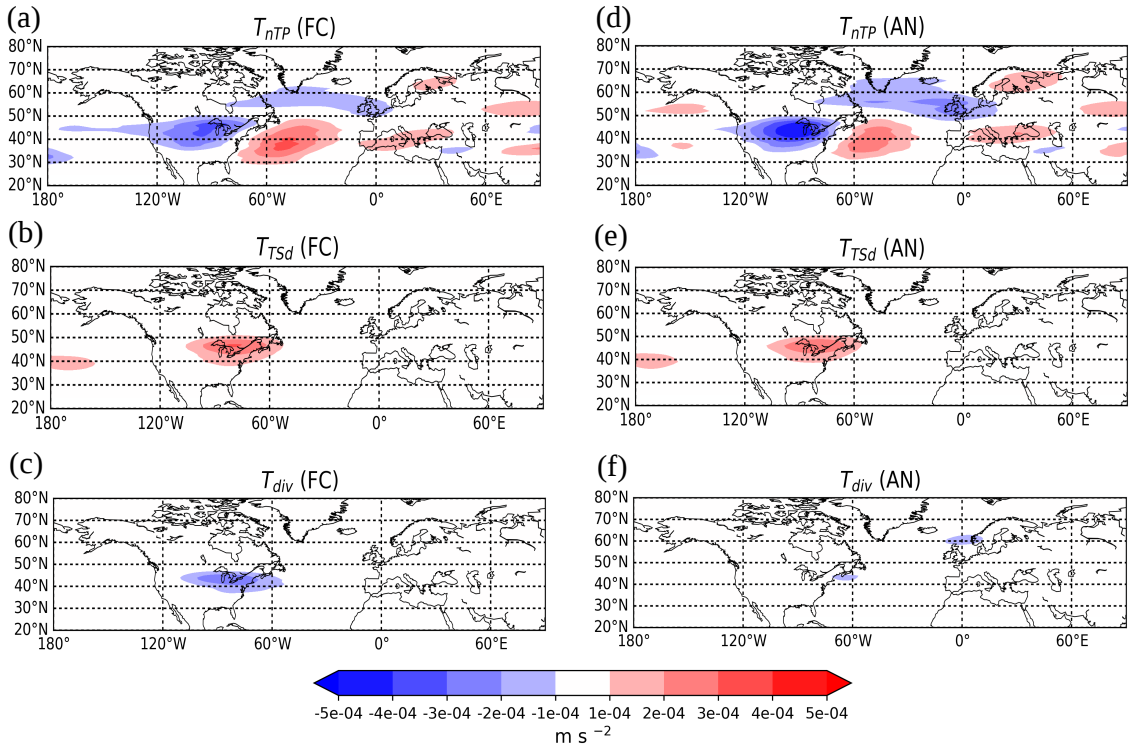

Figure 6.15: Partitioning of the conservative term T_{C} into the different wind contributions on the 325 K isentrope averaged between the 10th and 12th of April (with 6-hourly data). T_{nTP}, T_{TPd}, and T_{div} for the forecast are in panels (a), (b), (c), the same but for the analysis in panels (d), (e), (f), and their difference (forecast minus analysis) in panels (g), (h), (i). Contours for panels (g), (h), (i) are between $-2 * 10^{-4}$ m s^{-2} and $2 * 10^{-4}$ m s^{-2} every 10^{-4} m s^{-2}. The zero contour is not shown and the dashed contours represent negative values.

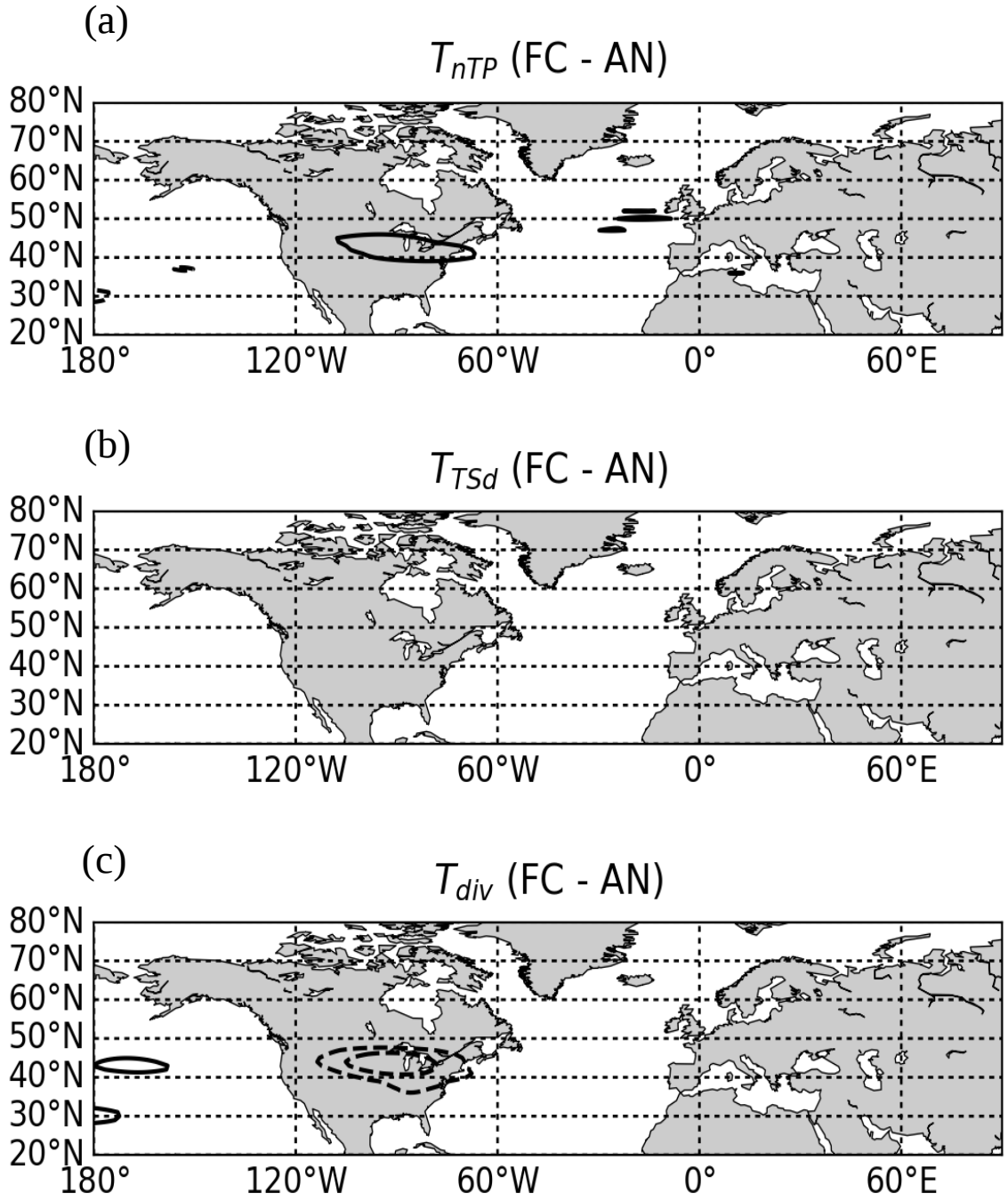

Figure 6.16: Error (forecast minus analysis) in the different contributions to the conservative term in the LWA budget corresponding to the fields displayed in Figure 6.16: (a) tropopause-near term, (b) troposphere-deep term, (c) divergent term. Contours for all plots are between $-2 * 10^{-4}$ m s^{-2} and $2 * 10^{-4}$ m s^{-2} every 10^{-4} m s^{-2}. The zero contour is not shown and the dashed contours represent negative values.

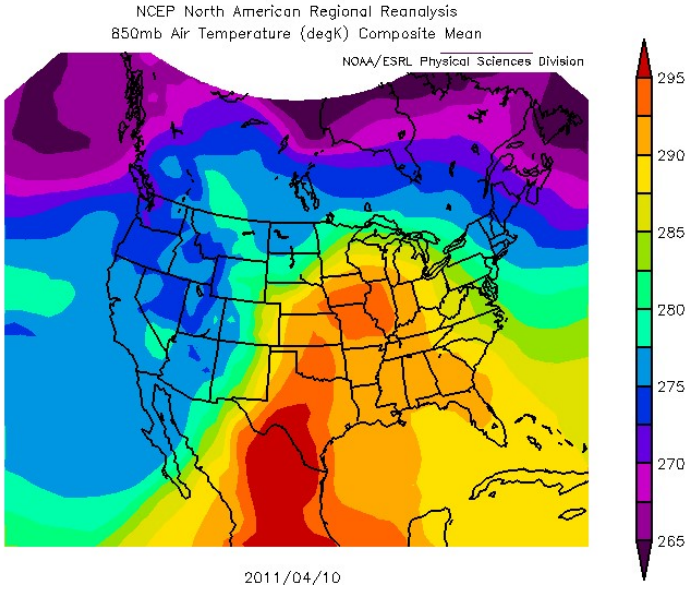

Figure 6.17: Re-analysed temperature at 850 hPa on the 10th of April over North America. Data have been retrieved and plotted using the NCEP/NCAR reanalysis portal: https://www.esrl.noaa.gov/psd/data/composites/day/.

in turn is related to a strong horizontal temperature gradient over North America during this period (see Fig. 6.17). This process seems to be well represented in the forecast (Fig. 6.16b). Interestingly, the largest error arises from the divergent contribution T_{div} (Fig. 6.16c): in the forecast this term is associated with a considerable decrease of LWA (Fig. 6.15c), much stronger than suggested by the verifying analysis (Fig. 6.15f). The negative values of T_{div} in the forecast are found in the middle of the ridge, ahead of the approaching PV trough (Fig. 6.11), similar as for the RWP examined in the PUMA simulation (Fig. 6.10d). In the present real case, however, the magnitude of the divergent wind contribution T_{div} is much larger than in the PUMA simulation due to a stronger divergent wind in the upper levels, and this is likely to be associated with moist processes below.

In summary, both the local non-conservative term T_{N} and the divergent contribution T_{div} to the conservative term T_{C} are associated with substantial errors in the forecast. Both terms are directly or indirectly related to diabatic heating happening in the mid and upper troposphere (Hoskins et al., 1985; Teubler and Riemer, 2016). Our analysis thus suggest that the origin of the RWP amplitude errror was a poor representation of diabatic processes in the forecast model. This result is consistent with the original

interpretation of Rodwell et al. (2013)" (Ghinassi et al., 2019).

Chapter 7

Summary and conclusions

In this thesis a new diagnostic to quantify the amplitude of upper tropospheric Rossby wave packets (RWPs) in terms of their pseudo-momentum has been developed. The diagnostic is based on the local finite amplitude wave activity (LWA) of Huang and Nakamura (2016), but extended to the primitive equations in isentropic coordinates framework. RWPs are identified by first computing LWA and then their amplitude is quantified by removing the phase dependence from LWA applying a zonal filter. Two filters are proposed (described in chapter 3), both based on the convolution of LWA with a Hann window. The first filter assumes a Hann window of fixed length at each latitude, in which its wavelength is set determining a dominant zonal wavenumber via a Fourier analysis of the power spectrum of the meridional wind at each latitude circle. Two main advantages of this filter are the fact that it is computationally inexpensive and the fact that commutes with the gradient operator. The latter property is of crucial importance to preserve the exactness of the conservation relation written in the flux form for filtered LWA. Although in this work we do not explicitly compute the LWA budget using the flux form of the conservation relation we decided to use this filter anyway when dealing with budgets of filtered LWA. In the second filter proposed the width of the Hann window depends also on longitude and it is determined computing a local dominant zonal wavenumber through wavelet analysis of the meridional wind. This wavelet filter performs better in removing the phase dependence from LWA especially when several wave packets with different carrier wavenumbers are found at the same latitude. We have used the wavelet filter when dealing only with the identification of RWPs.

In chapter 4 we tested our LWA diagnostic to identify RWPs in both idealized

simulations (barotropic model on the sphere) and reanalysis data. For this purpose we achieved the phase removal from LWA via the filter based on wavelets. Part of the results mentioned in section 4 have been published Ghinassi et al. (2018).

"We studied the performance of the LWA disgnostic in identifying RWPs with the aid of a barotropic model simulation in which two wave packets, initialised with different carrier wave numbers, were propagating onto a zonal jet until they decayed producing wave breaking. During our experiment we compared the LWA diagnostic with another widely used one based on the extraction of the envelope of meriodional wind Zimin et al. (2003). By the time the RWPs developed wave breaking and overturning PV contours, the envelope diagnostic showed a strong amplitude decrease, while the LWA diagnostic continued to detect the RWPs with a strong amplitude. In addition, we found differences between the two diagnostics in the location of the detected RWPs during the late stage of the evolution, with a tendency of the LWA diagnostic to focus on the vortical structures" (Ghinassi et al., 2018). During this analysis we also compared the finite amplitude LWA with its small amplitude variant, demonstrating the value of the finite amplitude nature of LWA when dealing with large amplitude wave packets. Furthermore, we demonstrated numerically the global conservation of filtered LWA, comparing it with the envelope of meridional wind. Our analysis suggests that LWA, due to its conservation property, would be particularly suitable for the tracking of RWPs.

The finite amplitude LWA flux has been used to diagnose the RWPs propagation of the eddies in the RWPs decay simulation. Results show how wave breaking was associated with the propagation of LWA towards regions of smaller PV gradient and to the convergence of the LWA flux, especially in the equatorward flank of the jet. These results are in agreement with previous works related to the propagation of RWPs in reanalysis data (Danielson et al., 2006; Wolf and Wirth, 2017). These authors however performed their analysis using the LWA flux formulation of Takaya and Nakamura (2001), which assumes that the amplitude of the waves is small and that the atmosphere is quasi-geostrophic. The finite amplitude LWA flux and its divergence, despite being tested in an idealised simulation, provided insightful information on the propagation of RWPs even during their large amplitude stage and wavebreaking initiation.

In addition, the LWA flux has been applied to an additional simulation considering the barotropic model in a forced-dissipative set-up to diagnose the propagation of planetary scale Rossby waves. In this experiment a Rossby wave train was generated through a flow in solid body rotation interacting with a pseudo-orographic forcing, until Rossby wave activity was radiated all over the globe and a stationary state was reached. The LWA flux clearly identified the horizontal propagation of the eddies during the transient phase of the wave train development and once a stationary state was reached. The results obtained are in agreement with previous work which considered the local wave activity flux in the framework of linear theory (Plumb, 1985, 1986; Takaya and Nakamura, 2001) but now are generalised including finite amplitude eddies. The LWA flux is thus of extreme value in complementing the RWPs analysis using wave activity. Unfortunately a formulation of the LWA flux in the primitive equations framework cannot be derived in a straightforward manner, due to the impossibility to write the equation for the evolution of LWA in the canonical flux form. An open question is to investigate to what extent the quasi-geostrophic formulation of the LWA flux can provide an insightful picture when applied to real atmospheric data, at least in the extratropics.

After a first test in the barotropic model, we applied our LWA diagnostic in the primitive equations framework to real atmospheric data, namely to an episode of a propagating RWP which occurred in April 2011. At the initial stage the RWP structure did not deviate consistently from a plane wave, but at a later stage the RWPs became large, produced wave breaking which eventually evolved into blocking. It turns out that during this episode the newly developed diagnostic provides a more coherent picture of a continuous progression of various RWPs than the conventional diagnostic based on the envelope of the meridional wind. The better performance of the new method in such nonlinear situation is associated with a better representation of the mature phase of RWPs with large amplitudes from LWA, as was found in the barotropic model experiment. During this analysis LWA in the primitive equations has been compared with its quasi-geostrophic variant elucidating the limits of the quasi-geostrophic approximation in identifying RWPs in the subtropics and at the tropopause region. The fact that the LWA diagnostic is able to identify RWP during the nonlinear, finite-

amplitude stage is obviously related to the fact that LWA is by design able to keep track of arbitrarily large amplitudes.

Finally, a seasonal climatology of Rossby wave activity based on filtered LWA has been computed from Era-Interim data spanning the 1979-2016 period. During the Northern Hemisphere winter and spring Rossby wave activity is mainly localised over two pronounced maxima over the Pacific and North Atlantic, where the storm tracks are found. In autumn and summer instead wave activity appears more longitudinally uniform, with the Pacific and Atlantic storm tracks connected together due to relatively high Rossby wave activity found over the North American continent. The Eastern portion of the Northern Hemisphere exhibits a weaker wave activity throughout the four seasons. During our analysis we found that the Rossby wave activity associated with transient RWPs in the Northern Hemisphere storm tracks was found more to the east when compared to other works in which the latter was identified through the envelope of meridional wind (Souders et al., 2014). This is presumably related to the ability of filtered LWA to identify Rossby wave breaking (which usually happens in the downstream region of storm tracks), in contrast to the envelope of the meridional wind, which generally produces a weak amplitude in such nonlinear conditions. The Rossby wave activity analysis of the Southern Hemisphere showed a more uniformly, longitudinally distributed band of wave activity in the midlatitudes. Concerning the latitudinal position of the storm tracks, in both hemispheres the regions of high LWA are found poleward compared to other metrics (envelope, Eddy Kinetic Energy) and this is likely to be a nonlocal effect due to vortices of high (low) PV associated with a more nortward (southward) latitude.

In chapter 5 we presented an application of the LWA diagnostic to an upscale error growth experiment. The results presented in this section appear in Baumgart et al. (2019). "The experiment consisted in investigating global ICON simulations of real cases employing the stochastic Plant-Craig convection scheme to simulate how the uncertainty associated to the convective scale project onto the planetary scale. The use of a stochastic convection scheme enables us to represent convective uncertainty and its upscale propagation at relatively low computational cost (Selz and Craig, 2015).

Thereby, it has been possible to simulate 12 cases each consisting of a 5 member ensemble, in which the only difference between the ensemble members lies in the random seed of the stochastic convection scheme" Baumgart et al. (2019).

The LWA diagnostic was used to extract the Rossby wave envelope, therefore proving a metric for the phase averaged waviness of the large scale flow. This allowed to extend our investigation of the upscale error growth to the planetary scale, which would not have been possible using the PV based diagnostic described in Baumgart et al. (2018), since the latter reaches saturation at the synoptic scale. The PV and LWA diagnostics allowed us to identify the regions in which the error grows faster in magnitude and spatial scale. These regions were located mainly in the Western Hemisphere, in particular over the East Pacific, North America and North Atlantic. Those are regions associated with high Rossby wave activity in the climatology. "The LWA diagnostic indicates that a fourth stage of the error growth exists between about day 14.5 and 18 when the predictability time in the PV diagnostic is reached, but when there is still some predictability left in the Rossby wave envelope. This stage is characterised by error growth from the synoptic scale of individual Rossby wave troughs and ridges up to the planetary scale of the wave envelope.

The results of our PV and LWA diagnostic confirm the existence of a multi-stage behaviour of upscale error growth as observed in previous studies (e.g., Zhang et al., 2007; Selz and Craig, 2015; Judt, 2018). Furthermore the LWA diagnostics suggests an additional fourth stage of planetary-scale error growth that was missing in the conceptual model of Zhang et al. (2007)" Baumgart et al. (2019).

In chapter 6 we extended the LWA diagnostics deriving a budget equation for filtered LWA (see sections 2.5.1 and 2.5.3) in order to quantify the processes associated with the growth and decay of the amplitude of upper tropospheric RWPs. The results of chapter 6 have been submitted in Ghinassi et al. (2019). "We applied this technique to a hierarchy of models, namely a barotropic model, a dry primitive equation model, and a state-of-the-art weather forecast model. The budget term representing conservative dynamics was further partitioned into contributions from the near-tropopause wind, the tropospheric-deep wind, and the divergent wind close to the tropopause, following

previous work by Teubler and Riemer (2016) and Baumgart et al. (2018).

Our diagnostic was first applied to an idealised simulation using the barotropic model on the sphere with local pseudo-orographic forcing as a source for RWPs. The simplicity of the model and its configuration allowed us to anticipate the behaviour of the individual terms of the LWA budget, and we found a very good correspondence between these expectations and our model results. In particular, as expected in the barotropic model, the orographic forcing and the dissipation were reflected in the non-conservative term T_{N} of the LWA budget. Importantly, these sources and sinks showed a pronounced zonal asymmetry, which demonstrates the added value of LWA compared to a zonally averaged diagnostic.

We then applied our diagnostic to simulations of a dry primitive equation model (PUMA, (Frisius et al., 1998; Fraedrich et al., 2005)). A forced-dissipative model configuration was used with locally enhanced baroclinicity in order to generate an idealised storm-track, in which RWPs grow due to baroclinic instability. A key difference with respect to the foregoing barotropic simulation is the fact that in a three-dimensional model RWPs and the associated LWA may also propagate in the vertical. It follows that on a given upper tropospheric isentrope the vertical propagation of a RWP may appear as net increase or decrease of LWA on that isentrope, although this process is clearly associated with conservative dynamics. The dynamics of this simulated baroclinic wave packets clearly appeared in our LWA budget: in the upper troposphere Rossby we found that wave activity is continuously excited via baroclinic instability, which at the same time is balanced by the dissipation from non-conservative processes (linear relaxation and hyperdiffusion in our PUMA experiment). It was shown that the formulated LWA diagnostic is, indeed, able to identify these local conservative and non-conservative sources and sinks of LWA and their impact on the RWPs amplitude evolution.

Finally, the diagnostic framework was applied to an observed episode simulated by the operational model of the ECMWF, namely the April 2011 case (the same case analysed section 4 but with reanalysis data). We applied our LWA budget diagnostic to both the forecast and the analysis and obtained insight into error sources regarding the RWP dynamics by comparing the two. Differences in RWP amplitude during early lead

times were found to be related to non-conservative processes in the upper troposphere and with upper tropospheric divergent flow, the latter likely to be associated with diabatic heating in the mid-troposphere Hoskins et al. (1985); Grams et al. (2011). These findings are consistent with the study of Rodwell et al. (2013), who linked the forecast error in this particular RWP to a misrepresentation of diabatic processes over the American midwest associated with a mesoscale convective system, which was present at the time of the forecast initialization. At the same time we demonstrated that the origin of the error in the RWP occurred not only during the forecast initialization but persisted also at some time later into the forecast. Our results are also consistent with the analysis performed by Baumgart et al. (2018, 2019), who linked the early stage of error growth to the diabatic modification of PV. A similar scenario was also found by Martinez-Alvarado et al. (2016), who linked an error in a ridge embedded in a RWP to the misrepresentation of both the diabatic modification of PV and the divergent outflow in the upper troposphere.

Future work has to show to what extent the results from our case study, namely the ability of diabatic processes to strongly affect the RWPs amplitude, are systematic and can be generalized to the majority of the cases of interest.

A key advantage of LWA in comparison with its linear variant is that all terms can be computed from any PV field without the danger of singularities. On the other hand, obviously there are some caveats with our proposed method. It is important to remark that the partly Lagrangian nature of LWA can sometimes prevent a straightforward interpretation. For instance, in case of a pronounced and longitudinally extended reversal of the meridional PV gradient, high (low) PV values at a given latitude may become associated with high LWA values at a more poleward (equatorward) latitude in the Northern Hemisphere. If this is the case, large values of LWA or its budget may be associated with meteorological phenomena at a different latitude " (Ghinassi et al., 2019). The choice of a suitable isentrope that avoids such longitudinally extended PV gradient reversals is thus desirable both for the identification of RWPs and the description of the evolution of their amplitude to avoid such intrinsic non-local effect of LWA.

To conclude, the main properties of the here presented LWA diagnostic are sum-

marised in the following:

- in terms of the identification of RWPs the LWA diagnostic is in fair agreement with the envelope of meridional wind of Zimin et al. (2003) in case of small amplitude wave packets. However, unlike the envelope of meridional wind, the LWA diagnostics is able to identify RWPs even when their amplitude becomes large an they exhibit a highly non-linear structure, due to the finite amplitude nature of LWA.

- in the analysis of the RWPs dynamics, the use of LWA is particularly convenient, since the LWA budget clearly distinguishes between conservative and non-conservative processes affecting the evolution of the RWP amplitude. In addition, the finite amplitude nature of LWA guarantees its computation from any PV field and the possibility to quantify nonconservative sources and sinks of LWA as a residual from the budget, unlike its small amplitude variant.

- the LWA diagnostics provides information about the evolution of the amplitude of the whole wave packet rather than its individual phases. This places the LWA diagnostics at an intermediate spatial scale between a PV based approach to describe the evolution of individual troughs and ridges and the formulation of wave activity for the zonally averaged flow.

As author of this thesis I hope that the material and the results presented in this work can be used in the future to gain further insight on the dynamics and predictability of RWPs.

Appendices

Appendix A

Local wavenumber through wavelet analysis[1]

Here we describe the algorithm realised by my colleague Georgios Fragkoulidis to determine a local (in space) zonal wavenumber. The analysis is based on the wavelet transform of the meridional wind v for each given latitude circle on the selected isentrope. "The following steps are performed.

(i) The basis function for our wavelet analysis is the complex-valued Morlet wavelet as a function of longitude,

$$\Psi_0(\lambda) = (\pi\sigma_\lambda^2)^{-\frac{1}{4}}\, e^{is_0\lambda}\, e^{-\frac{\lambda^2}{2\sigma_\lambda^2}}\,, \tag{A.1}$$

where s_0 is the center wavenumber and σ_λ is the shape parameter (Yi and Shu, 2012). This wavelet is suitable for our purposes, partly because its real part resembles the RWPs that we are trying to analyze. The parameters s_0 and σ_λ were taken to be 6 and 0.7; this choice guarantees important properties of the Morlet wavelet, namely its admissibility (Farge, 1992) and a good compromise between wavenumber and space localization.

(ii) The meridional wind field is filtered by applying a Fourier series expansion in longitude and discarding zonal wavenumbers greater than 20.

(iii) The continuous wavelet transform in the zonal direction yields the following

[1]From Ghinassi et al. (2018).

wavelet coefficients,

$$W_n(L) = \sum_{n'=0}^{N-1} v_{n'} \Psi_0^* \left[\frac{(n'-n)\Delta\lambda}{L} \right] , \tag{A.2}$$

where L denotes the scale, n $(= 0, 1, \ldots N-1)$ numbers the grid points in the zonal direction, v_n is the meridional wind at grid point n, $\Delta\lambda$ is the grid spacing in the zonal direction, and the asterisk denotes complex conjugation (Torrence and Compo, 1998). At every grid point, $W_n(L)$ is evaluated for various values of the scale L, which effectively probe the different spatial scales in the neighborhood of this grid point. Note that edge effects are not an issue in our application since we are dealing with a periodic domain.

For an efficient computation, we actually perform the convolution on the right hand side of (A.2) in Fourier space. The wavelet coefficients can, thus, be written as

$$W_n(L) = \sum_{s=0}^{N-1} \hat{v}_s \hat{\Psi}^*(Ls) e^{isn\Delta\lambda} , \tag{A.3}$$

where s is the zonal wavenumber, $\hat{v}_s$ represents the discrete Fourier transform of v_n, and

$$\hat{\Psi}(Ls) \coloneqq C\ \hat{\Psi}_0(Ls) = C\ (4\pi\sigma_\lambda^2)^{\frac{1}{4}}\ e^{\frac{-\sigma_\lambda^2 (Ls - s_0)^2}{2}} \tag{A.4}$$

is the Fourier transform of the Morlet wavelet (Yi and Shu, 2012), multiplied by the normalization factor $C = (2\pi L/\Delta\lambda)^{\frac{1}{2}}$ to achieve unit energy at each scale (Torrence and Compo, 1998).

(iv) The two-dimensional *wavelet power spectrum* is then obtained by computing $|W_n(L)|^2$ at every grid point for a finite number of scales ($L_m = L_0\, 2^{m\delta_m}$, $m = 0, 1, \ldots 300$, with $L_0 = 0.2$ being the smallest resolvable scale and $\delta_m = 0.02$ the scale resolution). Following Liu et al. (2007), each value of the power spectrum is then divided by its respective scale in order to partially account for the dispersion (in scale) bias at small scales.

(v) The above set of scales is converted to the associated zonal wavenumbers through $s_m = 2\pi/(fL_m)$ where $f = 4\pi/\left(s_0 + \sqrt{2 + s_0^2}\right)$ (Torrence and Compo, 1998). At each grid point n of the resulting $|W_n(s_m)|^2$ spectrum, the wavenumber that

corresponds to the maximum power constitutes the *local dominant wavenumber* s_d of the respective longitude λ.

(vi) Steps (iii)–(v) are repeated for every latitude, eventually providing the two-dimensional field of local dominant wavenumber $s_d(\lambda, \phi)$.

(vii) Finally, we apply a filter to $s_d(\lambda, \phi)$ by convolution with a Hann-window (Harris, 1978) of 21° (full width at half maximum) in the zonal direction, followed by a 7° Hann-window in the meridional direction.

As an example, we show in Fig. A.1 the field of the meridional wind and the associated locally dominant wavenumber for the initial state of our barotropic simulation. Remember that the two wave packets were initialized with carrier wavenumbers 6 and 9, respectively. Apparently, our algorithm does a good job in reproducing these wavenumbers in the center of the respective wave packets, with a smooth transition between them. The performance for a real flow situation corresponding to the analysis from Fig. 4.10 is shown in Fig. A.2. This field is more complex, but again there seems to be a reasonable compromise between local detail and overall representativeness in the field $s_d(\lambda, \phi)$" (Ghinassi et al., 2018).

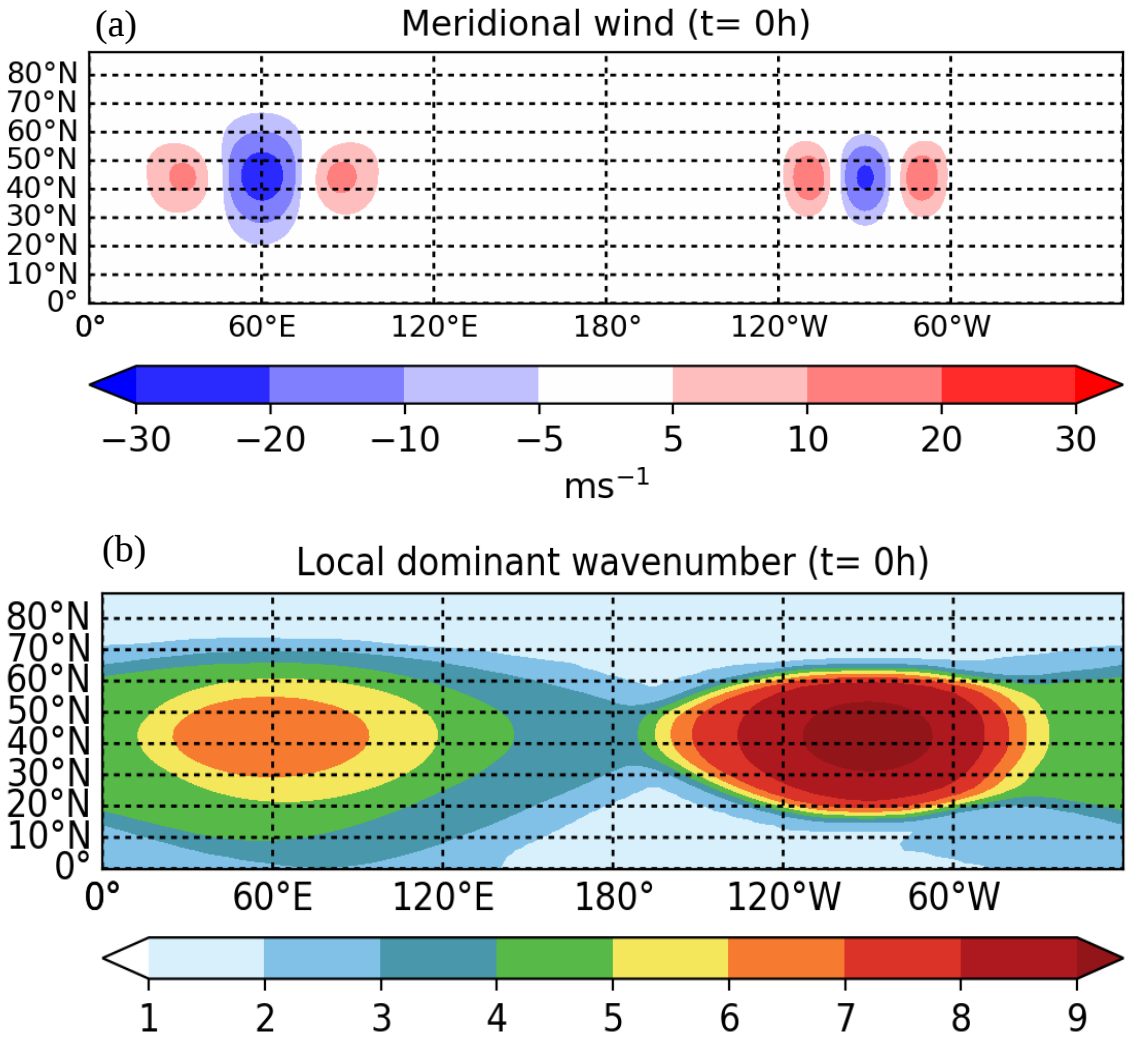

Figure A.1: Initial state of the barotropic model simulation: (a) meridional wind v (color shading, in m s^{-1}) and (b) local dominant wavenumber (color shading, dimensionless) from wavelet analysis. From Ghinassi et al. (2018) © Copyright 2018 American Meteorological Society (AMS). Used with permission.

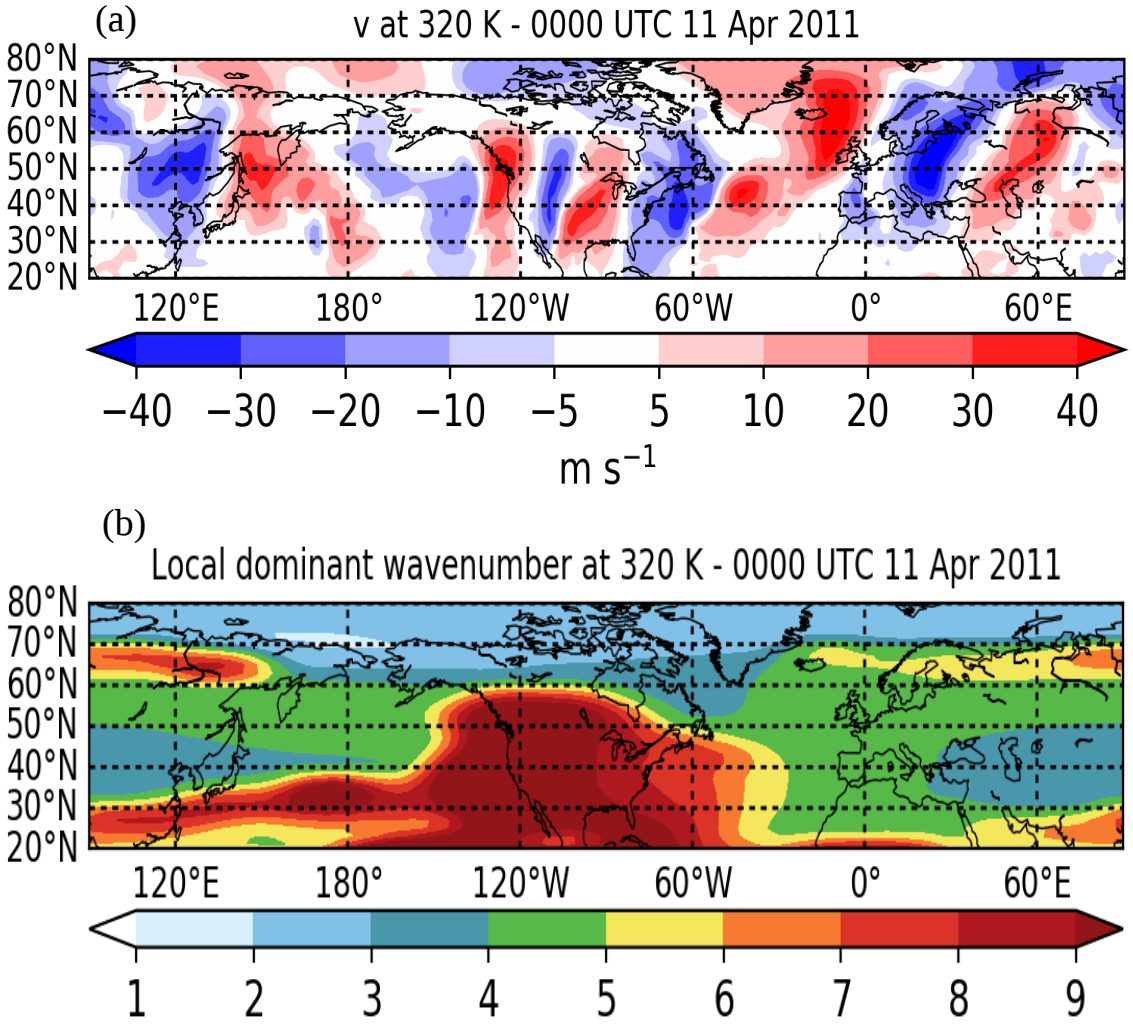

Figure A.2: Same analysis as in Fig. A.1, but here for the flow on the 320 K isentrope on 0000 UTC 11 April 2011. From Ghinassi et al. (2018) © Copyright 2018 American Meteorological Society (AMS). Used with permission.

Appendix B

Relaxation temperature profile in PUMA

"The zonally symmetric part $T_R(\phi, \sigma_{\text{lev}})$ of the relaxation temperature field is equal to the one of Held and Suarez (1994), namely

$$T_R(\sigma_{\text{lev}}, \phi,) = \max\Big\{T_{\text{tp}}, \Big[T_{\text{srf}} - (\Delta T_R)_{EP} \sin\phi^2 - (\Delta\theta)_{\text{z}} \ln\sigma_{\text{lev}} \cos\phi^2\Big]\sigma_{\text{lev}}^{\kappa}\Big\}\,, \tag{B.1}$$

where $\sigma_{\text{lev}} = p/p_s$ is the model vertical coordinate (with $p_s = 1000$ hPa), $\kappa = R/c_p = 2/7$, $R = 287$ J kg^{-1} K^{-1} is the gas constant for dry air, $T_{\text{tp}} = 200$ K is the temperature at the tropopause, $T_{\text{srf}} = 315$ K, and $(\Delta T_R)_{\text{EP}} = 50$ K is the temperature difference between the equator and the poles and $(\Delta\theta)_{\text{z}} = 10$ K.

A cold and a warm anomaly are added to $T_{\text{R}}(\phi, \sigma_{\text{lev}})$, such that the new field $\widetilde{T_{\text{R}}}(\phi, \sigma_{\text{lev}})$ becomes:

$$\begin{aligned}\widetilde{T_{\text{R}}}(\sigma_{\text{lev}}, \phi, \lambda) = T_R(\sigma_{\text{lev}}, \phi) + f(\sigma_{\text{lev}})\Big[T_R(\sigma_{\text{lev}}, \phi) + \\ - (\Delta T)_{\text{dip}} \sum_{j=1}^{2} (-1)^j \exp(-d_{\lambda j}\cos^2\phi(\lambda - \lambda_j)^2 - \\ d_{\phi j}(\phi - \phi_j)^2)\Big]\end{aligned} \tag{B.2}$$

where $(\Delta T)_{\text{dip}}$ is the difference between the warm ($j = 1$) and cold ($j = 2$) anomaly, which is set to $(\Delta T)_{\text{dip}} = 40\ K$. The function $f(\sigma_{\text{lev}})$ provides weighting of the temperature anomalies along the vertical such that they decrease from their surface value

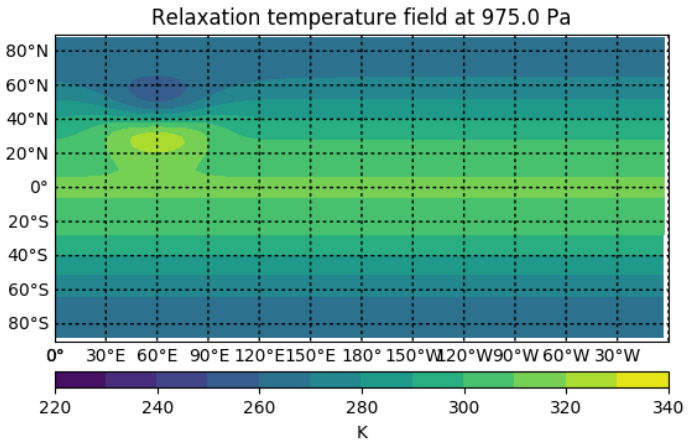

Figure B.1: Relaxation temperature $\tilde{T}_{\mathrm{R}}$ on the lowest model level for the PUMA model.

to zero in the upper troposphere and above:

$$f(\sigma_{\mathrm{lev}}) = \begin{cases} \sin\left[\frac{\pi}{2}\left(\frac{\sigma_{\mathrm{lev}}-0.4}{1-0.4}\right)\right], & \text{if } \sigma_{\mathrm{lev}} \geq 0.4, \\ 0, & \text{if } \sigma_{\mathrm{lev}} < 0.4. \end{cases} \tag{B.3}$$

Values for parameters of (B.2) are given in table C1, and the modified relaxation temperature in the lowest model level is shown in Figure B.1 " (Ghinassi et al., 2019).

parameter	value
λ_1	60
λ_2	60
ϕ_1	32.1
ϕ_2	51.6
$d_{\lambda 1}$ for $\lambda \geq \lambda_1$	20 rad^{-2}
$d_{\lambda 1}$ for $\lambda < \lambda_1$	15 rad^{-2}
$d_{\lambda 2}$ for $\lambda \geq \lambda_2$	12 rad^{-2}
$d_{\lambda 2}$ for $\lambda < \lambda_2$	5 rad^{-2}
$d_{\phi 1}$ for $\phi \geq \phi_1$	20 rad^{-2}
$d_{\phi 1}$ for $\phi < \phi_1$	10 rad^{-2}
$d_{\phi 2}$ for $\phi \geq \phi_2$	9 rad^{-2}
$d_{\phi 2}$ for $\phi < \phi_2$	5 rad^{-2}

Table B.1: Parameters in equation B.2.

References

Ambaum, M. H. P., and L. Novak, 2014: A nonlinear oscillator describing storm track variability. *Quarterly Journal of the Royal Meteorological Society*, **140 (685)**, 2680–2684, doi:10.1002/qj.2352. 71, 98

Andrews, D., and M. E. Mcintyre, 1976: Planetary waves in horizontal and vertical shear: The generalized eliassen-palm relation and the mean zonal acceleration. *Journal of the Atmospheric Sciences*, **33 (11)**, 2031–2048, doi:10.1175/1520-0469(1976)033⟨2031:PWIHAV⟩2.0.CO;2. 2, 3, 18, 21

Andrews, D. G., J. R. Holton, and C. B. Leovy, 1987: *Middle Atmosphere Dynamics*. Academic Press, 489 pp. 8, 20, 21, 34, 37, 38

Andrews, D. G., and M. E. McIntyre, 1978: An exact theory of nonlinear waves on a Lagrangian-mean flow. *jfm*, **89**, 609–646, doi:10.1017/S0022112078002773. 2, 17, 21, 23

Baumgart, M., P. Ghinassi, V. Wirth, T. Selz, G. C. Craig, and M. Riemer, 2019: Quantitative view on the processes governing the upscale error growth up to the planetary scale using a stochastic convection scheme. *Mon. Wea. Rev*, **147 (5)**, 1713–1731, doi:10.1175/MWR-D-18-0292.1. 2, 75, 76, 77, 79, 80, 81, 82, 83, 84, 85, 117, 118, 120

Baumgart, M., M. Riemer, V. Wirth, F. Teubler, and S. T. K. Lang, 2018: Potential vorticity dynamics of forecast errors: A quantitative case study. *Monthly Weather Review*, **146 (5)**, 1405–1425, doi:10.1175/MWR-D-17-0196.1. 5, 45, 118, 119, 120

Bretherton, F. P., 1966: Baroclinic instability and the short wavelength cut-off in terms of potential vorticity. *Quart. Journ. Roy. Met. Soc.*, **92**, 335–345. 17

Buehler, O., 2009: *Waves and mean flows*. Cambridge University Press, 341 pp. 16

Butchart, N., and E. E. Remsberg, 1986: The area of the stratospheric polar vortex as a diagnostic for tracer transport on an isentropic surface. *Journal of the Atmospheric Sciences*, **43 (13)**, 1319–1339, doi:10.1175/1520-0469(1986)043⟨1319:TAOTSP⟩2.0.CO;2. 24

Chagnon, J. M., S. L. Gray, and J. Methven, 2013: Diabatic processes modifying potential vorticity in a north atlantic cyclone. *Quart. J. Roy. Meteor. Soc.*, **139**, 1270–1282. 5

Chang, E. K. M., 2001: The structure of baroclinic wave packets. *Journal of the Atmospheric Sciences*, **58 (13)**, 1694–1713. 16, 22

Chang, E. K. M., 2005a: The impact of wave packets propagating across asia on pacific cyclone development. *Monthly Weather Review*, **133 (7)**, 1998–2015, doi:10.1175/MWR2953.1. 16, 22

Chang, E. K. M., 2005b: The role of wave packets in wave-mean-flow interactions during southern hemisphere summer. **62**, 2467–2483, doi:10.1175/JAS3491.1. 2

Chang, E. K. M., S. Lee, and K. L. Swanson, 2002: Storm track dynamics. *Journal of Climate*, **15 (16)**, 2163–2183, doi:10.1175/1520-0442(2002)015⟨02163:STD⟩2.0.CO;2. 71

Chang, E. K. M., and I. Orlanski, 1993: On the dynamics of a storm track. *Journ. Atmos. Sci.*, **50**, 999–1015, doi:10.1175/1520-0469(1993)050⟨0999:OTDOAS⟩2.0.CO;2. 2, 14, 16, 92

Charney, J. G., 1947: The dynamics of long waves in a baroclinic westerly current. *Journal of Meteorology*, **4 (5)**, 136–162. 14

Charney, J. G., and P. G. Drazin, 1961: Propagation of planetary-scale disturbances from the lower into the upper atmosphere. *Journal of Geophysical Research*, **66 (1)**, 83–109. 1, 17, 18

Charney, J. G., and M. E. Stern, 1962: On the stability of internal baroclinic jets in a rotating atmosphere. **19**, 159–172. 17

Danielson, R. E., J. R. Gyakum, and D. N. Straub, 2006: A case study of downstream baroclinic development over the north pacific ocean. part ii: Diagnoses of eddy energy and wave activity. *Monthly Weather Review*, **134 (5)**, 1549–1567, doi:10.1175/MWR3173.1. 115

Davis, C. A., 1992: Piecewise potential vorticity inversion. *Journal of the Atmospheric Sciences*, **49 (16)**, 1397–1411, doi:10.1175/1520-0469(1992)049⟨1397:PPVI⟩2.0.CO;2. 29, 45

Dee, D., and Coauthors, 2011: The ERA-Interim reanalysis: Configuration and performance of the data assimilation system. *Quarterly Journal of the Royal Meteorological Society*, **137 (656)**, 553–597, doi:10.1002/qj.828. 62

Eady, E. T., 1949: Long waves and cyclone waves. *Tellus*, **1 (3)**, 33–52, doi:10.1111/j.2153-3490.1949.tb01265.x. 14

Edmon, H. J., B. J. Hoskins, and M. E. McIntyre, 1980: Eliassen-palm cross sections for the troposphere. *Journal of the Atmospheric Sciences*, **37 (12)**, 2600–2616, doi:10.1175/1520-0469(1980)037⟨2600:EPCSFT⟩2.0.CO;2. 2, 22

Ertel, H., 1942: Ein neuer hydrodynamischer Wirbelsatz. *Met. Z.*, **59**, 277–281. 4, 29

Farge, M., 1992: Wavelet transforms and their applications to turbulence. *Annual Review of Fluid Mechanics*, **24 (1)**, 395–458, doi:10.1146/annurev.fl.24.010192.002143. 123

Fraedrich, K., E. Kirk, U. Luksch, and F. Lunkeit, 2005: The portable university model of the atmosphere (puma): Storm track dynamics and low-frequency variability. *Meteorologische Zeitschrift*, **14 (6)**, 735–745. 92, 119

Fragkoulidis, V., G. and, P. Bossmann, and A. Fink, 2018: Linking northern hemisphere temperature extremes to rossby wave packets. *Quarterly Journal of the Royal Meteorological Society*, doi:10.1002/qj.3228, in press. 2

Frisius, T., F. Lunkeit, K. Fraedrich, and I. N. James, 1998: Storm-track organization and variability in a simplified atmospheric global circulation model. *Quarterly Journal of the Royal Meteorological Society*, **124 (548)**, 1019–1043, doi: 10.1002/qj.49712454802. 92, 119

Ghinassi, P., M. Baunmgat, F. Teubler, M. Riemer, and V. Wirth, 2019: Local finite-amplitude wave activity as a diagnostic for rossby wave packets. *Journal of the Atmospheric Sciences*. 2, 4, 5, 7, 31, 33, 36, 38, 39, 42, 43, 46, 86, 87, 92, 93, 104, 113, 118, 120, 129

Ghinassi, P., G. Fragkoulidis, and V. Wirth, 2018: Local finite-amplitude wave activity as a diagnostic for rossby wave packets. *Monthly Weather Review*, **146**, 4099–4114, doi:10.1175/MWR-D-18-0068.1. 1, 2, 7, 23, 30, 31, 32, 36, 39, 41, 42, 44, 47, 48, 49, 53, 54, 62, 63, 66, 68, 69, 115, 123, 125, 126, 127

Grams, C. M., and Coauthors, 2011: The key role of diabatic processes in modifying the upper-tropospheric wave guide: a north atlantic case-study. *Quarterly Journal of the Royal Meteorological Society*, **137 (661)**, 2174–2193, doi:10.1002/qj.891. 120

Gray, S. L., C. M. Dunning, J. Methven, G. Masato, and J. M. Chagnon, 2014: Systematic model forecast error in rossby wave structure. *Geophysical Research Letters*, **41 (8)**, 2979–2987, doi:10.1002/2014GL059282. 2

Grazzini, F., and G. van der Grijn, 2002: Central European floods during summer 2002. *ECMWF Newsletter*, **96**, 18–28. 2

Grazzini, F., and F. Vitart, 2015: Atmospheric predictability and rossby wave packets. *Quarterly Journal of the Royal Meteorological Society*, **141 (692)**, 2793–2802, doi: 10.1002/qj.2564. 2, 71

Harris, F. J., 1978: On the use of windows for harmonic analysis with the discrete fourier transform. *Proceedings of the IEEE*, **66 (1)**, 51–83, doi:10.1109/PROC.1978.10837. 43, 44, 125

Harvey, B., J. Methven, and M. H. P. Ambaum, 2018: An adiabatic mechanism for the

reduction of jet meander amplitude by potential vorticity filamentation. *Journal of the Atmospheric Sciences*, **75 (12)**, 4091–4106, doi:10.1175/JAS-D-18-0136.1. 2

Held, I. M., 1983: Stationary and quasi-stationary eddies in the extratropical troposphere: Theory. Citeseer. 88

Held, I. M., and P. J. Phillips, 1987: Linear and nonlinear barotropic decay on the sphere. *Journal of the atmospheric sciences*, **44 (1)**, 200–207, doi:10.1175/1520-0469(1987)044⟨0200:LANBDO⟩2.0.CO;2. 19, 48

Held, I. M., and M. J. Suarez, 1994: A proposal for the intercomparison of the dynamical cores of atmospheric general circulation models. *Bulletin of the American Meteorological Society*, **75 (10)**, 1825–1830, doi:10.1175/1520-0477(1994)075⟨1825:APFTIO⟩2.0.CO;2. 92, 128

Holton, J. R., 2004: *Introduction to Dynamic Meteorology*. 4th ed., Elsevier, 535 pp. 2, 9

Hoskins, B. J., 1991: Towards a PV-θ view of the general circulation. *Tellus*, **43 AB**, 27–35, doi:10.1034/j.1600-0870.1991.t01-3-00005.x. 1

Hoskins, B. J., and I. N. James, 2014: *Fluid Dynamics of the Midlatitude Atmosphere*. Wiley Blackwell. 2, 20

Hoskins, B. J., I. N. James, and G. H. White, 1983: The shape, propagation and mean-flow interaction of large-scale weather systems. *Journal of the Atmospheric Sciences*, **40 (7)**, 1595–1612, doi:10.1175/1520-0469(1983)040⟨1595:TSPAMF⟩2.0.CO;2. 14

Hoskins, B. J., and D. J. Karoly, 1981: The steady linear response of a spherical atmosphere to thermal and orographic forcing. *Journal of the Atmospheric Sciences*, **38 (6)**, 1179–1196, doi:10.1175/1520-0469(1981)038⟨1179:TSLROA⟩2.0.CO;2. 1, 61, 88

Hoskins, B. J., M. E. McIntyre, and A. W. Robertson, 1985: On the use and significance of isentropic potential vorticity maps. **111**, 877–946, doi:10.1002/qj.49711147002. 1, 4, 15, 29, 101, 112, 120

Hoskins, B. J., and P. J. Valdes, 1990: On the existence of storm-tracks. *Journal of the Atmospheric Sciences*, **47 (15)**, 1854–1864, doi:10.1175/1520-0469(1990)047⟨1854:OTEOST⟩2.0.CO;2. 14, 71

Hovmöller, E., 1949: The trough-and-ridge diagram. *Tellus*, **1 (2)**, 62–66, doi:10.1111/j.2153-3490.1949.tb01260.x. 2, 12

Huang, C. S. Y., and N. Nakamura, 2016: Local finite-amplitude wave activity as a diagnostic of anomalous weather events. **73**, 211–229, doi:10.1175/JAS-D-15-0194.1. 3, 4, 23, 30, 31, 34, 35, 36, 42, 52, 114

Huang, C. S. Y., and N. Nakamura, 2017: Local wave activity budgets of the wintertime Northern Hemisphere: Implications for the Pacific and Atlantic storm tracks. **44**, 5673–5682, doi:10.1002/2017GL073760. 4, 36, 38

James, I. N., 1994: *Introduction to Circulating Atmospheres*. Cambridge University Press, 230 pp. 14

Judt, F., 2018: Insights into atmospheric predictability through global convection-permitting model simulations. *Journal of the Atmospheric Sciences*, **75 (5)**, 1477–1497, doi:10.1175/JAS-D-17-0343.1. 118

Killworth, P. D., and M. E. McIntyre, 1985: Do Rossby-wave critical layers absorb, reflect or over-reflect? *J. Fluid Mech.*, **161**, 449–492, doi:10.1017/S0022112085003019. 3, 23

Lee, S., and I. M. Held, 1993a: Baroclinic wave packets in models and observations. *Journal of the Atmospheric Sciences*, **50 (10)**, 1413–1428, doi:10.1175/1520-0469(1993)050⟨1413:BWPIMA⟩2.0.CO;2. 2

Lee, S., and I. M. Held, 1993b: Baroclinic wave packets in models and observations. **50**, 1413–1428, doi:10.1175/1520-0469(1993)050⟨1413:BWPIMA⟩2.0.CO;2. 14

Lindzen, R. S., and B. Farrell, 1980: A simple approximate result for the maximum growth rate of baroclinic instabilities. *Journal of the Atmospheric Sciences*, **37 (7)**, 1648–1654, doi:10.1175/1520-0469(1980)037⟨1648:ASARFT⟩2.0.CO;2. 14

Liniger, M. A., and H. C. Davies, 2004: Seasonal differences in extratropical potential vorticity variability at tropopause levels. *Journal of Geophysical Research: Atmospheres*, **109 (D17)**, n/a–n/a, doi:10.1029/2004JD004639. 76

Liu, Y., X. San Liang, and R. H. Weisberg, 2007: Rectification of the bias in the wavelet power spectrum. *Journal of Atmospheric and Oceanic Technology*, **24 (12)**, 2093–2102, doi:10.1175/2007JTECHO511.1. 124

Lubis, S. W., C. S. Y. Huang, N. Nakamura, N.-E. Omrani, and M. Jucker, 2018: Role of finite-amplitude rossby waves and nonconservative processes in downward migration of extratropical flow anomalies. *Journal of the Atmospheric Sciences*, **75 (5)**, 1385–1401, doi:10.1175/JAS-D-17-0376.1. 4

Lynch, P., 1989: Partitioning the wind in a limited domain. *Mon. Wea. Rev.*, **117 (7)**, 1492–1500, doi:10.1175/1520-0493(1989)117⟨1492:PTWIAL⟩2.0.CO;2. 45

Martinez-Alvarado, O., E. Madonna, S. L. Gray, and H. Joos, 2016: A route to systematic error in forecasts of rossby waves. *Quart. J. Roy. Meteor. Soc.*, **142 (694)**, 196–210, doi:10.1002/qj.2645. 2, 120

Martius, O., C. Schwierz, and H. Davies, 2008: Far-upstream precursors of heavy precipitation events on the alpine south-side. *Quarterly Journal of the Royal Meteorological Society*, **134 (631)**, 417–428, doi:10.1002/qj.229. 2

Martius, O., C. Schwierz, and H. Davies, 2010: Tropopause-level waveguides. *Journal of the Atmospheric Sciences*, **67 (3)**, 866–879, doi:10.1175/2009JAS2995.1. 1

Martius, O., C. Schwierz, and H. C. Davies, 2007: Breaking waves at the tropopause in the wintertime northern hemisphere: Climatological analyses of the orientation and the theoretical lc1/2 classification. *Journal of the Atmospheric Sciences*, **64 (7)**, 2576–2592, doi:10.1175/JAS3977.1. 72

Masato, G., B. J. Hoskins, and T. J. Woollings, 2012: Wave-breaking characteristics of midlatitude blocking. *Quarterly Journal of the Royal Meteorological Society*, **138 (666)**, 1285–1296, doi:10.1002/qj.990. 72

McIntyre, M., 1980: An introduction to the generalized lagrangian-mean description of wave, mean-flow interaction. *pure and applied geophysics*, **118 (1)**, 152–176, doi: 10.1007/BF01586449. 23, 24

McIntyre, M. E., and T. G. Shepherd, 1987: An exact local conservation theorem for finite-amplitude disturbances to non-parallel shear flows, with remarks on hamiltonian structure and on arnol'd's stability theorems. **181**, 527–565, doi: 10.1017/S0022112087002209. 3, 16, 23

Methven, J., 2013: Wave activity for large-amplitude disturbances described by the primitive equations on the sphere. *Journal of the Atmospheric Sciences*, **70**, 1616–1630, doi:10.1175/JAS-D-12-0228.1. 23, 30, 38, 70

Methven, J., B. J. Hoskins, E. Heifetz, and C. H. Bishop, 2005: The counter-propagating Rossby-wave perspective on baroclinic instability. Part IV: Nonliner life cycles. *Quart. J. Roy. Meteor. Soc.*, **131**, 1425–1440. 101

Nakamura, N., and C. S. Y. Huang, 2017: Local wave activity and the onset of blocking along a potential vorticity front. **74**, 2341–2362, doi:10.1175/JAS-D-17-0029.1. 4

Nakamura, N., and A. Solomon, 2010: Finite-amplitude wave activity and mean flow adjustments in the atmospheric general circulation. part i: Quasigeostrophic theory and analysis. *Journal of the Atmospheric Sciences*, **67 (12)**, 3967–3983, doi:10.1175/2010JAS3503.1. 3, 4, 20, 25, 26, 27, 65

Nakamura, N., and A. Solomon, 2011: Finite-amplitude wave activity and mean flow adjustments in the atmospheric general circulation. part ii: Analysis in the isentropic coordinate. *Journal of the Atmospheric Sciences*, **68 (11)**, 2783–2799, doi:10.1175/2011JAS3685.1. 3, 4, 28, 29, 30, 36, 38, 40, 65, 69, 70, 71, 73

Nakamura, N., and D. Zhu, 2010: Finite-amplitude wave activity and diffusive flux of potential vorticity in eddy–mean flow interaction. *Journal of the Atmospheric Sciences*, **67 (9)**, 2701–2716, doi:10.1175/2010JAS3432.1. 3, 24, 25, 35, 90

Novak, L., M. H. P. Ambaum, and R. Tailleux, 2017: Marginal stability and predatorprey behaviour within storm tracks. *Quart. J. Roy. Meteor. Soc.*, **143 (704)**, 1421–1433, doi:10.1002/qj.3014. 98

Orlanski, I., 2003: Bifurcation in eddy life cycles: Implications for storm track variability. *J. Atmos. Sci.*, **60 (8)**, 993–1023, doi:10.1175/1520-0469(2003)60⟨993:BIELCI⟩2.0.CO;2. 88

Orlanski, I., and J. Katzfey, 1991: The life cycle of a cyclone wave in the Southern Hemisphere. Part I: Eddy energy budget. **48**, 1972–1998. 2, 18

Pedlosky, J., 1972: Finite-amplitude baroclinic wave packets. *Journal of the Atmospheric Sciences*, **29 (4)**, 680–686, doi:10.1175/1520-0469(1972)029⟨0680:FABWP⟩2.0.CO;2. 12, 14

Plant, R. S., and G. C. Craig, 2008: A stochastic parameterization for deep convection based on equilibrium statistics. *Journal of the Atmospheric Sciences*, **65 (1)**, 87–105, doi:10.1175/2007JAS2263.1. 76

Plumb, R. A., 1985: On the three-dimensional propagation of stationary waves. *Journal of the Atmospheric Sciences*, **42 (3)**, 217–229, doi:10.1175/1520-0469(1985)042⟨0217:OTTDPO⟩2.0.CO;2. 2, 3, 35, 61, 116

Plumb, R. A., 1986: Three-dimensional propagation of transient quasi-geostrophic eddies and its relationship with the eddy forcing of the timemean flow. *Journal of the Atmospheric Sciences*, **43 (16)**, 1657–1678, doi:10.1175/1520-0469(1986)043⟨1657:TDPOTQ⟩2.0.CO;2. 3, 35, 61, 116

Rhines, P. B., 2002: *Encyclopedia of Atmospheric Sciences*, chap. Rossby waves, 1923–1939. Elsevier. 8

Rodwell, M. J., and Coauthors, 2013: Characteristics of occasional poor medium-range weather forecasts for europe. *Bulletin of the American Meteorological Society*, **94 (9)**, 1393–1405, doi:10.1175/BAMS-D-12-00099.1. 2, 5, 62, 67, 104, 106, 113, 120

Rossby, C.-G., 1939: Eelation between variations in the intensity of the zonal circulation of the atmosphere and the displacements of the semi-permanent centers of action. *J. Mar. Re*, **2**, 38–55. 1

Rossby, C.-G., 1940: Planetary flow patterns in the atmosphere. *Quarterly Journal of the Royal Meteorological Society*, **66 (supplement)**, 68–87. 1

Saffin, L., J. Methven, and S. L. Gray, 2016: The non-conservation of potential vorticity by a dynamical core compared with the effects of parametrized physical processes. *Quart. J. Roy. Meteor. Soc.*, **142 (696)**, 1265–1275, doi:10.1002/qj.2729. 2, 5

Schubert, S., H. Wang, and M. Suarez, 2011: Warm season subseasonal variability and climate extremes in the northern hemisphere: The role of stationary rossby waves. *Journal of Climate*, **24 (18)**, 4773–4792, doi:10.1175/JCLI-D-10-05035.1. 2

Selz, T., 2019: Estimating the intrinsic limit of predictability using a stochastic convection scheme. *Journal of the Atmospheric Sciences*, **76 (3)**, 757–765, doi:10.1175/JAS-D-17-0373.1. 76, 82, 83, 84

Selz, T., and G. C. Craig, 2015: Upscale error growth in a high-resolution simulation of a summertime weather event over europe. *Monthly Weather Review*, **143 (3)**, 813–827, doi:10.1175/MWR-D-14-00140.1. 117, 118

Shaw, T., and Coauthors, 2016: Storm track processes and the opposing influences of climate change. *Nature Geoscience*, **9 (9)**, 656. 71, 74

Shutts, G. J., 1983: The propagation of eddies in diffluent jetstreams: Eddy vorticity forcing of blocking flow fields. *Quarterly Journal of the Royal Meteorological Society*, **109 (462)**, 737–761, doi:10.1002/qj.49710946204. 2

Simmons, A. J., and B. J. Hoskins, 1978: The life cycles of some nonlinear baroclinic waves. *Journal of the Atmospheric Sciences*, **35 (3)**, 414–432, doi:10.1175/1520-0469(1978)035⟨0414:TLCOSN⟩2.0.CO;2. 14, 71

Solomon, A., and N. Nakamura, 2012: An exact lagrangian-mean wave activity for finite-amplitude disturbances to barotropic flow on a sphere. *Journal of Fluid Mechanics*, **693**, 69–92, doi:10.1017/jfm.2011.460. 3, 24, 52, 90

Souders, M. B., B. A. Colle, and E. K. M. Chang, 2014: The climatology and characteristics of rossby wave packets using a feature-based tracking technique. *Monthly Weather Review*, **142 (10)**, 3528–3548, doi:10.1175/MWR-D-13-00371.1. 72, 74, 117

Swanson, K., and R. T. Pierrehumbert, 1994: Nonlinear wave packet evolution on a baroclinicaily unstable jet. *Journal of the Atmospheric Sciences*, **51 (3)**, 384–396, doi:10.1175/1520-0469(1994)051⟨0384:DCCISF⟩2.0.CO;2. 16

Takaya, K., and Y. Nakamura, 2001: A formulation of a phase-independent wave-activity flux for stationary and migratory quasigeostrophic eddies on a zonally varying basic flow. **58**, 608–627, doi:10.1175/1520-0469(2001)058⟨0608:AFOAPI⟩2.0.CO;2. 2, 3, 35, 59, 115, 116

Teubler, F., and M. Riemer, 2016: Dynamics of rossby wave packets in a quantitative potential vorticity–potential temperature framework. *Journal of the Atmospheric Sciences*, **73 (3)**, 1063–1081, doi:10.1175/JAS-D-15-0162.1. 5, 45, 112, 119

Thorncroft, C. D., B. J. Hoskins, and M. E. McIntyre, 1993: Two paradigms of baroclinic-wave life-cycle behaviour. **119**, 17–55, doi:10.1002/qj.49711950903. 65

Torrence, C., and G. P. Compo, 1998: A practical guide to wavelet analysis. *Bulletin of the American Meteorological society*, **79 (1)**, 61–78, doi:10.1175/1520-0477(1998)079⟨0061:APGTWA⟩2.0.CO;2. 124

Tung, K. K., 1986: Nongeostrophic theory of zonally averaged circulation. part i: Formulation. **43 (22)**, 2600–2618, doi:10.1175/1520-0469(1986)043⟨2600:NTOZAC⟩2.0.CO;2. 30, 38

Vallis, G. K., 2006: *Atmospheric and Oceanic Fluid Dynamics: Fundamentals and Large-Scale Circulation*. Cambridge University Press, 745 pp, Cambridge, U.K., 745 pp. 9, 17, 20, 21, 22

Wilcox, L., B. Hoskins, and K. Shine, 2012: A global blended tropopause based on era data. part i: Climatology. *Quarterly Journal of the Royal Meteorological Society*, **138 (664)**, 561–575. 72

Williams, P. D., 2011: The raw filter: An improvement to the robert–asselin filter in semi-implicit integrations. *Monthly Weather Review*, **139 (6)**, 1996–2007, doi: 10.1175/2010MWR3601.1. 48, 88

Wirth, V., and J. Eichhorn, 2014: Long-lived rossby wave trains as precursors to strong winter cyclones over europe. *Quarterly Journal of the Royal Meteorological Society*, **140 (680)**, 729–737, doi:10.1002/qj.2191. 2

Wirth, V., M. Riemer, E. K. M. Chang, and O. Martius, 2018: Rossby wave packets on the midlatitude waveguidea review. *Monthly Weather Review*, **146 (7)**, 1965–2001, doi:10.1175/MWR-D-16-0483.1. 11, 16

Wolf, G., and V. Wirth, 2017: Diagnosing the horizontal propagation of Rossby wave packets along the midlatitude waveguide. **145**, 3247–3264, doi:10.1175/MWR-D-16-0355.1. 2, 59, 115

Yang, G.-Y., and B. J. Hoskins, 1996: Propagation of rossby waves of nonzero frequency. *Journal of the Atmospheric Sciences*, **53 (16)**, 2365–2378, doi:10.1175/1520-0469(1996)053⟨2365:PORWON⟩2.0.CO;2. 59

Yi, H., and H. Shu, 2012: The improvement of the morlet wavelet for multi-period analysis of climate data. *Comptes Rendus Geoscience*, **344 (10)**, 483–497, doi:10.1016/j.crte.2012.09.007. 123, 124

Zängl, G., D. Reinert, P. Rípodas, and M. Baldauf, 2015: The icon (icosahedral nonhydrostatic) modelling framework of dwd and mpim: Description of the nonhydrostatic dynamical core. *Quarterly Journal of the Royal Meteorological Society*, **141 (687)**, 563–579, doi:10.1002/qj.2378. 76

Zhang, F., N. Bei, R. Rotunno, C. Snyder, and C. C. Epifanio, 2007: Mesoscale predictability of moist baroclinic waves: Convection-permitting experiments and multistage error growth dynamics. *Journal of the Atmospheric Sciences*, **64 (10)**, 3579–3594, doi:10.1175/JAS4028.1. 82, 118

Zimin, A. V., I. Szunyogh, B. R. Hunt, and E. Ott, 2006: Extracting envelopes of

nonzonally propagating rossby wave packets. *Monthly Weather Review*, **134 (4)**, 1329–1333, doi:10.1175/MWR3122.1. 2, 72, 74

Zimin, A. V., I. Szunyogh, D. Patil, B. R. Hunt, and E. Ott, 2003: Extracting envelopes of rossby wave packets. *Monthly Weather Review*, **131 (5)**, 1011–1017, doi:10.1175/1520-0493(2003)131⟨1011:EEORWP⟩2.0.CO;2. 2, 5, 12, 13, 48, 67, 78, 115, 121